1-1-2010

Computational Fluid Dynamic Optimization and Design for the Airborne Laser System

Matthew James Opgenorth
University of Denver

COMPUTATIONAL FLUID DYNAMIC OPTIMIZATION AND DESIGN FOR THE AIRBORNE LASER SYSTEM

_____

A Dissertation

Presented to

the Faculty of Engineering and Computer Science

University of Denver

_____

In Partial Fulfillment

Of the Requirements for the Degree

Doctor of Philosophy

_____

by

Matthew J. Opgenorth

November 2010

Advisor: Dr. Corinne Lengsfeld

Author: Matthew J. Opgenorth
Title: COMPUTATIONAL FLUID DYNAMIC OPTIMIZATION AND DESIGN FOR THE AIRBORNE LASER SYSTEM
Advisor: Dr. Corinne Lengsfeld
Degree Date: November 2010

ABSTRACT

The Airborne Laser (ABL) was designed to destroy any ballistic missile shortly after launch that could be a threat to the United States and its allies. The ABL uses several lasers to accomplish the destruction of the ballistic missile, most notably the high powered Chemical Oxygen Iodine Laser (COIL). The COIL is a complex device that could be improved upon in several areas that will result in overall weight reduction, refinement of beam quality, and increased magazine capacity.

This dissertation presents novel design and optimization techniques coupled with fluid dynamics to improve the performance of the COIL system. The focus was on two components of the COIL system: the iodine mixing nozzle and the pressure recovery system. Improvements to the iodine mixing nozzle were made in terms of mixing efficiency, gain uniformity, and flow uniformity. These improvements result in a power increase per module, which in turn reduces the overall number of modules required to shoot down a missile. The use of fewer modules significantly reduces the weight of the entire system.

Additionally, investigations into the pressure recovery system led to further reduction in weight. New designs increased the mixing of the flows, which improved the pressure recovery and entrainment ratios. Focusing on the ABL application, the required pressure recovery needed for operation could be achieved with lower flow rates, and thus, less fluid is needed onboard.

ACKNOWLEDGEMENTS

I would like to thank Dr. Corinne Lengsfeld and the lab group for continuous support and advisement, Dr. Peter Laz for guidance with the optimization analysis, Dr. William McDermott for his technical expertise in COIL systems, and lastly Dr. Thomas Henshaw and Neumann Systems Group for collaboration on this project. This project was funded by the Missile Defense Agency; "Close Coupling of Excited Oxygen with Iodine Injection in COIL Lasers," Contract No. HQ0006-07-C-7652 and HQ0006-06-C-7508 and "Improved Pressure Recovery System for the ABL," Contract No. HQ0006-09-C-7174.

Table of Contents

List of Tables

List of Figures

CHAPTER 1

INTRODUCTION

History of the Airborne Laser

Any ballistic missile that has a range between 300 and 3500 kilometers is classified as a theater ballistic missile (TBM). These missiles can deliver high explosives, chemical, biological, or nuclear warheads [1]. For the first time in 1991, during the Persian Gulf War, the Iraqi military fired TBMs at US Forces. Even though the TBM were widely ineffective the threat revealed deficiencies in the US Defenses [1-3]. One short-coming is that the US defenses do not have a deployed technology to defend against a TBM in its boost phase. The Airborne Laser (ABL) would solve this inadequacy.

The current Ballistic Missile Defense System for the US takes an integrated approach in order to intercept and destroy missiles prior to reaching their targets. The architecture incorporates [4]:

- Networked sensors and ground and sea-based radars for target detection and tracking
- Ground and sea-based interceptor missiles for destroying a ballistic missile using either the force of direct collision, called “hit-to-kill” technology, or an explosive blast fragmentation warhead
- A command and control, battle management, and communications network providing the war fighter with the needed links among the sensors and interceptor missiles

The flight trajectory of a ballistic missile is divided into four categories: boost, ascent, midcourse, and terminal. Intercepting the missile in the terminal phase is the most difficult and therefore the least desirable phase to intercept. This phase starts when the missile reenters the atmosphere which gives little time for destruction and interception occurs close to the intended target Current terminal phase interceptor systems include Aegis BMD near-term Sea-Based Terminal Defense and the U.S. Army's PATRIOT Advanced capability 3 (PAC-3) [4].

During the first Gulf War, it was shown that not only was the PATRIOT's performance unsatisfactory, but the point defense (interception) concept was as well [3]. Anytime a TBM was fired during the first Gulf War, two Patriots were launched. That means that there are three missiles in the air every time there is a threat launched. When this happens the TBM could be destroyed, but damage could happen from falling pieces. Second, if a PATRIOT missile intercepts the TBM successfully, it may not destroy the missile but just sever the missile leaving the warhead intact and armed. Lastly, if one or all of the PATRIOT missiles fail to intercept, there is a potential for a system failure resulting in falling to the ground while still ignited [3].

The midcourse phase of a ballistic missile is when the missile is coasting in space and can have duration upwards of 20 minutes. This duration of time allows for several opportunities to employ the "hit-to-kill" technology. In addition to the Aegis sea-based missile defense, ground-based midcourse defenses are deployed in Alaska, California, and future sites in Europe for defense against countries like North Korea and Iran [4]. These systems are highly advanced and fully integrated with missiles, launchers, radar, and command and control. They can receive cueing information from numerous sources including both theater and on-orbit sensors [3]. While the time for destruction and interception is greater; there is still a limited range based on the location of the interceptor defenses.

There are numerous challenges and benefits to the interception of ballistic missiles during the ascent and boost phases. The ascent phase is categorized as the phase after powered flight, but prior to apogee. Preceding the ascent phase, the boost phase can last 1 to 5 minutes. Obvious challenges for destruction of the TBM during these phases include a short window time for interception and the need for close proximity to the missile launch site. However, the ballistic missile is easiest to detect during the boost phase due to the large plume of hot exhaust. Also, since the missile is far from its intended target countermeasures have not been deployed resulting is an easier shoot-down [4]. To date there are no systems deployed to counter TBMs during there boost and ascent phases.

Figure 1.1: Depiction of the different phases of a ballistic missile [4].

The Airborne Laser (ABL) is designed to destroy a TBM during its boost phase or if needed during the ascent phase. The system comprises of a modified Boeing 747-400F which houses two solid-state lasers and one megawatt class Chemical Oxygen Iodine Laser (COIL). The first solid-state laser, the Track Illuminator, tracks the missile once it is detected by the ABL's infrared sensors. The second solid-state laser measures the atmospheric disturbances which the adaptive optics system will compensate. Lastly, the COIL sends a beam of high energy to the intended missile which will rupture the skin and cause structural failure with ranges in the "100s of kilometers" (the actual distance is classified) [4].

Chemical Oxygen Iodine Laser

COIL has the shortest wavelength, 1.315 μm, of any high power chemical laser. The shortwave length, along with megawatt power, allows for a more compact laser producing a lethal beam over long distances [5]. This technology was first demonstrated by the Air Force Weapons Lab in 1977 [6]. The COIL is driven by reacting gaseous chlorine and aqueous basic hydrogen peroxide (BHP) which produces singlet delta oxygen, O2($^1\Delta$), with efficiencies near 100% [7]. This reaction occurs in the Singlet Oxygen Generator (SOG). Molecular iodine is injected into the singlet oxygen flow through a bank of nozzles and mixed sub-sonically. The stored energy in the singlet delta oxygen dissociates the molecular iodine into iodine atoms. The chemical reaction is given as:

$$O_2(^1\Delta) + I(^2P_{3/2}) \leftrightarrow O_2(X^3\Sigma) + I(^2P_{1/2}) \quad (1)$$

After mixing, the flow is accelerated to supersonic velocities via converging-diverging nozzle and creates the laser gain region. The optical resonator extracts the light transversely to the gas flow. The gases then flow through a supersonic diffuser in order to reduce the flow velocity to subsonic speeds and start the pressure recovery process. Finally, the flow enters a supersonic ejector where high temperature and high pressure steam mixes with the gases to increase the overall pressure to atmospheric conditions. A simple schematic in Figure 1.2 shows the basic configuration of a chemical laser with a close up of the nozzle bank and lasing cavity in Figure 1.3.

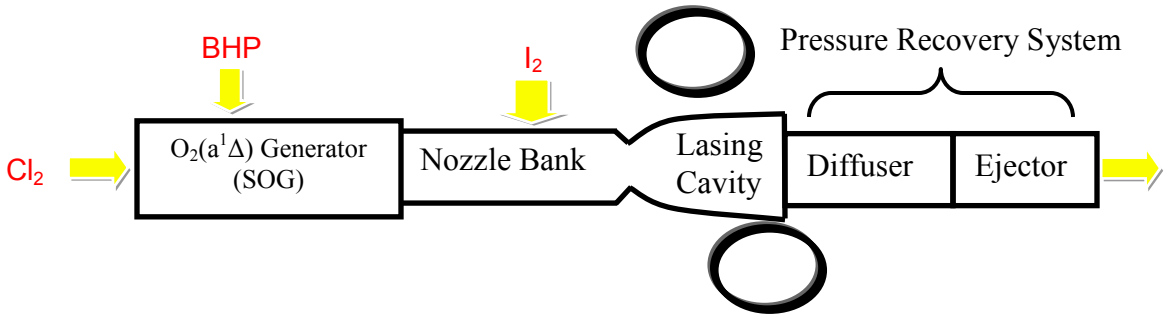

Figure 1.2: Schematic of the COIL.

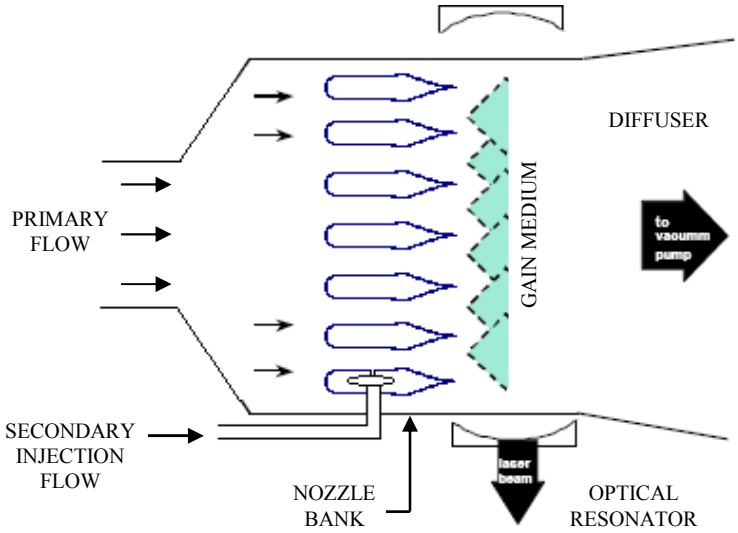

Figure 1.3: Close up of the nozzle bank and lasing cavity.

Currently, there are six COIL modules each the size of a pickup truck and weighs upwards of 6500 pounds not including the support equipment (e.g. Pressure Recovery System (PRS) and turret) and plumbing [5]. An off-the-shelf Boeing 747-400F has a maximum payload of approximately 248,300 pounds [8]. In addition to the overall weight, engineers have to be concerned with the weight that the flooring can support and the distribution. This dissertation will expand on the weight discussion for nozzle bank and supersonic ejector of the COIL, highlighting the opportunities for improvement in performance and reduction in weight.

COIL Mixing Nozzle

The historical configuration of the supersonic COIL mixing nozzle is a converging-diverging nozzle (see Figure 1.4) with two rows of offset iodine injector holes. These holes inject the molecular iodine transversely to the primary singlet delta oxygen gas flow.

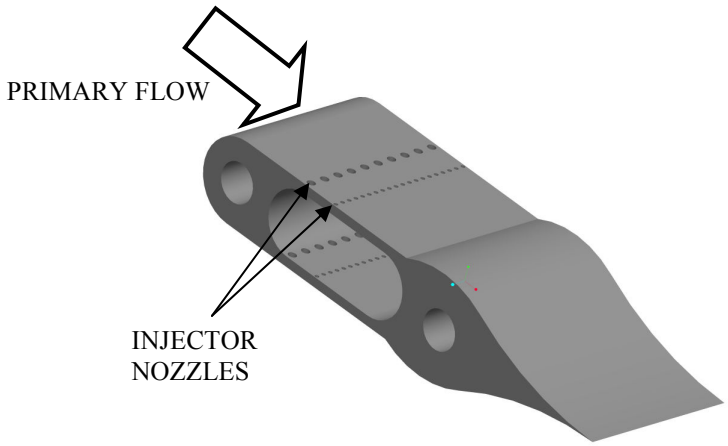

Figure 1.4: Traditional supersonic iodine mixing nozzle. The iodine is injected into the primary flow through the injector nozzles.

There have been several key researchers in the area of COIL nozzle computational fluid dynamic (CFD) analysis. Madden et al. [9-14] has reported numerous simulations analyzing the different mechanisms contributing to the mixing and utilizing planar laser induced fluorescence for experimental comparison. Madden [14] indicates that the mixing of the iodine into the primary flow is created by the interfacial area created by the cross flow jets and molecular diffusion. He also states that since molecular diffusion and chemical reactions are strongly linked to spatial gradients of the reactant concentration, the flow structure created from the interaction of the jets with the primary flow will have a great impact on the gain of the laser. Lastly, Madden proposes a supersonic injection of the iodine gas in order to improve mixing and pressure recovery. Unfortunately, he never

reports the results of his investigation other than validation of his CFD models. Additionally, Miller et al. [15] and Endo et al. [16] have also performed CFD simulations with experimental validation and report detailed flow characteristics on existing nozzle designs. Miller et al. details the velocity distributions and pressure measurements at different locations within the nozzle. The pressure calculated was compared to experimental measurements and showed good agreement. With the exception of Endo et al.[16], researchers have only examined existing nozzles and have not used CFD to attempt to redesign the COIL nozzle to improve performance. Endo et al. [16] investigated a radically designed x-wing nozzle to overcome the inefficient mixing of a supersonic injected iodine flow. It was found that the supersonic injection of iodine is favorable to the subsonic injection due to reduction in water quenching losses. However, supersonic injection has poor mixing since the compressibility of the fluid stabilizes the flow. The x-wing nozzle was designed to both expand the flow supersonically and create vortices to enhance mixing. Their results showed an increase in power and gain distribution compared to a conventional nozzle. However, Endo et al. failed to report the effect that the vortex generators may have on the beam quality and density distributions. In this author's opinion, the location and geometry of the vortex generators could lead to a complex shock structure that could adversely affect the overall performance of the COIL. Additionally, Endo et al. was focusing on industrial COILs which do not need good beam quality since the material can be placed close to the laser. The ABL is attempting to destroy a missile at 100s of kilometers from the plane and beam quality becomes very important. Additional research needs to be carried out on different nozzle designs that will lead to improved performance and enhanced mixing of iodine for ABL applications.

This dissertation builds from previous research completed by the University of Denver's Fluids Lab [17]. Previous work has demonstrated that through CFD optimization the mixing can be improved by 13% for a subsonic nozzle with cross flow injection. Chapter Two will present mixing results using the same methodology, but for a supersonic nozzle

of greater complexity. Chapter Three takes a step further to include chemical kinetics where the results become directly relevant to weight savings.

Pressure Recovery System

The Pressure Recovery System (PRS) aids in driving the flow of the whole system while exhausting to the atmosphere. Two components comprise the PRS: the diffuser and the ejector. The purpose of the diffuser is to reduce the Mach number of the primary flow after lasing and bring it to subsonic velocities [18]. The ABL design of the supersonic diffuser is very complex and specific to the COIL. The design is based on the chemicals and diluents, the amount of heat generation within the diffuser (which is unique to the COIL compared to other chemical lasers), size and construction, gas dynamic parameters (depends on operating conditions; i.e. ground-based or airborne), and the particularities of the singlet-delta oxygen generator (SOG), just to name a few [19].

In order for the Airborne Laser to operate, the low pressure in the lasing cavity must be recovered to atmospheric conditions at approximately 40,000 feet above sea level. Due to recovery requirements and lack of electric energy available on a plane, the only option is supersonic ejectors which are currently used. These ejectors utilize a high temperature, high pressure steam flowing through a supersonic nozzle to transfer momentum to the laser gases exiting the lasing cavity. This momentum transfer results in the increase of pressure of the mixed flow as it exits the ejector. A diagram of a typical ejector is shown in Figure 1.5.

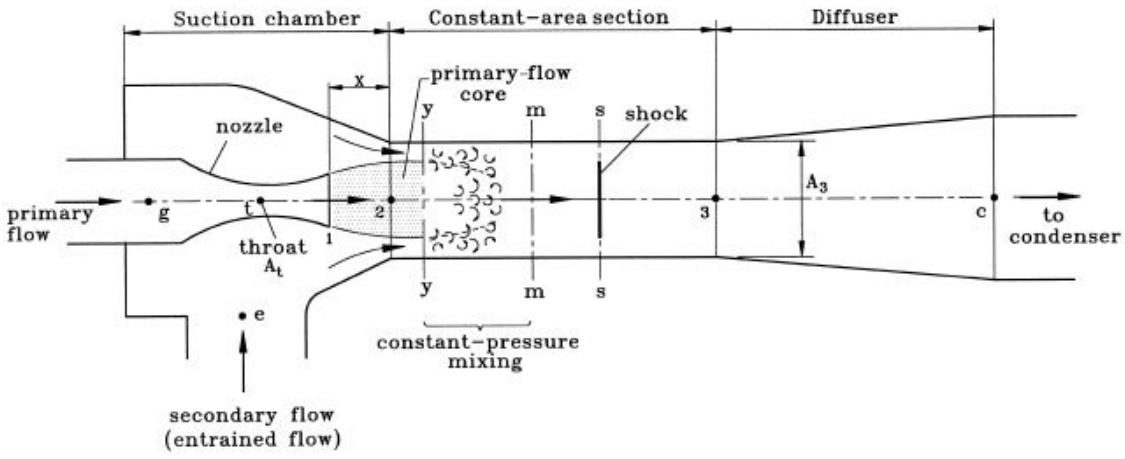

Figure 1.5: Schematic of a typical supersonic ejector [20].

A significant amount of information is known about supersonic ejectors from refrigeration applications. The first substantial contribution came from Keenan et al [21] who developed a one dimensional analytical approach to assist in design using first principles (i.e., continuity and energy equations). Building off of Keenan et al., Munday et al. [22] developed a theory to account for the effective choke area for the secondary flow. Later, more researchers continued to improve on the models by accounting for irreversibilities within the system [23-25]. From these analytical models came numerous experimental efforts that explored wide ranges in operating conditions [22, 24, 26-28], as well as comparisons to CFD simulations [29-32].

However, refrigerant systems are small in size and flow rates relative to the ABL PRS, thus the motivation to maximize the pressure recovery for a given entrainment ratio needs to be further explored. For example, approximately 17 tons of motive fluid is carried onboard the ABL in order to recover the pressure needed to operate the COIL. Even a small percentage of increased efficiency would lead to a large weight savings. Research done in refrigerant systems has sought improved efficiencies. For instance, Eames [33] proposed a profiled geometry for the mixing channel in order to remove normal shocks. The profile does not directly reduce the motive fluid requirements, but dramatically

increases the pressure recovery. A redesign of parameters may allow for the reduction of fluid requirements for a given pressure recovery. Eames provides a one-dimensional analysis that generates the profiled channel for a given set of boundary conditions. Varga et al. [34] also reports that there is an optimum distance from the motive nozzle exit position to the entrance of the mixing channel to provide the largest entrainment of the two fluids. The shape of the motive nozzle was explored by Srikrishnan et al. [35]. They observed enhanced mixing of a six-lobed nozzle compared to a round nozzle at Mach 1.67 into a sonic secondary flow with equal boundary conditions. The degree of mixing was quantified by the distribution of the momentum at a given location downstream. Similarly, Chang et al. also looked at a six-lobed nozzle in their experiments and concluded that the lobed nozzle outperformed a round nozzle, but the flow field was not well understood [36].

Chapter Five will more thoroughly explore ways to improve the performance of supersonic ejectors in efforts to reduce the 17 tons of motive fluid currently needed to operate. In an effort to reduce the motive flow requirements for the ABL both of the mixing channel and motive nozzle geometries will be investigated.

CHAPTER 2

SUPERSONIC IODINE MIXING NOZZLE: COLD FLOW OPTIMIZATION

Background

Conventional high-powered, directed energy laser systems utilize a complicated series of chemical reactions to produce the desired laser gain [3]. For example, in an oxygen-iodine laser the singlet state of oxygen is transported from the generator to a bank of supersonic nozzles where molecular iodine is injected transversely to the primary oxygen flow. The system relies on the rapid dissociation of molecular iodine into atomic iodine. In the gain region, atomic iodine will undergo many energy transfer, excitation, and stimulated emission cycles in order to extract most of the energy from the singlet oxygen during the lasing process. It can be speculated that better performance (i.e., gain and beam quality) would be achieved with a uniform distribution of iodine prior to exit from the mixing nozzle setting the stage for uniform lasing.

The objective of this research was to develop and demonstrate the use of computational fluid dynamics (CFD) in conjunction with optimization techniques in order to design a new mixing nozzle for a COIL laser system. An automated design tool for a supersonic nozzle with cross flow injection was developed and utilized to increase mixing performance. This effort required development of an accurate fluid dynamic (cold flow only) model of the cross flow injection into a primary flow, as well as, validation of the dynamic meshing strategy and algorithms chosen. Validation of the mixing behavior used Planar Laser Induced Fluorescence (PLIF) measurements from both base and improved

geometries. The goal was to obtain an improved design for a conventional chemical laser mixing nozzle through the exploration of multiple designs in a rapid fashion.

The University of Denver's Fluids Lab previously created and implemented an efficient computational design tool to combine optimization and probabilistic modeling to provide insight into how to improve HICl laser mixing nozzle performance [17]. The effort included simulation validation with experimental velocity and temperature profiles from a jet injected into subsonic cross flow. Most importantly, this effort demonstrated that the CFD algorithms were accurately modeling sub and supersonic conditions when compared to experimental data. With the automated process, the mixing results were shown to be consistent with known geometry improvements. Numerical results showed that elliptical orifices with the major diameter parallel to the flow direction increased the mixing within the system by roughly 13%. Haven et al. [37] similarly found through experimentation that the injection port geometry had a powerful influence on penetration in the near field [15]. The computational optimization approach discovered the optimum aspect ratio of the larger orifice to be approximately 6. Additionally, the small injection orifice should be placed upstream of the larger orifice in a staggered alignment pattern. It is crucial to note this configuration is opposite to the configuration employed in most chemical laser mixing nozzles (the large orifice is upstream of the small orifice).

With a functioning computational fluid dynamic automated design tool, this work directs its efforts to the more complex COIL mixing nozzle and associated conditions. The computational model was modified to account for the supersonic flow and the boundary conditions. Additionally, the computational model was compared against the 10kW class supersonic COIL (Research Assessment and Device Improvement Chemical Laser - RADICL) [15] for preliminary validation of the CFD algorithms used for supersonic flow (data not shown). In addition to the computational validation, experimental data utilizing Planar Laser Induced Fluorescence (PLIF) was compared to the models. The PLIF experiments were carried out with an industrial collaborator. It is of interest to whether

the computational approach accurately models the fluid domain from sub to supersonic regimes and if the optimization reflects improvements in an experimental system.

Numerical Methodology

The beginning stages of this effort focused on the development of pairing an automated optimization routine with a sophisticated CFD software. The optimization routine will perturb several identified variables and calculate the resulting performance parameter to be optimized. The capabilities of this routine can include parameters of both physical geometry and flow characteristics. A simple flow chart is provided in Figure 2.1 outlining the different steps of the design tool.

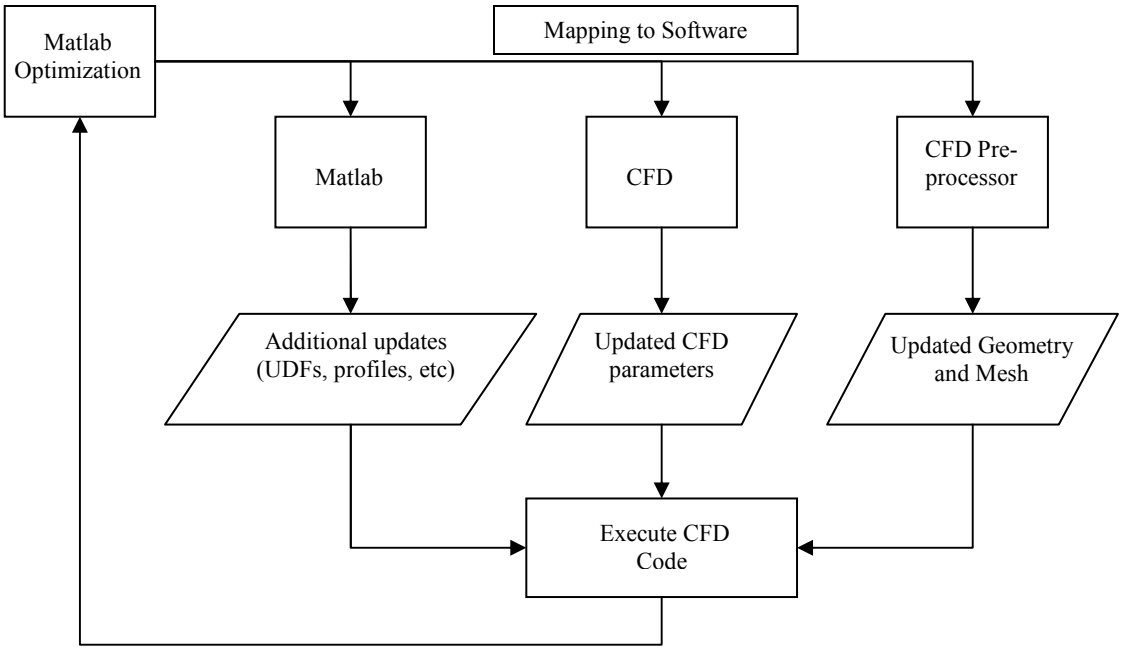

Figure 2.1: Diagram of the optimization and CFD interface. Each program is linked by custom scripts.

Numerical Model

The CFD software used for the simulations is Fluent™ Version 6.3.26 [38]. It is a state-of-the-art computational software package for modeling fluid flow and heat transfer in complex 3D geometries. Easy mesh generation and ability to refine or coarsen the mesh autonomously based on the flow solution are just some of the features that make this CFD package extremely versatile and ideal for automation. Gambit® was the pre-processor used for the solid modeling and mesh generation.

The 3-D Navier-Stokes numerical simulation of the COIL nozzle utilized a density based solver, due to the subsonic, transonic, and supersonic flow conditions, along with the k-epsilon turbulence model. The density based solver calculates the density from continuity (Equation 2), while the velocity field is given by the conservation of momentum (Equation 3). Additionally, energy and species must be conserved which are satisfied by Equations 4 and 5, respectively.

Continuity:
$$\frac{\partial \rho}{\partial t} + \nabla(\rho \vec{v}) = S_m \tag{2}$$

Momentum:
$$\frac{\partial}{\partial t}(\rho \vec{v}) + \nabla \cdot (p \vec{v} \vec{v}) = -\nabla p + \nabla \cdot (\overline{\overline{\tau}}) + \rho \vec{g} + \vec{F} \tag{3}$$

Energy:
$$\frac{\partial}{\partial t}(\rho E) + \nabla \cdot (\vec{v}(\rho E + p)) = \nabla \cdot (k_{eff} \nabla T - \sum h_j \vec{J}_j + (\overline{\overline{\tau}}_{eff} \cdot \vec{v})) + S_h \tag{4}$$

Species:
$$\frac{\partial}{\partial t}(\rho Y_i) + \nabla \cdot (\rho \vec{v} Y_i) = -\nabla \cdot \vec{J}_i + R_i + S_i \tag{5}$$

where ρ is the density, $\vec{v}$ is the velocity vector, S_m is the mass source term for the continuity equation and ∇ is the derivative in multi-dimensional space defined as

$\frac{\partial}{\partial x}i + \frac{\partial}{\partial y}j + \frac{\partial}{\partial z}k$. Additional terms in the momentum equation are: p is the pressure, $\bar{\bar{\tau}}$ is the stress tensor, g is gravity, and $\vec{F}$ is the force vector. Within the energy equation, E is the total fluid energy, k_{eff} is the effective thermal conductivity of the medium, T is the temperature, h is the enthalpy, $\vec{J}$ is the diffusion flux, and S_h is the enthalpy source term, which includes heat of chemical reactions and any other volumetric heat source terms. The first three terms on the right hand side of the energy equation (Equation 4) are the energy transfer terms due to conduction, species diffusion, and viscous dissipation, respectively. When solving for the conservation of chemical species (Equation 5), the algorithms will solve a convection-diffusion equation [38] for ith species where Y_i is the local mass fraction, R_i is the net rate of production of species by chemical reaction, and S_i is the rate of creation due to the dispersed phase plus any user-defined sources.

All of the conservation equations are solved by using a control volume based technique to convert a scalar transport equation to an algebraic equation that can be numerically solved. This procedure can be demonstrated by the discretization of the momentum equation in the x direction:

$$a_p u = \sum a_{nb} u_{nb} + \sum p_f A \cdot \hat{i} + S \tag{6}$$

Discretization allows differential equations over the entire flow domain to be converted to algebraic equations when the domain is parceled into small volume elements described by a single individual node located in the center of the volume. However, several rules apply to each control volume to ensure a physically correct solution is obtained. First, the size must be sufficiently small in order to accurately represent the fluid flow field. Second, the growth rate from one volume to an adjacent neighbor can not exceed 20%. Volume elements should maintain a low aspect ratio and regular shape, reducing skewness. An equilateral element is optimal and increases the accuracy and stability of a solution. Both first and second order discretizations were used depending on the non-

linearity of the conservation equations. A Roe flux-difference splitting (Roe-FDS) was used which splits the fluxes consistent with their eigenvalues. This flux algorithm scheme allows for both upstream cell boundary calculations for supersonic flow, as well as, upstream and downstream calculations for the subsonic flow.

The boundary conditions of pressure were used for the flow inlets and outlets. The nozzle walls were modeled as smooth and without slip. Initialization for the fluid domain was determined by isentropic relationships or from previously solved simulations. In order to get from the initial conditions to a final converged solution, the governing equations were decoupled through the lowering of the under-relaxation factors (URF) and then slowly increased. For the cold flow simulations, an initial grid of approximately 200,000 cells were modified using different adaption techniques to reach a scaled convergence of at least 1E-3, while the species and energy reached a convergence of 1E-5 and 1E-6, respectively. The adaption techniques used simply refined or coarsened the grid based on the gradients of normalized pressures and Mach numbers within the flow field. The k-epsilon turbulence model is robust and suitable for initial iterations, initial alternative design screenings, and parametric studies. This will be ideal for the automated analysis where many different shapes will be analyzed.

Optimization

Numerical optimization techniques are designed to minimize an objective function subject to constraints, with many different algorithms developed over the past several decades [39]. In general, the algorithms require a starting point, x_0, and then iterate until there is no more progression, or the approximate solution falls within a user-defined tolerance. Typically, algorithms follow one of two types of strategies, line search or trust region. This study implemented a trust region [40] strategy, because it is speculated that the geometric changes would result in the fluid domain acting non-linearly. A common problem in line searches is that the fixed step size can cause them to miss a local

minimum. Where as the step size in the trust region search is not fixed and has a better opportunity to find a minimum that is close to the current point.

The success and efficiency of an optimization is contingent on selection of an appropriate algorithm and an accurate characterization of the problem. The optimization algorithm had to be suitable for a continuous objective function with variables that are constrained by simple bounds and can solve for linear, non-linear, and convex variables.

The trust-region algorithm utilized an active-set algorithm for the optimization analysis. An active-set algorithm will employ linear techniques to estimate the active-set at each iteration and then solve an equality constrained quadratic program to generate a step [41]. This method was used because it tends to yield more exact solutions and is less sensitive to the initial starting point than interior point methods. Another benefit of the active-set algorithm is that it uses a gradient projection method when only bounds are applied to the constraints [42]. The gradient projection method attempts to speed up the solution process within the active-set, but is only utilized when the variables are bounded. It consists of two different stages. First, the search direction will be along the path of steepest decent from the current point. The second stage investigates the face of the feasible region using the active-set constraints [41]. The second stage can significantly reduce the optimization time.

Interfacing Model

To facilitate communication between all of the software packages, custom interfacing was developed to build CFD models with perturbed parameters and calculate performance parameters from the analysis outputs. Interfacing was performed with components written in Matlab®, DOS and C. In addition, checks were performed to ensure mesh quality to prevent analyses that would fail or highly skewed elements, which

may lead to convergence issues. This is noteworthy because the automated process can potentially take days and even weeks to run and computational efficiency will be a driving factor, especially as the complexities of the flow increases. A Matlab script is also utilized to calculate the performance parameter and print the results for analysis by the optimization routine.

Problem Description

Utilizing optimization with CFD allows for rapid investigations into a complex system with many parameters. For this investigation, only geometric parameters will be perturbed, leaving the flow parameters constant throughout the process. This will allow the experimental validation setup to remain constant while different nozzles will be interchanged. In this design optimization process the following variables were manipulated:

1. Converging Radius
2. Diverging radius
3. Expansion Radius
4. Aspect Ratio of the I_2 injection
5. Distance to the I_2 injection from the leading edge
6. Throat height

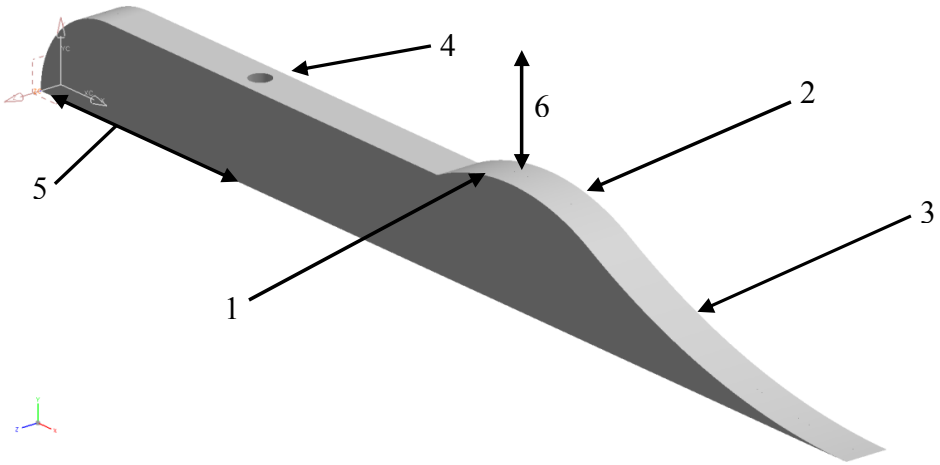

Figure 2.2: Schematic of the parameters perturbed during the optimization process. 1) Converging radius, 2) Diverging radius, 3) Expansion Radius, 4) Aspect ratio of iodine injector, 5) Location of the iodine injector.

The performance parameter used is Mixedness, which is defined by:

$$Mixedness = 1 - \frac{\sum | M_f - M_{f\_Homogeneous} |}{n \cdot M_{f\_Homogeneous}} \tag{7}$$

where M_f is the mole fraction of an interested species of gas, $M_{f\_Homogeneous}$ is the homogeneous mole fraction across a downstream plane for the gas of interest within the fluid domain (this signifies perfect mixing), and n is the number of computational nodes over which Mixedness will be calculated.

The degree of mixing is measured by the ratio of the integral value for species mole fraction across an exit plane divided by the homogeneous result. The optimization routine will perturb these variables, based on its algorithm, until all of the convergence criteria are satisfied. Convergence was set such that each variable and the performance parameter must no longer be changing within a scaled tolerance of 1E-3. Increased mixing of

species in chemical systems should result in greater chemical efficiencies and better performance. This can be shown by the heuristic equation [43]:

$$P(kW) = 91\dot{m}_{Cl2}\eta_{chem} \tag{8}$$

where the $\dot{m}_{Cl2}$ is the mass flow rate of chlorine and chemical efficiency (η_{chem}) can be given by:

$$\eta_{chem} = U_{til}(Y_{NIP} - Y_{diss} - Y_{thres})\eta_{mix}\eta_{extr} \tag{9}$$

where U_{til} is the utilization of chlorine, Y_{NIP} is the yield in the nozzle inlet plane, Y_{diss} is the loss of singlet delta oxygen due to iodine dissociation, Y_{thres} is the threshold yield representing the minimum singlet delta oxygen fraction necessary for positive gain, η_{mix} is the mixing efficiency, and η_{extr} is the optical extraction efficiency. For the cold flow simulations, the utilization and yields are not calculated due to not having any reactions therefore the power becomes a function of mixing efficiency.

$$\eta_{mix} = \int \frac{I_{mol\_frac} * dA}{I_{\max\_mol\_frac} * A} \tag{10}$$

and

$$\eta_{chem} = f\left(Y_{diss}, \eta_{mix}\right) \tag{11}$$

Additionally, I_2 dissociates into I and I^*, therefore the distribution of I_2 is proportional to I. The mixing parameter proposed in Equation 11 is the same as the mixing efficiency

except on a nodal basis instead of area. Nodes are simply the grid points used to describe the fluid domain and locations where the calculations occur.

Experimental Methods

Previous work validated the cross-flow injection velocity and penetration [44] but for this multi-species computational simulation it is necessary to validate iodine concentration profiles. Validation required the assembly of a planar laser induced fluorescence (PLIF) test bed for the measurement of I_2 intensity contours and was undertaken at Directed Energy Solutions (DES) in Colorado Springs, CO. The planar laser induced fluorescence (PLIF) technique utilizes an argon ion (Ar+) laser which registers 470mW at 510 nm wavelength. The beam is then shaped into planar sheets and directed into the optical ports of the flow channel. The planar beam excites the injected iodine within the flow which produces fluorescence. The fluorescence can then be captured by a CCD camera. Images were captured in both cross flow and counter flow orientations.

The I_2 is produced by a boiler and directed to the flow via Teflon tubing. The I_2 boiler operates by driving gas flow over I_2 crystals that are heated by heat tape in a glass reservoir. The Teflon tubing is insulated in order to prevent the I_2 from condensing prior to injection into the flow.

There are four mass flow controllers used in the PLIF system. Two of the mass flow controllers regulate the primary flow of helium and nitrogen, which simulates the singlet delta oxygen by molecular weight. Another controller allows a slow flow of helium through the boiler to pick up the I_2 before being combined with the final controller which provides the secondary flow though the nozzles. Four pressure transducers and thermocouples are used to measure the static flow conditions. The pressure transducers and thermocouples are placed at the I_2 boiler, the nozzles, and upstream and downstream

of the throat. The managing of all the controllers, pressure transducers and the thermocouples was handled by LabVIEW 8.0. Figure 2.3 shows the schematic for the PLIF system.

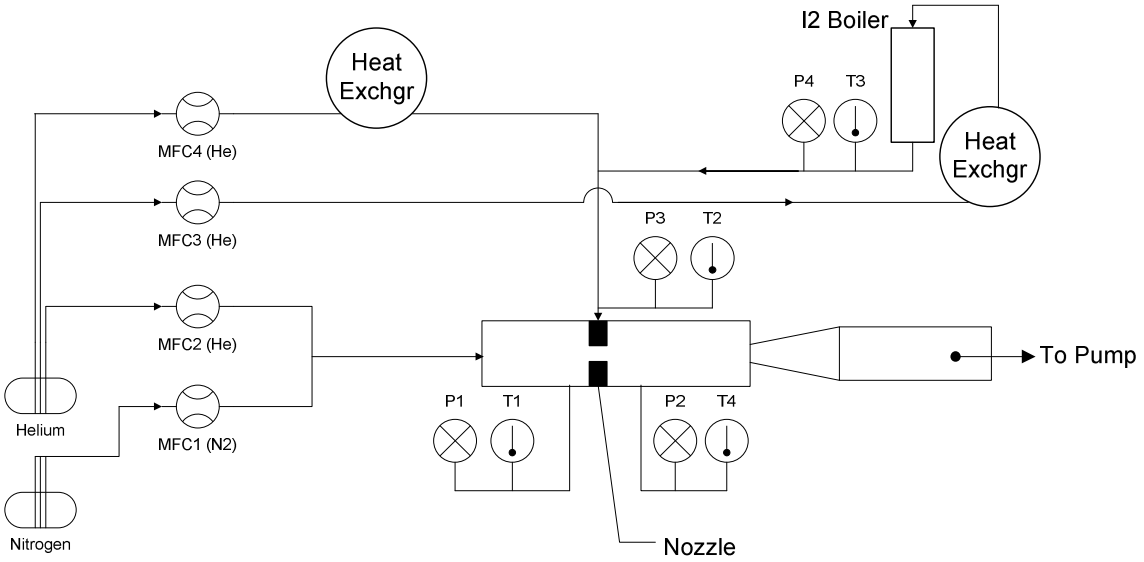

Figure 2.3: Schematic of the PLIF test stand.

PLIF Intensity and Mole Fraction Relationship

For comparison to the CFD calculations, the iodine fluorescence intensity was compared to the I_2 concentrations within the fluid flow. Using the temperature, pressure and iodine concentration at a given point in the fluid domain, the I_2 intensity can be calculated. The non-radiative lifetime is:

$$\frac{1}{\tau_{nr}} = \sigma_s \sqrt{\frac{16\pi}{m_{I2} k_B T}} P_{I2} + \sigma_{He} \sqrt{\frac{8\pi}{\mu_{He} k_B T}} P_{He} + \sigma_{N2} \sqrt{\frac{8\pi}{\mu_{N2} k_B T}} P_{N2} \qquad (12)$$

where m_{I2} is the mass of an iodine molecule, k_B is the Boltzmann constant, $1.38\text{x}10^{-23}$ J/K, the cross-section of the fluorescence quenching for I_2, σ_S, is $60\text{x}10^{-20}\text{m}^2$, the cross-section of the fluorescence quenching for He-I_2 collisions, σ_{He}, is $1.34\text{x}10^{-20}$ m^2, and the cross-section of the fluorescence quenching for N_2-I_2 collisions, σ_{N2}, is $1.34\text{x}10^{-20}$ m^2. The reduced mass for helium and nitrogen, μ_{He} and $\mu_{N2,}$ are 0.00394 kg and 0.0252 kg, respectively [13, 45]. Therefore, for a given temperature, T, and partial pressure for a given species, P_i, τ_{nr} can be solved for at any given point. The radiative lifetime for a flow without collisions, τ_0, is 1.0 μs and the fluorescence yield is:

$$\eta(x,y,z) = \frac{\frac{1}{\tau_0}}{\frac{1}{\tau_0} + \frac{1}{\tau_{nr}(x,y,z)}} \tag{13}$$

and the fluorescence intensity is:

$$F(x,y,z) = \eta(x,y,z) * C[I_2](x,y,z) * I(x,y) \tag{14}$$

where $C[I_2]$ is the concentration of iodine at a given point. Finally, the laser intensity profile is:

$$I(x,y) = e^{\left(-2\frac{x^2+y^2}{w_l}\right)} \tag{15}$$

where w_l is the beam radius. The above equations were incorporated into the CFD program for easy comparison to the experimental results.

Results

The optimization process had a clock time on the order of 4 days. This included 192 total CFD design evaluations. All the computations took place on a HP xw8600 Workstation with 2 - 3.00GHz Xeon Quad Core Processors and 8 GB RAM, which ran in parallel on 6 processors. The results of parameters and Mixedness in listed in Table 2.1.

Table 2.1: Starting and optimal values for each parameter.

Parameters	Starting Conditions	Optimal Conditions	Bounds
Converging Radius	6.35 mm	4.000 mm	4 – 8 mm
Diverging Radius	6.35 mm	4.000 mm	4 – 8 mm
Expansion Radius	20.638 mm	18.580 mm	17 – 22 mm
I_2 inlet Z radius	0.2000 mm	0.2000 mm	0.1 – 0.5 mm
Distance to I_2 inlet	7.000 mm	7.933 mm	4 – 12 mm
Throat	10.000 mm	6.04 mm	6 – 14 mm
Mixedness	0.290	0.670	

A visual comparison of Figure 2.4 (baseline case) and Figure 2.5 (converged improved design) shows the mixing is more complete in Figure 2.5 with only a small central region of lower concentration. The initial geometry started with a Mixedness value of 0.290 and after the automated design tool was applied an improvement of more than two-fold was observed (Mixedness = 0.670).

Several of the parameters proceeded to the lower bounds. For example, the converging and diverging radii both proceeded to the lower bound. However, proceeding further

would result in geometry likely to experience an initial shock wave and other complicating anomalies. The expansion radius decreased moderately. The I_2 inlet remained unchanged from the optimal value determined from the previous injection study [44]. The I_2 inlet distance moved slightly, but the more significant change was the throat diameter. Reducing the throat dimension, while maintaining the same area ratios and velocities yielded improvements in the mixing.

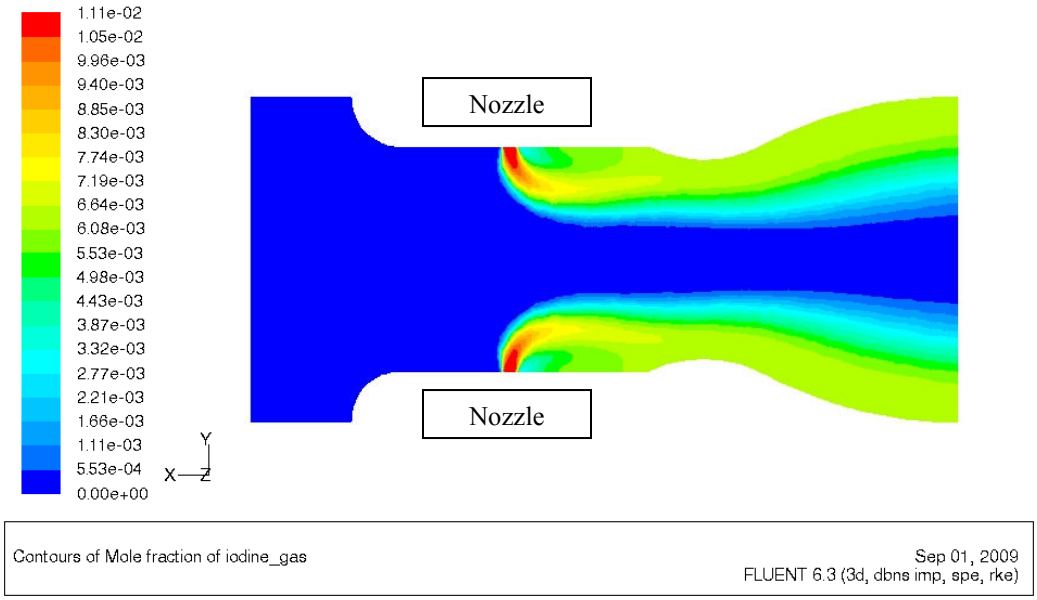

Figure 2.4: Contours of I_2 mole fraction for the start case of the optimization.

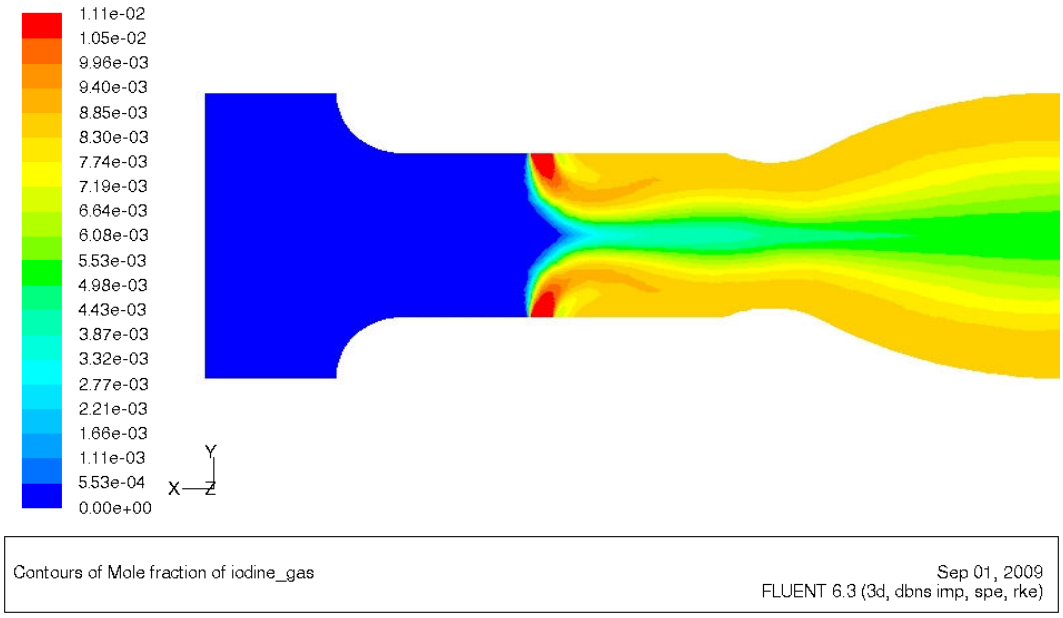

Figure 2.5: Contours of I_2 mole fraction for the optimum case.

Comparison of Numerical and Experimental Results

Validation of the CFD focused on two different nozzle geometries; double and single row I_2 injection geometries. In addition to the different geometries, two different flow parameters were investigated; underpenetrated and fully-penetrated injection. A typical image of fluorescence for an underpenetrated case is shown in Figure 2.6 and Figure 2.7 shows a fully penetrated secondary flow with conditions given in Table 2.2 for both cases.

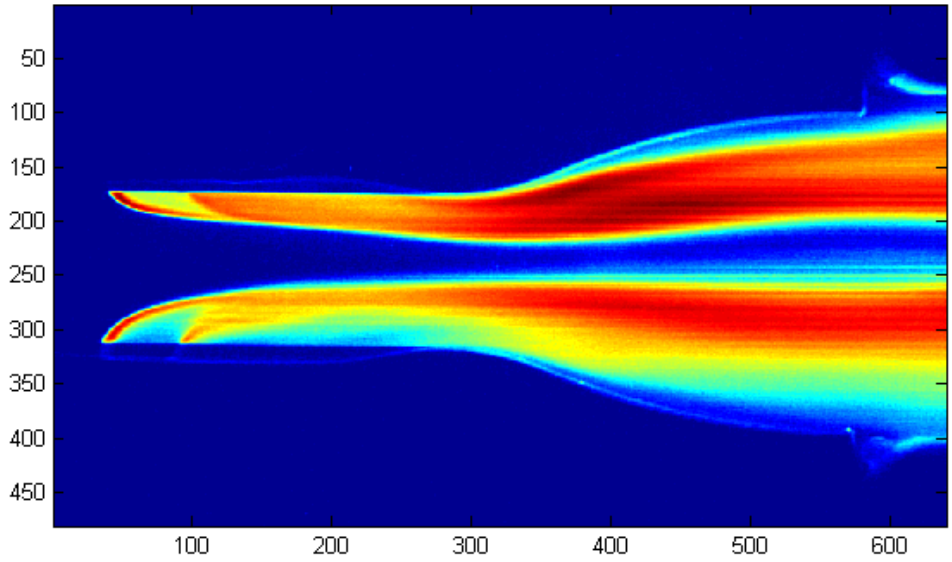

Figure 2.6: PLIF I_2 intensity image of a double row underpenetrated case showing 2 high intensity cores.

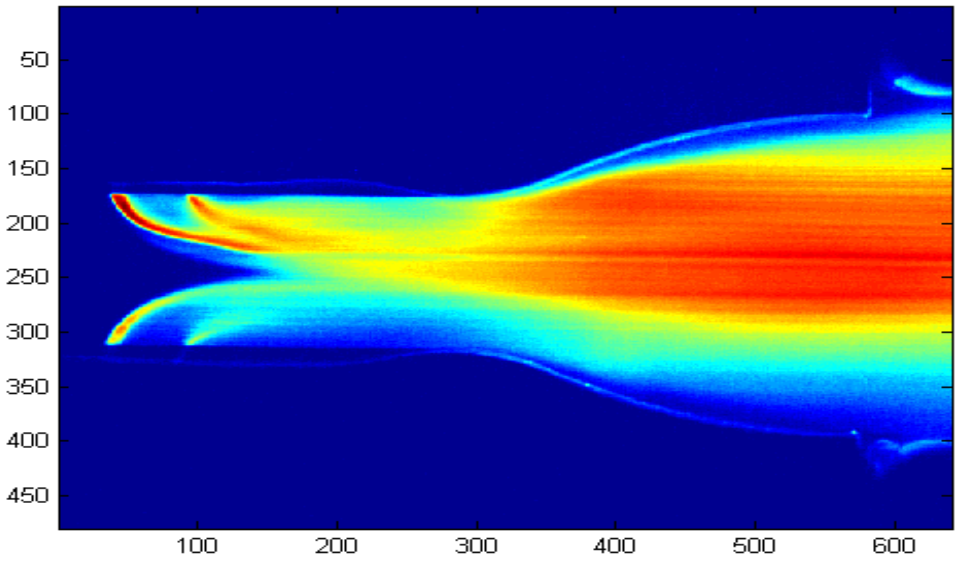

Figure 2.7: PLIF I_2 intensity image of a double row fully penetrated case showing a single high intensity core.

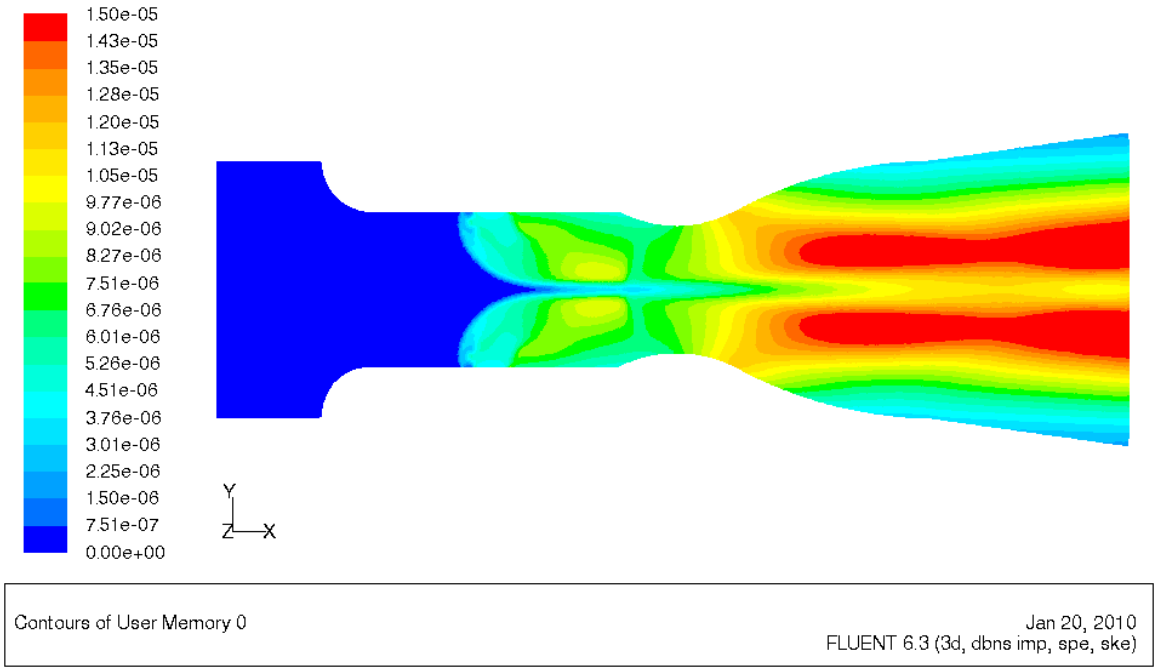

Figure 2.8: CFD fluorescence calculation of a double row underpenetrated case showing 2 high intensity cores.

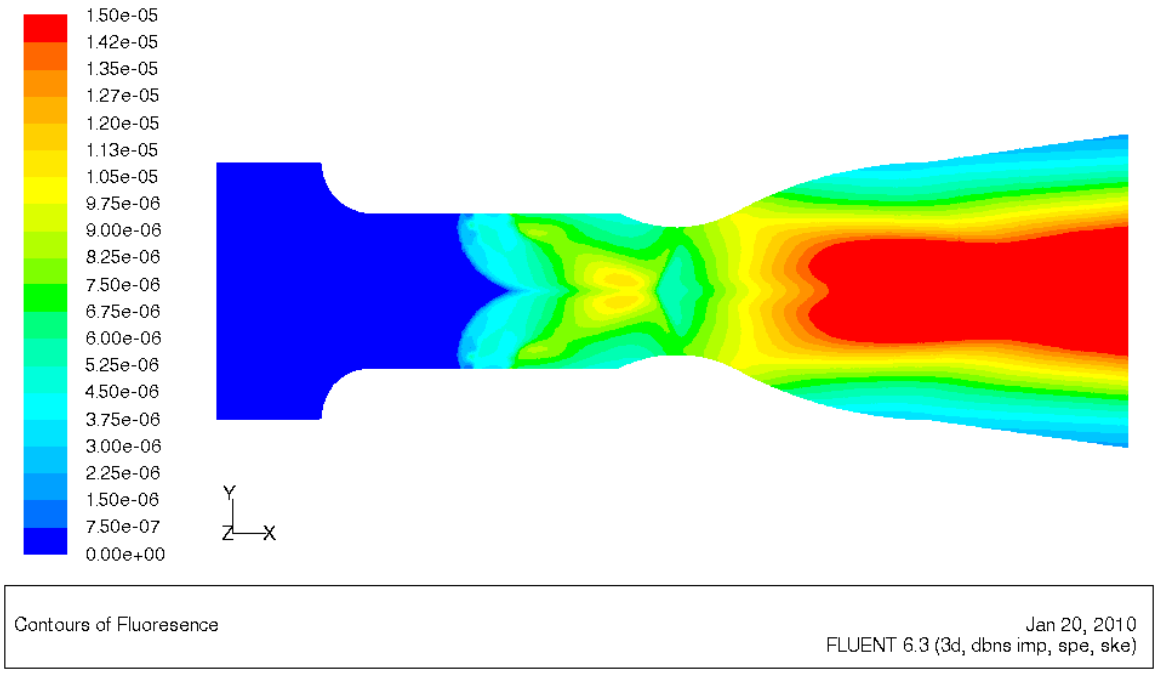

Figure 2.9: CFD fluorescence calculation of a double row fully penetrated case showing a single high intensity core.

Table 2.2: Typical conditions for under and fully penetrated cases. For locations refer to Figure 2.3.

	Under Penetrated Case	Fully Penetrated Case
Chan 1 Press, torr	45.5777	58.2796
Chan 2 Press, torr	3.21417	3.71879
Chan 3 Press, torr	218.231	314.581
Chan 4 Press, torr	182.219	289.829
Chan 1 Temp, K	91.2	93.5
Chan 2 Temp, K	58.2	59.4
Chan 3 Temp, K	27.5	27.6
Chan 4 Temp, K	22.9	26.2
Chan 1 MFC	10.28	10.29
Chan 2 MFC	34.61	34.63
Chan 3 MFC	2	1.99
Chan 4 MFC	4.95	15.06
MACH #	2.41305	2.45393
Pri Avg MolWt	9.49542	9.4971
Sec Avg MolWt	4.14318	4.10685
I_2 Conc, MF	0.0020039	0.0036866
I_2 Conc at noz, MF	0.0005766	0.0004302

Equations 12 through 15 were programmed into the CFD simulations and with the extractions of temperature, pressure, and concentrations, the intensity can be plotted. The results from the CFD simulations for I_2 fluorescence intensity are shown for both the under-penetrated and fully-penetrated cases in Figure 2.8 and Figure 2.9. Visually, it can be seen that the CFD calculations and the PLIF match very well in the supersonic region of the flow, and penetration depth is in good agreement for the subsonic region. Furthermore, Figure 2.10 and Figure 2.11 show the plot comparison between the normalized fluorescence intensities of the experimental data and the CFD calculations for both under-penetrated and fully-penetrated at the outlet plane, respectively. These plots were taken from the double row injection geometry and for both flow conditions.

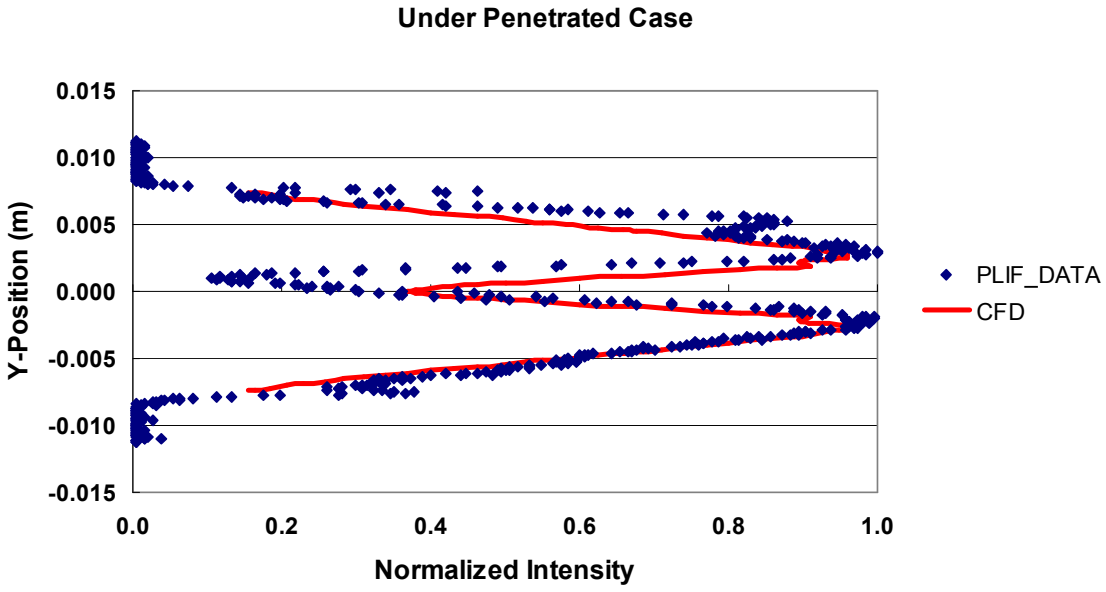

Figure 2.10: Plot comparison of PLIF and CFD calculations of iodine intensities across the outlet plane for an under-penetrated case.

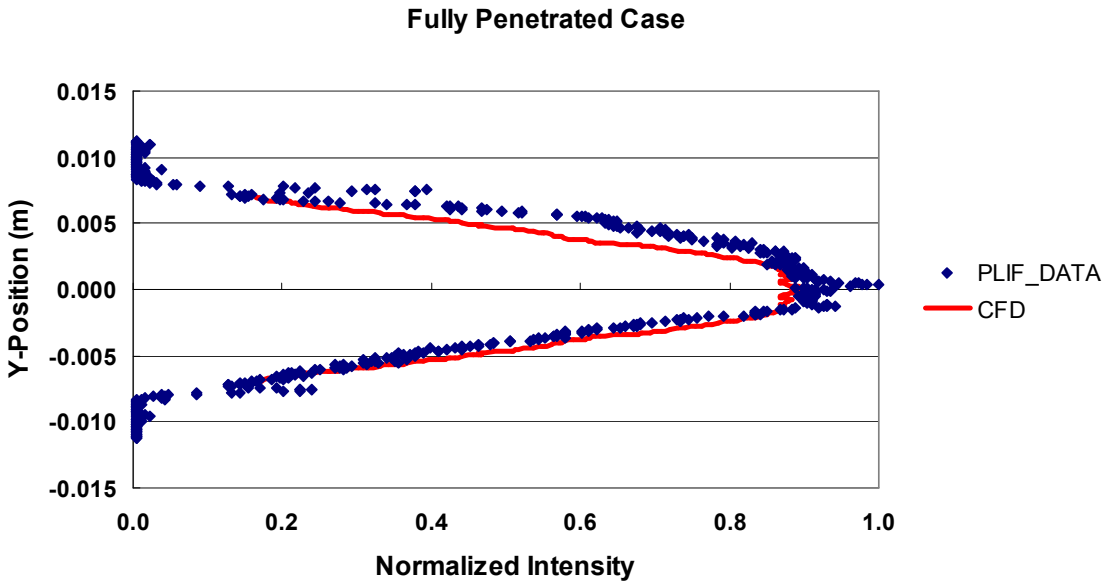

Figure 2.11: Plot comparison of PLIF and CFD calculations of iodine intensities across the outlet plane for a fully penetrated case.

Lastly, a comparison of elliptical I_2 injections with the double row injection nozzle was performed. Figure 2.12 shows that the elliptical inlets have slightly better penetration than the double row injection nozzle when looking at the I_2 mole fractions. Also, it can be observed that there is close agreement between the PLIF experiment and the CFD calculations.

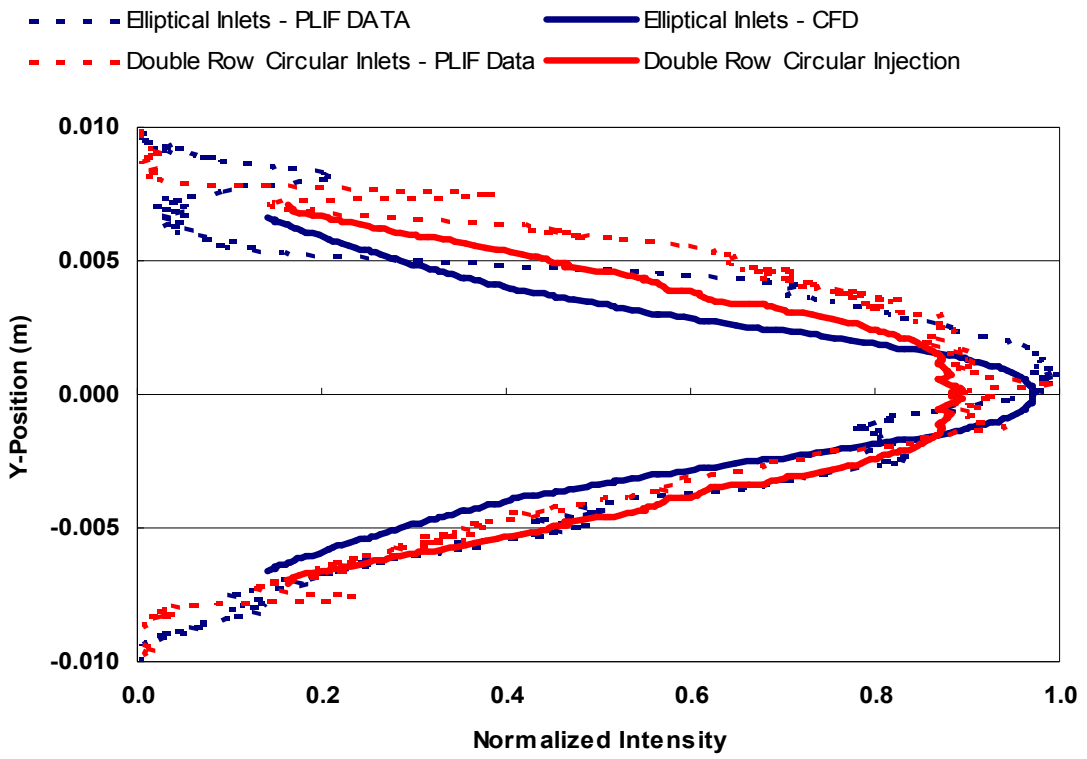

Figure 2.12: Comparison of measured and calculated intensity profiles at the outlet plane for both elliptical and circular inlet holes.

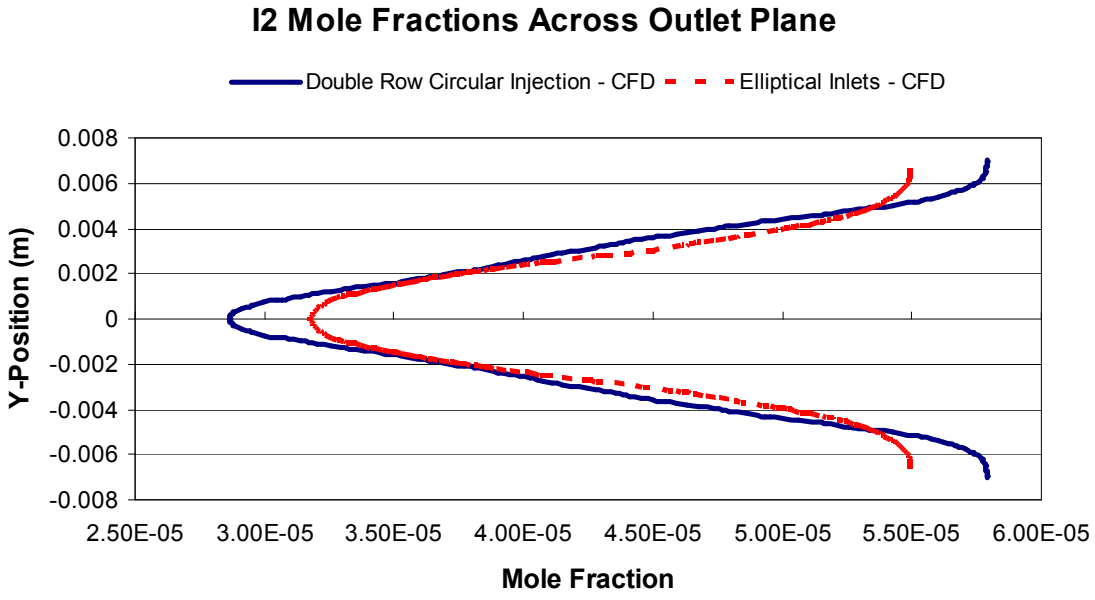

Figure 2.13: The I_2 molar fractions are compared for the elliptical and circular inlet holes.

Conclusions

The accuracy of the fluid dynamic simulations and automated design process to provide physically correct results has been demonstrated through PLIF experimentation. After 4 days of run time and 192 designs the automated tool improved the Mixedness value at the exit of the nozzle from 0.29 to 0.67. The analysis results support the implementation of an elliptical secondary injection port aligned with the direction of the primary flow. This shape and orientation could dramatically enhance the penetration of the jet, allowing for more complete and homogeneous mixing within a short distance. Chapter Three will incorporate these results while adding complexities, such as full chemical kinetics, in order to determine if geometric hot flow optimization will lead to increased laser output power and efficiencies.

CHAPTER 3

SUPERSONIC IODINE MIXING NOZZLE: HOT FLOW OPTIMIZATION

In Chapter Two it was discussed that conventional high-powered, directed energy laser systems utilize a complicated series of chemical reactions to produce the desired laser gain. The COIL relies on the rapid dissociation of molecular iodine into atomic iodine. It is in the gain region that atomic iodine undergoes many energy transfer, excitation, and stimulated emission cycles to extract the energy from the singlet oxygen for lasing. A more efficient laser would not only seek the regions containing the highest gain, but also a uniform distribution across the entire beam area.

The objective of this effort was to apply the automated computational fluid dynamics design tool to a reacting COIL nozzle in order to improve performance and reduce system weight. Compared to the cold flow case, optimization of the gain medium will increase the computational times significantly due to the chemical kinetics (increased number of equations needed to be solved) coupled with a larger fluid design space to allow for the full dissociation of iodine. The fluid domain was extended 10 cm past the nozzle exit plane. To minimize the computational impact, a reduced model was used for the chemical kinetics [46]. The full kinetics package includes 100 reactions and 20 different species [47-49]. Utilizing lessons learned from the cold flow optimization, only one inlet hole was included since it was shown to have a greater penetration than the two hole design.

Numerical Methodology

Nearly identical numerical techniques are utilized here as in Chapter Two, therefore further discussions will only review the differences caused by adding the chemical kinetics and managing the system for a new performance parameter.

Numerical Model

The main modification to the numerical model described in Chapter Two is the addition of chemical kinetics. A reduced kinetics model developed by McDermott et al. [46] includes 10 species and 12 of the most influential reactions present. Table 3.1 provides the species used in the kinetics model along with the concentrations.

Table 3.1: Species and primary flow molar percentages used in the reduced kinetics model.

Species		MW (kg/mole)	Initial Conditions - Percent of total oxygen concentrations	Remarks
1	O2X	0.032000	30%	Ground State O2
2	O2a	0.032000	60%	Singlet Delta O2
3	O2b	0.032000	0	Singlet SigmaO2
4	O2av	0.032000	3%	Singlet Delta O2 Vibrationally Excited
5	I_2X	0.253809	1%	Ground State I_2
6	I_2star	0.253809	0	Ground State I_2 Vibrationally Excited

7	I_2A	0.253809	0	Excited State I_2
8	I	0.126905	0	Ground State I Atoms
9	Istar	0.126905	0	Excited State I Atom
10	HOH	0.018015	12%	Water

The reactions fall into 3 categories: the main reactions, water quenching of excited species, and I_2 dissociation reactions. The first category establishes gain and losses in the "free" iodine atom regime after all the I_2 is dissociated. The second adds additional losses due to water in both the free iodine atom regime. The final category describes the dissociation process. All of these rates and mechanisms are well known and accurately reproduce experimental data [50]. The third category, the iodine dissociation process is an approximation. The reactions and their rate constants are given in Table 3.2.

Table 3.2: I_2 Reactions used in the reduced kinetics model.

Reaction Number	Reaction	Rate(cm3/molecule-s)
Main reactions		
1	O2a + O2a → O2b + O2X	1.20E-16
36	I + O2a → Istar + O2X	7.80E-11
36a	Istar + O2X → I + O2a	7.80E-11/0.75 * EXP(401.42/T)
37	Istar + O2a → I + O2b	1.10E-13
Water quenching		
30	O2b + HOH → O2a + HOH	6.70E-12
35	I2star + HOH → I2X + HOH	1.70E-11
38	Istar + HOH → I + HOH	2.00E-12
I_2 Dissociation		
33	I2X + Istar → I2star + I	3.80E-11
34	I2star + O2a → 2I + O2X	3.00E-10
39	O2av + I2X → O2X + I2A	1.00E-11
40	I2star + O2a → I2A + O2X	1.00E-12
42	I2A + O2a → 2I + O2X	3.00E-10

Even with reducing the chemical kinetics model from 103 reactions to 12, additional modeling techniques had to be used in order to reduce the computational time for the optimization process. This included using an interpolation scheme to provide the best initial guess for the fluid domain prior to the calculation. The interpolation scheme uses

the exported results from a previously converged case (baseline model) and populates the nodes of the new model with those values. Since the boundaries of the new model may not be the same as the interpolated model, any nodes that need to be filled in are assumed to be linear with a gradient that joins the boundary conditions with the nearest interpolated values. For this technique to work, the conservation equations are decoupled based on lower relaxation factors. Once an initial solution is solved for, the under relaxation factors are increased to re-couple the equations for an accurate solution. This process reduced the computational time by 50%-75% depending one the differences between the new case with the baseline solution.

Problem Description

For hot flow, the gain was chosen as the performance parameter. The gain medium arises from spontaneous emission and provides the amplification of light. More importantly than optimizing to the maximum gain, is optimizing to the uniformity of gain as it enters the gain region (10 cm downstream of the nozzle exit). Therefore, the gain uniformity described below was used:

$$GM = 1 - \frac{\sum_n \left(gain_n - gain_{perfect} \right)}{N * gain_{perfect}} \tag{16}$$

where GM is the gain uniformity, $gain$ is the calculated gain, $gain_{perfect}$ is the gain with perfect mixing, and N is the total number of nodes used in the calculation.

The difficulty is estimating the gain at perfect mixing as it exits the nozzle region. Assuming the oxygen yield, cavity temperature, and iodine concentration are uniform, then the gain can be given by [51]:

$$gain_{perfect} = 0.5 * \sigma * N_{I2} * \frac{\left[(2 * K(T) + 1) * Y_{cav} - 1\right]}{\left[(K(T) - 1) * Y_{cav} + 1\right]} \quad (17)$$

where $K(T)$ is the equilibrium constant, Y_{cav} is the yield of oxygen at the cavity, T is the temperature, N_{I2} is the average iodine molar concentration (moles/cm^3), and σ is the small signal gain cross section.

The average cavity yield is somewhat dependent on losses in the flow. One loss is pooling, which is fairly small. Another is the cost of dissociating the iodine, which is usually empirically set to a constant N_{diss} (~5) times the total iodine dissociated. N_{diss} is the number of $O_2(^1\Delta)$ required to dissociate one I_2. The cavity yield is then given by:

$$Y_{cav} = Y_{NIP} - Y_{diss} \quad (18)$$

where Y_{NIP} is the yield at the nozzle inlet plane. For a simple set of input parameters a sample calculation is shown below in Table 3.3.

Table 3.3: Sample *gain $_{perfect}$* calculation.

INPUTS IN BOLD	
T	200 K
Ynip	60%
dissF	100%
mO2	0.9 moles/s
mHep	3.6 moles/s
mHes	1.8 moles/s
I_2 Flow	0.009 moles/s
Pcav	5 torr
Rgas	62400 torr-cm3/(K-mole)
Ndiss	5
mdot	6.309 total moles/s
K(T)	5.58 equilibrium constant
sig	9.51E+06 1/cm
xO2	14.27%
xI2	0.14%
N	4.01E-07 moles/cm3
NI2	1.14E-09 moles/cm3
Yd	0.05
Ycav	0.55
$gain_{perfect}$	0.88% 1/cm

Gain, which is the calculated value from the CFD, is going to be a function of the parameters that will be perturbed during the optimization process. All of the other parameters will be held constant during the analysis. The parameters that will be investigated are:

1. Converging Radius
2. Diverging Radius
3. Expansion Radius
4. Radius in the Z-direction of the I_2 inlet (with a fixed cross sectional area, this provides the aspect ratio)
5. Distance of I_2 inlet from the leading edge
6. Pressure of the I_2 inlet

These are the same as those investigated in the cold flow simulation with the exception of the throat dimension. For this case the throat distance will be constant and instead the I_2 inlet pressure will be varied. Varying the I_2 pressure allows for the change of the penetration depth, similar to changing the throat, and is more practical to modify in the physical system. The same bounds as the Mixedness case were set for the geometric parameters, 1 through 5. Just to reiterate, the bounds were determined by physical constraints and limitations. I_2 inlet boundary, on the other hand, is based off the initial geometric constraints provided to us by DES and/or the Missile Defense Agency (MDA). The pressure was given bounds that would allow a range for both under and over penetration. The lower and upper bounds and initial starting point for the optimization are listed in Table 3.4. The flow conditions for the CFD simulation are given in Table 3.5.

Table 3.4: Design parameters with bounds.

Parameters	Starting Conditions	Lower Bounds	Upper Bounds
Converging Radius	6.35 mm	4.000 mm	8.000 mm
Diverging Radius	6.35 mm	4.000 mm	8.000 mm
Expansion Radius	20.638 mm	17.000 mm	22.000 mm
I2 inlet Z radius	0.1500 mm	0.1000 mm	0.3075 mm
Distance to I2 inlet	7.000 mm	4.000 mm	12.000 mm
I_2 Inlet Pressure	250.000 torr	250.000 torr	500.000 mm

Table 3.5: Flow conditions for the hot flow optimization.

Primary Inlet	
Pressure	47.6 torr
Temperature	350 K
Species Mass Fraction, O_2	0.260
Species Mass Fraction, O_{2a}	0.371
Species Mass Fraction, O_{2av}	0.020
Species Mass Fraction, H_2O	0.044
Species Mass Fraction, He	0.345
Avg. Mol. Wt.	10.102 gm/mol
Mass Flow Rate	6.642E-6 kg/s
Secondary I_2 Inlet	
Pressure	250 torr
Temperature	387 K
Species Mass Fraction, I_2	0.266
Species Mass Fraction, He	0.734
Avg. Mol. Wt.	5.426 gm/mol
Mass Flow Rate	4.618E-6 kg/s

Results

The optimization routine ran for more than two months before it reached convergence. The average run time for each of the 82 designs evaluated was ~16 hours. The process was carried out on 32 - Intel Xeon Quad Core processors at 3.00GHz running XP-64bit OS and 32 Gb total RAM. The convergence criterion for the optimization routine was to keep the gain uniformity and variable perturbation from changing with a tolerance of 1E-3 for two consecutive iterations.

A contour plot of the gain for the starting conditions is shown in Figure 3.1; these conditions resulted in a gain uniformity of 0.644. For the optimal conditions the gain uniformity increased by ~42% to 0.914. The contour plot for the optimal conditions is in Figure 3.2.

Table 3.6 has the starting and optimal values for each parameter. The maximum gain region moved downstream from the throat region towards the exit. In addition the uniformity also increased across the outlet face. Some interesting findings are that the I_2 inlet hole proceeded to a circular shape instead of an elliptical shape, which was found by the Mixedness optimization. This likely means that the shape of the inlet hole has little effect on the gain since the calculation for gain uniformity is so far downstream. If the gain region could be moved up stream, for example in a scenario where the optical resonator would be positioned close to the nozzle bank, the shape of the inlet hole would have more of an impact on the optimization and likely proceed back to an elliptical shape. The location of the I_2 inlet also became important, whereas with the Mixedness it was not. The optimal location found was furthest from the throat, which allowed for more of the I_2 to dissociate prior to reaching the throat. The converging and diverging radii remained symmetrical but reduced in radius and the expansion radius increased.

At first glance one may notice that 5 of the 6 parameters hit boundary values. It is more important to recognize that all 6 parameters moved from the initial position and many moved full range demonstrating the significance of each on the performance parameters. In fact their value is highly dependent on where you desire to make the gain measurement.

Based on the optimization a local minimum was found, but one may inquire about the global minimum and whether or not it differs from the minimum found. The downside to any global optimization investigation is the computation time to convergence is much greater than a gradient-based optimization finding a local minimum. Since the faster gradient-based optimization took over 2 months to run and the performance parameter increased by ~42%, the improvement was considered more than satisfactory. Another approach to investigate the design space would be to generate a Design of Experiments (DOE). If a simple DOE was examined where all six parameters had a uniform spacing within the bounds, generating 10 different values, the total number of simulations would be 10^6, which is not practical to run. However the optimization results did produce a real minimum that does lead to improved performance.

Additionally, it is important to verify that the optimized design yielded better results that the original baseline geometry and that the decision to remove the second row in I_2 injection holes was appropriate. The conditions used for the baseline geometry (double row injection) were identical to the hot flow conditions and the starting point of the optimization given in Table 3.6. The gain contour plot for the original nozzle is shown in Figure 3.3 and had a gain uniformity value of 0.595. It can be seen that there was a 4.6% improvement from the starting optimization nozzle and a 27% improvement from the final optimized nozzle compared to the baseline nozzle. Figure 3.4 shows the gain across the outlet plane at which the gain uniformity calculation was executed. It can be seen that the optimized nozzle design has a better gain profile both in terms of uniformity, as well as, increased value.

Table 3.6: Starting and optimal parameter values compared to the baseline case.

Parameters	Starting Conditions	Optimal Conditions	Baseline Conditions
Converging Radius	6.35 mm	4.000 mm	6.35 mm
Diverging Radius	6.35 mm	4.000 mm	6.35 mm
Expansion Radius	20.638 mm	22.000 mm	20.638 mm
I2 inlet Z radius	0.1500 mm	0.3075 mm	0.254 mm and 0.127mm (double row injection)
Distance to I2 inlet	7.000 mm	4.000 mm	7.000 mm
Pressure	250.000 torr	315.549 torr	250.000 torr
Gain Uniformity	0.644	0.914	0.598

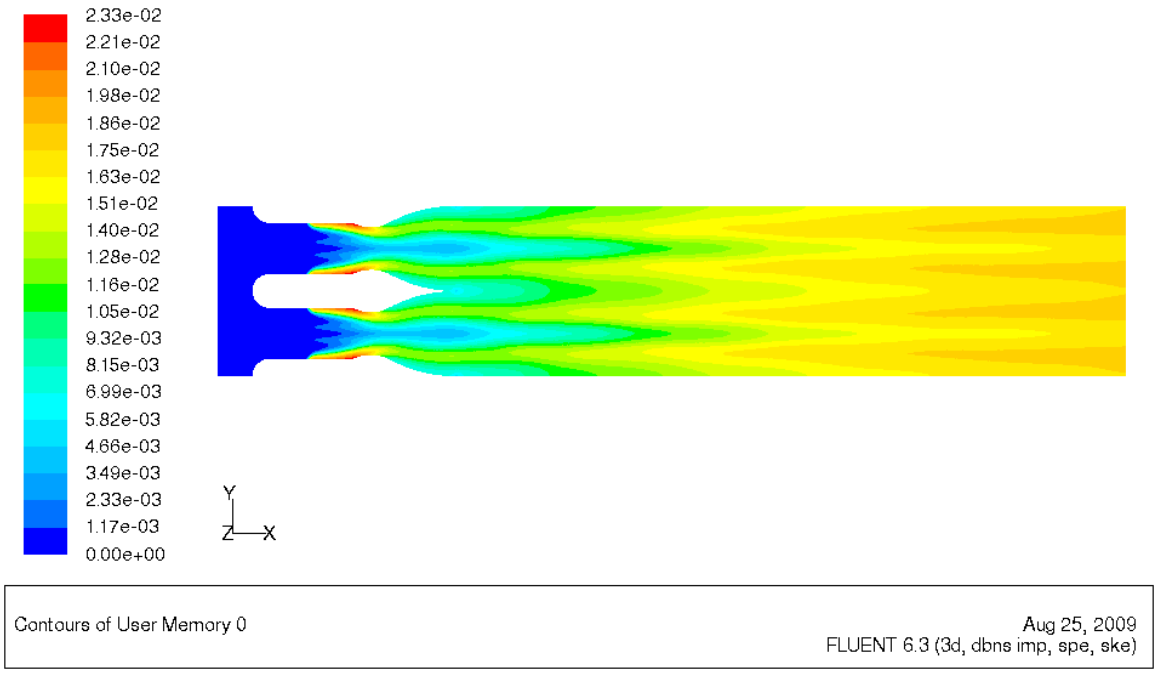

Figure 3.1: Contours of the gain for the initial conditions of the optimization.

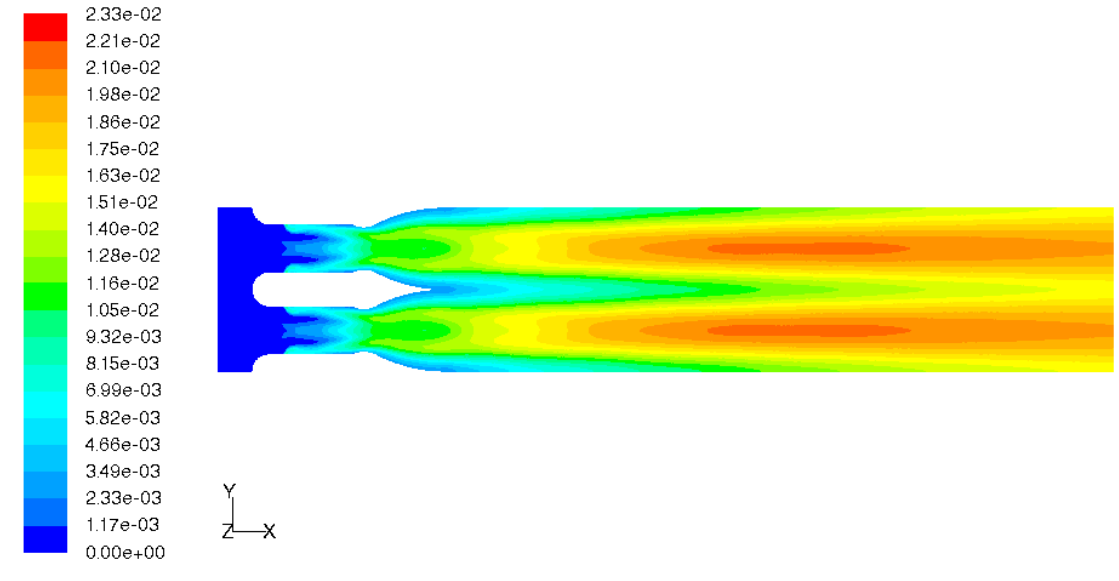

Figure 3.2: Contours of the gain for the best case (of the 80 simulations) conditions of the optimization.

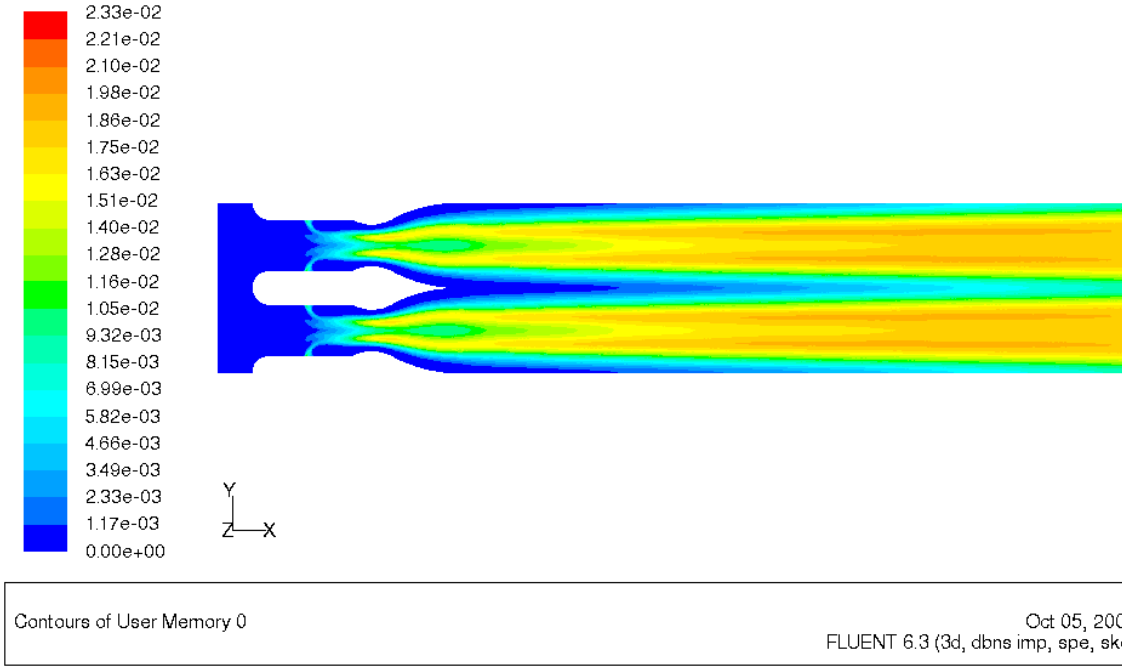

Figure 3.3: Contours of the gain for the double row circular injection nozzle design.

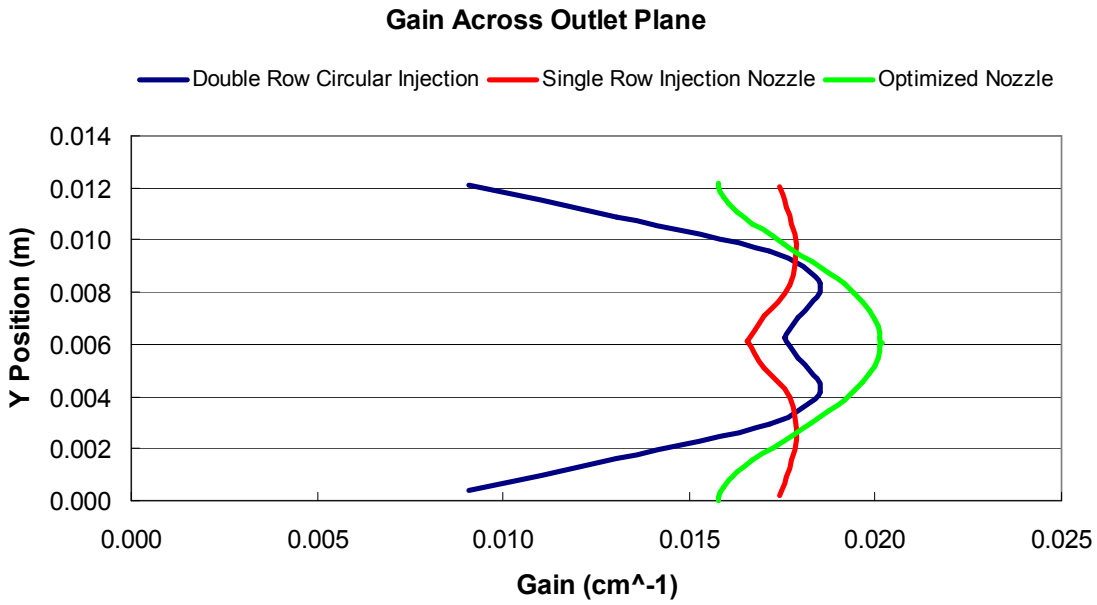

Figure 3.4: Comparison of the gain across the outlet plane for the original nozzle, starting nozzle of the optimization, and the final optimized design.

The next series of plots is to show that the kinetics model is properly calculating the iodine dissociation. These plots are taken from the optimized design. The molar fraction of each species will be presented.

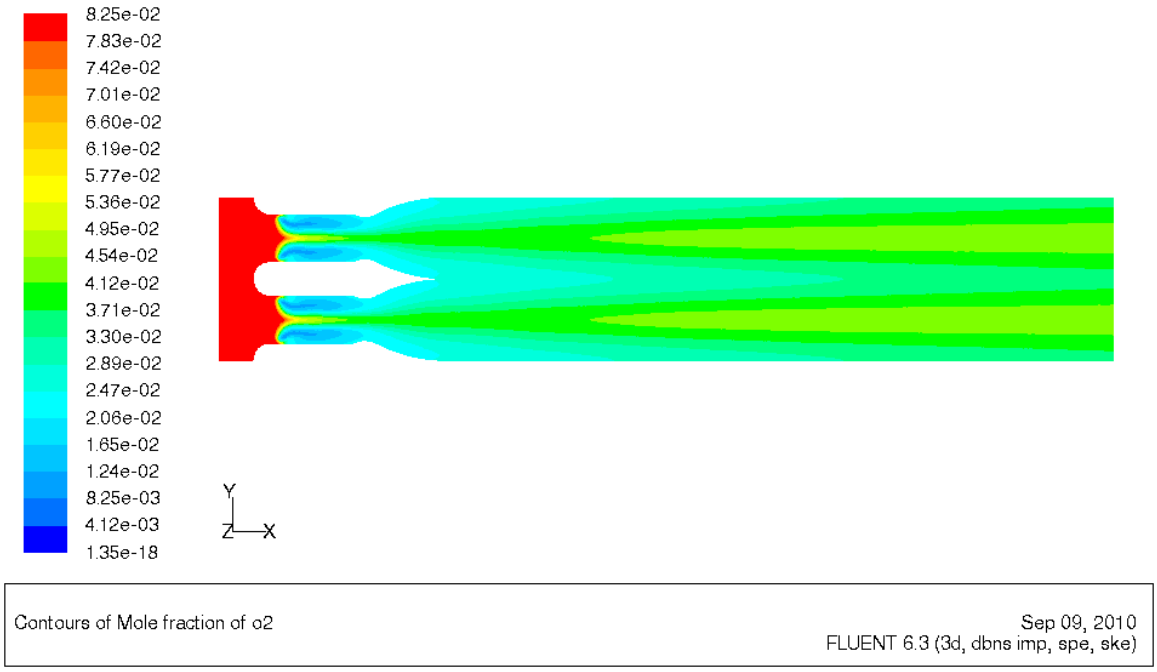

Figure 3.5: Molar fraction of ground state oxygen (O_2).

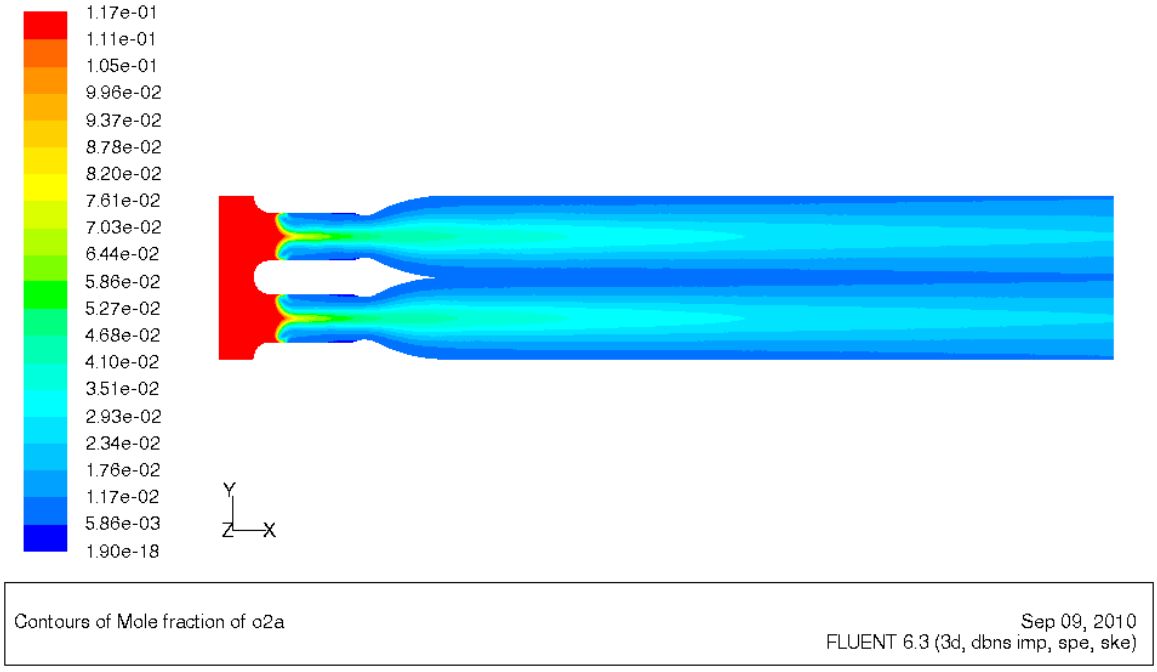

Figure 3.6: Molar fraction of singlet delta oxygen (O_2a).

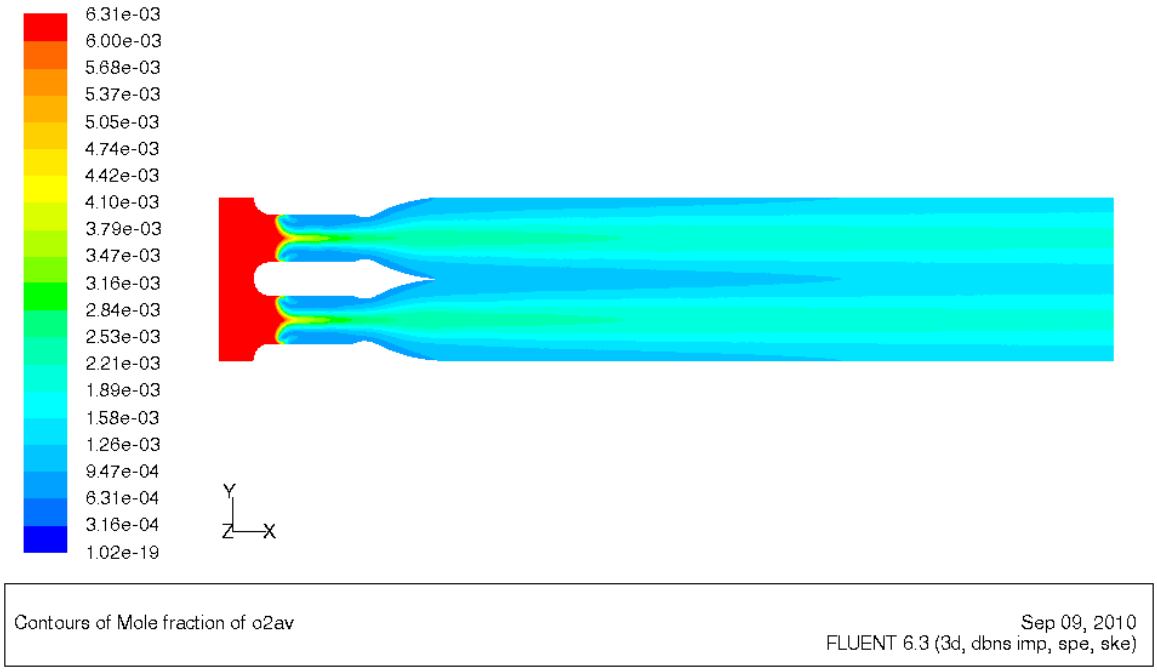

Figure 3.7: Molar fraction of vibrationally excited oxygen (O_2av).

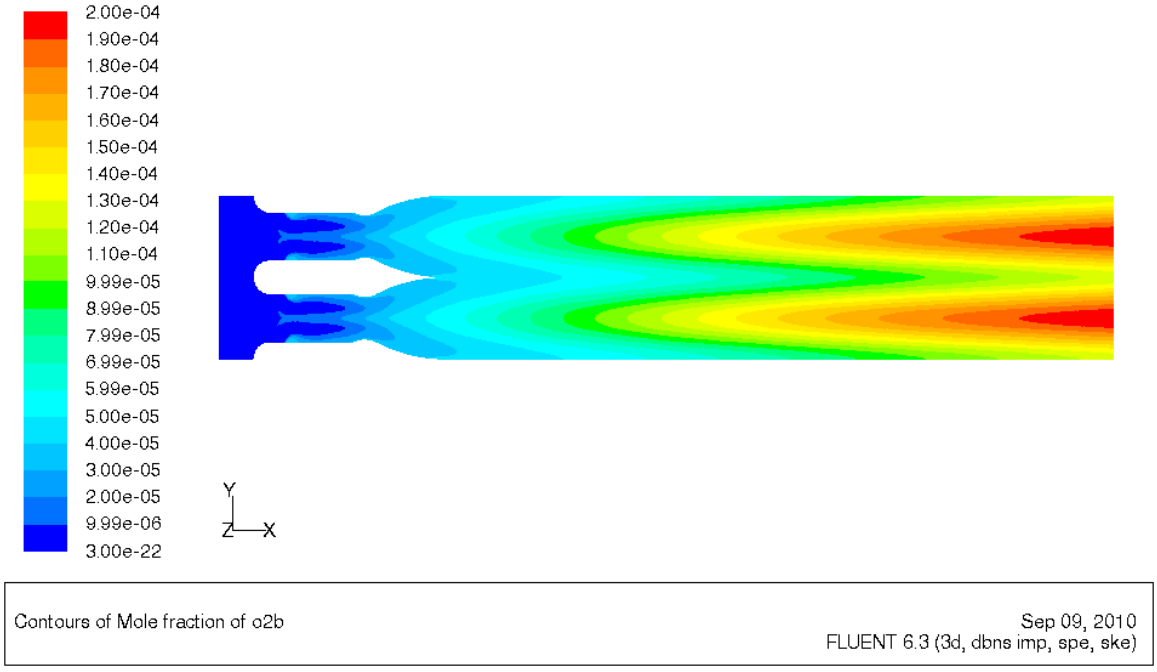

Figure 3.8: Molar fraction of singlet sigma oxygen (O_2b).

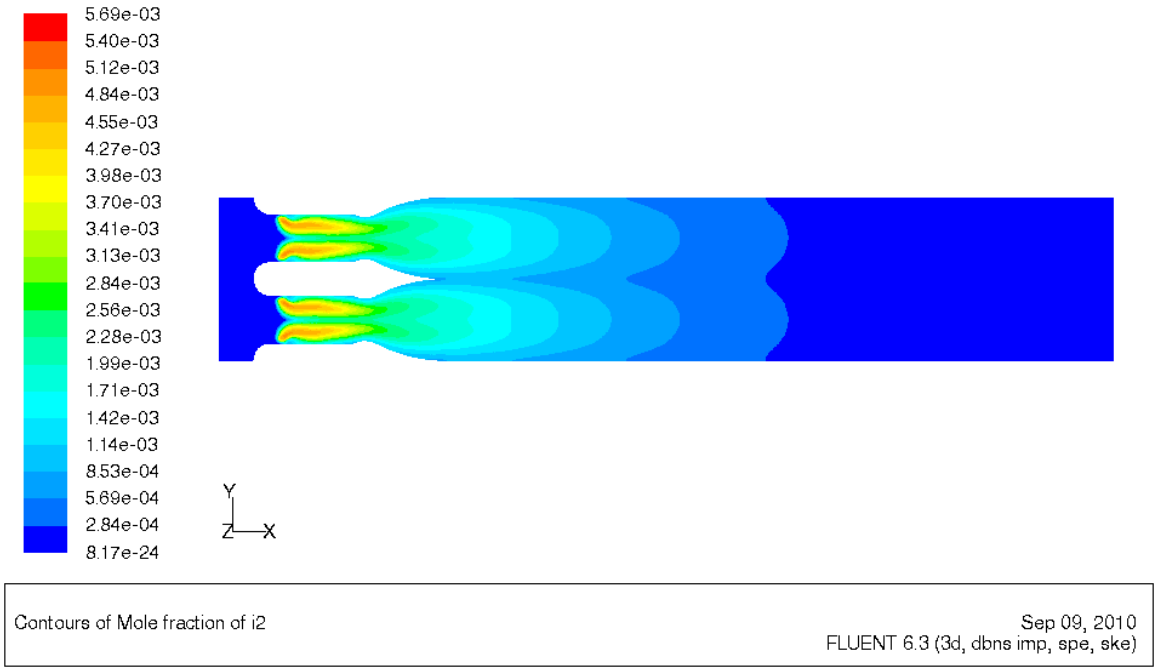

Figure 3.9: Molar fraction of ground state iodine (I_2).

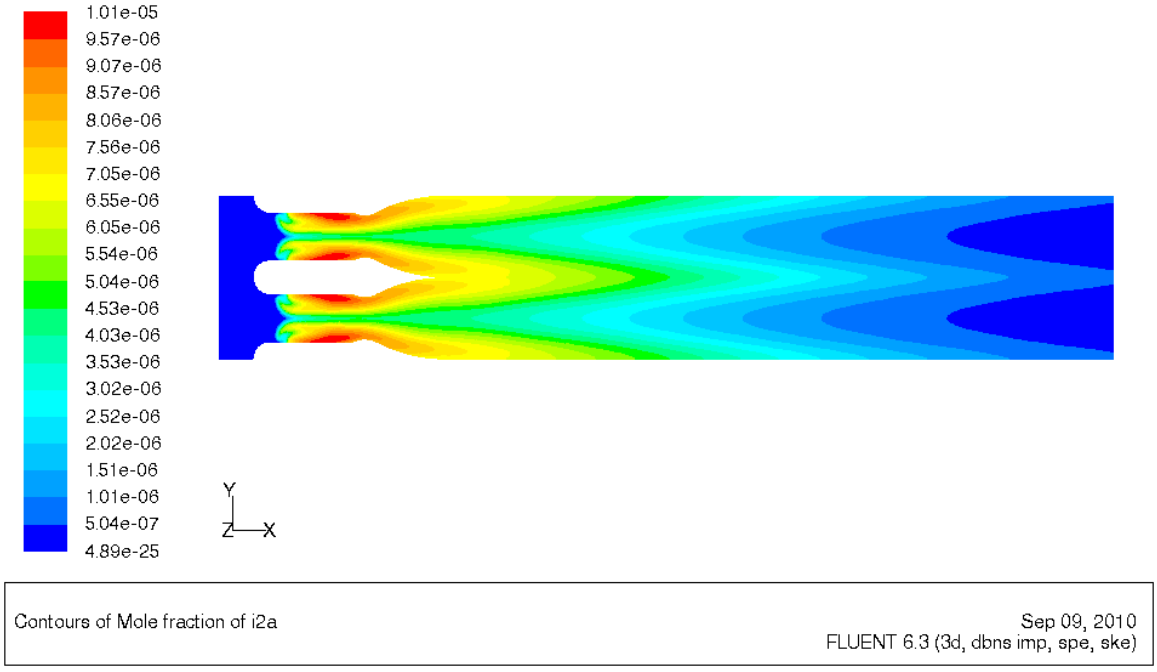

Figure 3.10: Molar fraction of exited state of iodine (I_2a).

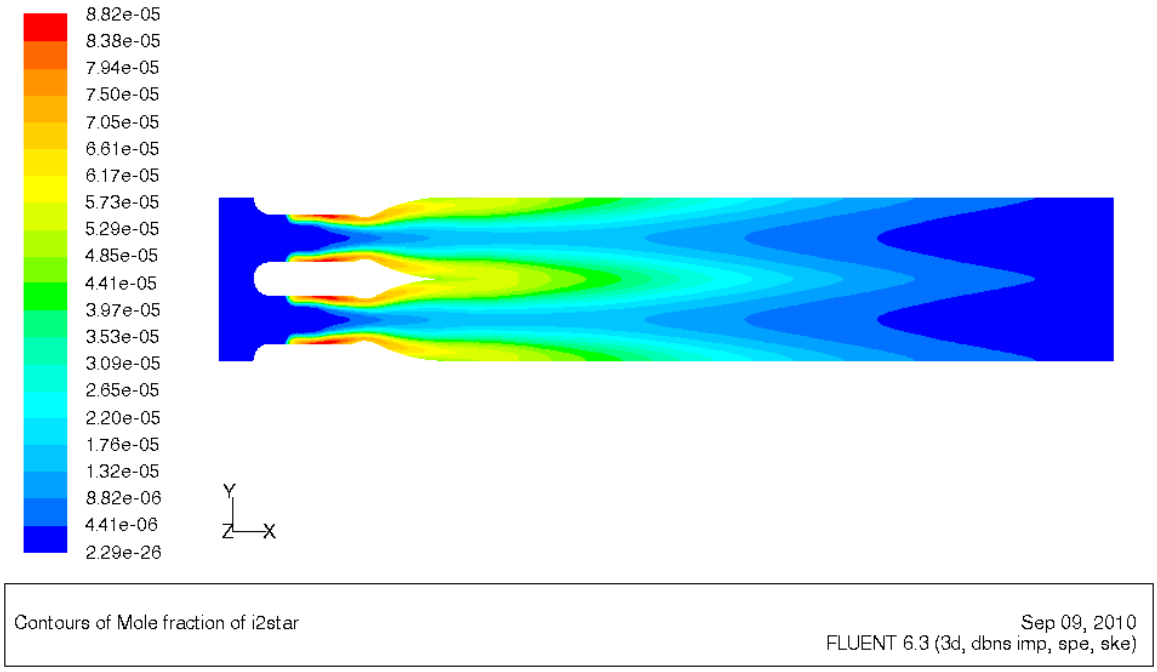

Figure 3.11: Molar fraction of vibrationally excited ground state iodine (I_2^*).

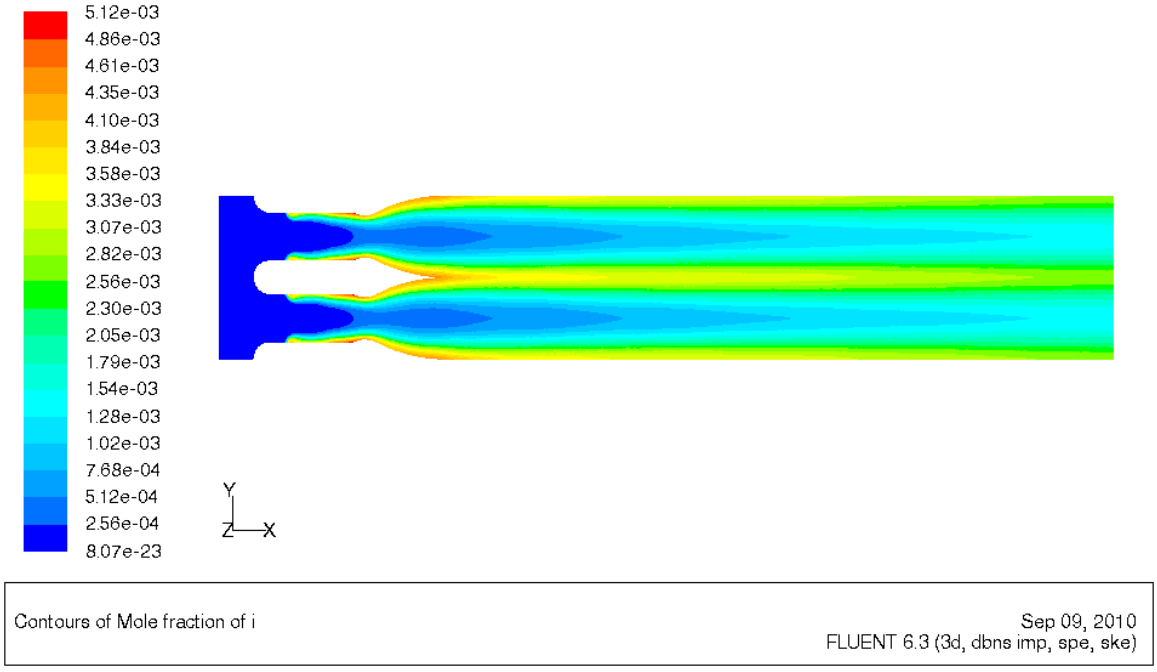

Figure 3.12: Molar fraction of ground state atomic iodine (I).

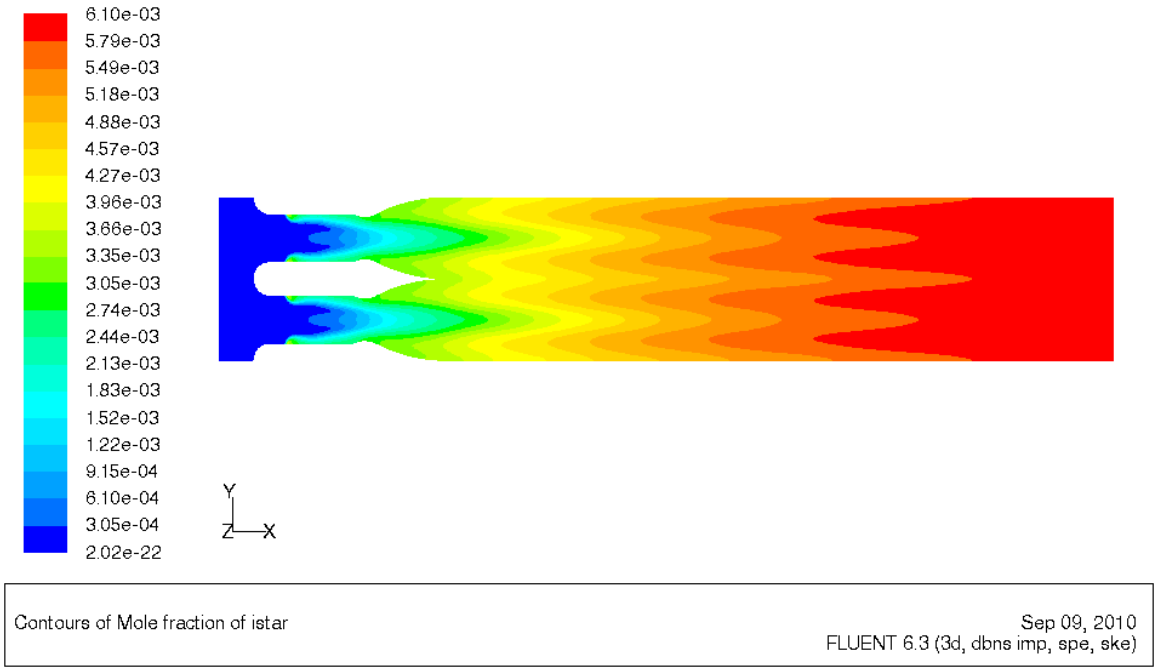

Figure 3.13: Molar fraction of excited state of atomic iodine (I^*).

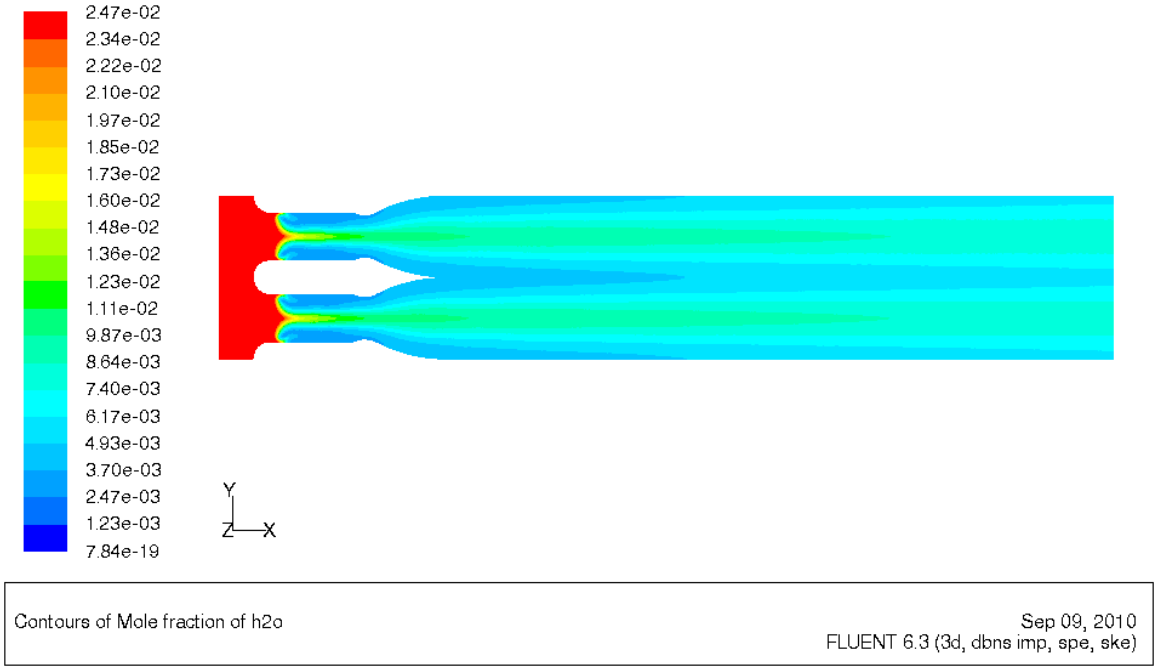

Figure 3.14: Molar fraction of water molecules (H_2O).

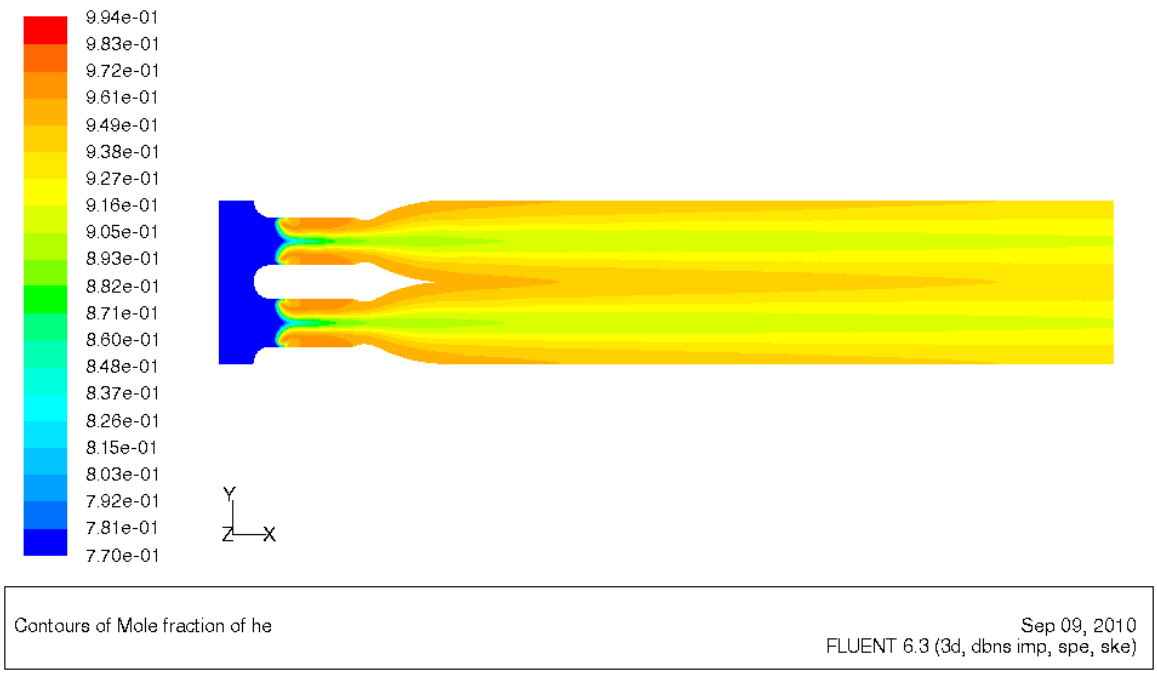

Figure 3.15: Molar fraction of helium molecules (He).

It is important to see that the ground state of iodine that is injected into the primary flow is being fully dissociated. This can be seen in Figure 3.9 where the iodine is fully dissociated about half way down the fluid domain.

Conclusions

The first part of this investigation was to improve on the supersonic mixing nozzle design. An optimization technique coupled with sophisticated CFD simulations was performed for a reacting flow. The gain was calculated and optimized to uniformity along the outlet plane. The analysis exceeded two months and required over 80 simulations to converge on a solution. It was carried out on a cluster of 5 Workstations and 32 processors running 64-bit Windows XP. The gain uniformity increased by approximately 42%, which means that the gain profile across the outlet plane was more uniform than both the starting point of the optimization and the baseline nozzle with double row

circular injection. Also for completeness, Table 3.7 shows the average gain and mixing efficiency based off of Equation 10.

Table 3.7: Average gain and mixing efficiency improvements.

	Double Row Circular Injection	Single Row Injection	Optimized Nozzle
Average Gain (1/cm)	0.0155	0.0174	0.0181
η_{mix}	48%	66%	75%

Essentially, the improvements made to the mixing and gain distribution will lead to an increase in beam quality and power. However, the goal is to reduce weight of the system. Remember that the ABL has 6 COIL modules needed to meet their power requirements. With the optimized nozzle design their lies a potential to remove several modules since more power can be extracted at an improved beam quality. The weight saving is increased even more with the removal of the massive PRS that corresponds to each COIL module no longer needed.

CHAPTER 4

SUPERSONIC IODINE MIXING NOZZLE: CONTOUR OPTIMIZATION

In Chapter Three it was shown that the design process was successful for improving gain uniformity though optimization. However, there was a simplification that must to be explored further in order to continue to improve the overall performance of the mixing nozzle. The gain simply corresponds to the concentrations of the species in the fluid. With any supersonic nozzle the shocks and expansion and compression waves are always a concern and should be minimized. For the previous optimizations, the expansion curvature of the mixing nozzle was modeled as a circular radius. In order to reduce the intensity of the shocks, a higher order curvature will be explored and may lead to further flow uniformity.

The objective of this effort was to apply the optimization design tool to a 2D COIL nozzle investigating higher order curvatures and how it will affect flow uniformity. Compared to the previous cases, this optimization will require lower computational times due to only being 2D and non-reacting. Utilizing lessons learned from the previous optimizations, the baseline nozzle will be the hot flow optimized nozzle.

Numerical Methodology

Nearly identical numerical techniques are utilized here as in Chapter Two, therefore further discussions will only review the differences in the simulations.

Numerical Model

Previous optimizations have simplified the expansion curvature as a circular arc. This simplification was sufficient when looking at mixing and gain uniformity, since they are calculated from the concentrations of species. However, when considering the quality of the flow field and minimizing shock structures, higher order curvatures need to be investigated. To explore this further, an optimization case was executed looking at 3rd order curvatures. For the investigation of the expansion curvature, only a 2D model has to be simulated. The fluid mixture will be the same as the cold flow analysis from Chapter Two; helium, nitrogen, and iodine. This mixture is used to be similar to the actual fluid characteristics (molecular weight, viscosity, etc.) of the full set of species. Additionally, the fluid domain for the simulations will only include the nozzle, since the concern is the flow uniformity at the nozzle exit.

Problem Description

In order to create a uniform flow at the exit of the nozzle, the majority of the flow must be in the x-direction. Therefore, the objective function can simply minimize the change of velocity in the y-direction. Figure 4.1 and Table 4.1 provides the contour of the mixing nozzle and the variables to be optimized, respectively.

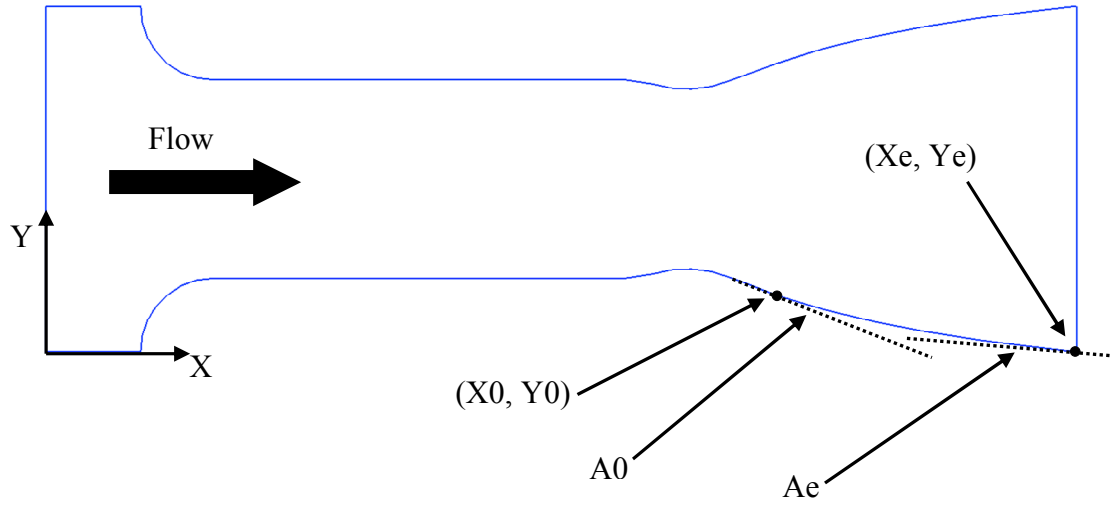

Figure 4.1: Mixing nozzle indicating the parameters that describe the 3rd order polynomial for the expansion curvature.

Table 4.1: The 3rd order polynomial used six inputs of which two will be varied during the analysis.

Inputs	Values	Remarks	Range
X0	X-Coordinate of the tangent location of the C-D curvature	Fixed point	NA
Y0	Y-Coordinate of the tangent location of the C-D curvature	Fixed point	NA
A0	Angle of the tangent location for the start of the polynomial	Variable for optimization	20 – 25 degrees
Xe	X-Coordinate of the nozzle exit	Fixed point	36.36 mm
Ye	Y-Coordinate of the nozzle exit	Fixed point keeping the Mach design point	NA
Ae	Tangent angle at the nozzle exit	Variable for optimization	4 – 8 degrees

Using these points along with the angles, the coefficients for a 3rd order polynomial can be solved:

$$Y = aX^3 + bX^2 + cX + D \tag{19}$$

Using these coefficients and incrementing the X between X0 and Xe, the Y locations corresponding to each X can be solved and plotted. Notably for the first analysis, the Xe dimension was fixed to the maximum dimension that would result in the longest nozzle that could be used in a small scale COIL device currently being built by industry collaborators. This is so that any potential benefits of the optimization can be readily implemented into the nozzle banks without modifying any other hardware.

The objective function will be calculated from the y component of the velocity vectors, υ, at the outlet of the nozzle. If the flow is perfectly uniform in profile, the y velocity vectors would all be equal to zero. The minimization of the objective function is given below:

$$\min F = \frac{\sum |\upsilon|}{n * |\upsilon_{\max}|} \tag{20}$$

From the CFD the y component of velocity vectors, υ, will be exported across the nozzle exit plane. The nodal average, where n is the total number of nodes on the nozzle exit plane, will then be normalized by the maximum of the absolute value of the y component velocity vector.

Results

The optimization routine ran for about 24 hours before it reached convergence. The average run time for each of the designs evaluated was 20 minutes. The process was carried out on 8 - Intel Xeon Quad Core processors at 3.00GHz running XP-64bit OS and 8 Gb total RAM. The convergence criterion for the optimization routine was the difference of 1E-3 in flow uniformity and variable perturbation for two consecutive iterations.

For the conditions described in Table 4.1, the resulting optimization found that minimum occurred at 22.24 and 4 degrees for A0 and Ae, respectively. A surface plot showing the minimization of the objective function based on the perturbation of Ae and A0 is provided in Figure 4.2.

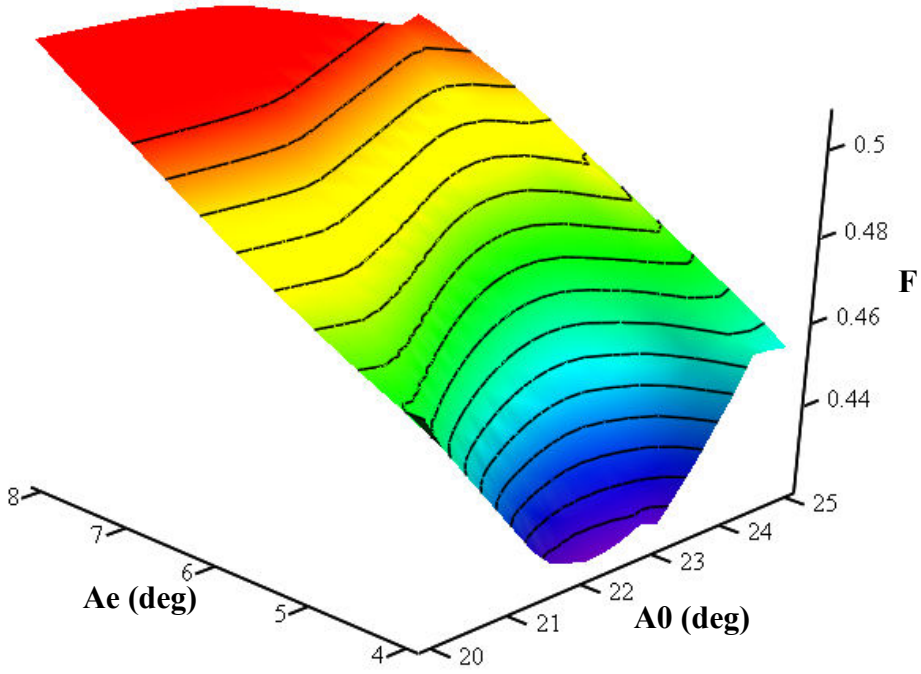

Figure 4.2: Surface plot showing the performance where the minimum lies at an exit angle equal to 4 degrees.

Noticing that the Ae hit the bottom of the range set for the optimization, the angle was extended to 0 degrees and rerun. The new minimum occurred at 23.46 and 0.002 degrees for A0 and Ae, respectively. Figure 4.3 shows the surface plot from extending Ae to 0 degrees. It is interesting to note that both the Ae and A0 values changed and the path of the minimization of the objective function changed. Figure 4.4 shows a comparison of the different contours, original baseline (RotoCOIL), Gain Uniformity Optimized from Chapter Three, and the Flow Uniformity Optimization.

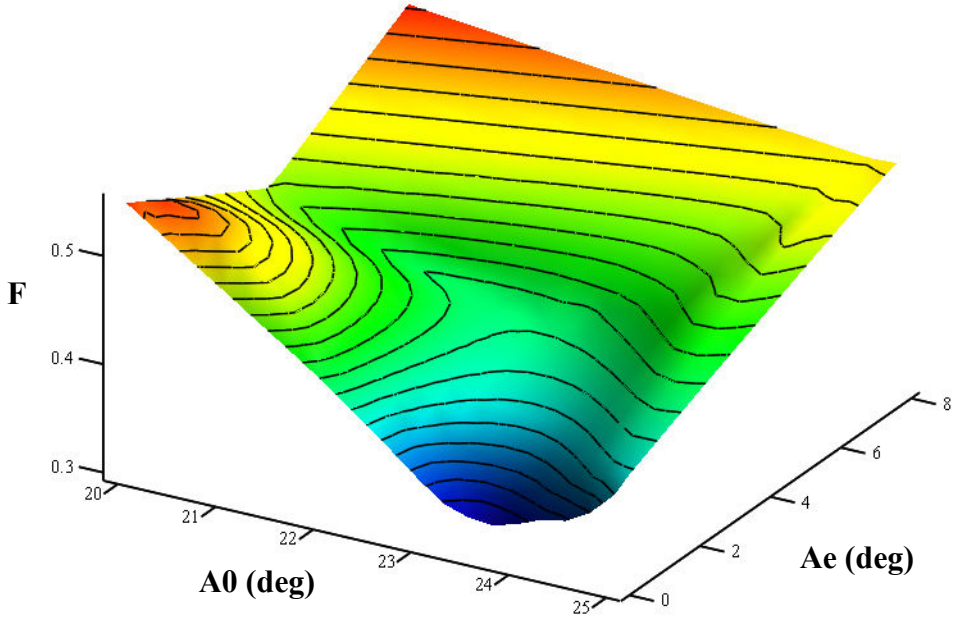

Figure 4.3: Minimum from extending the exit angle to 0 degrees.

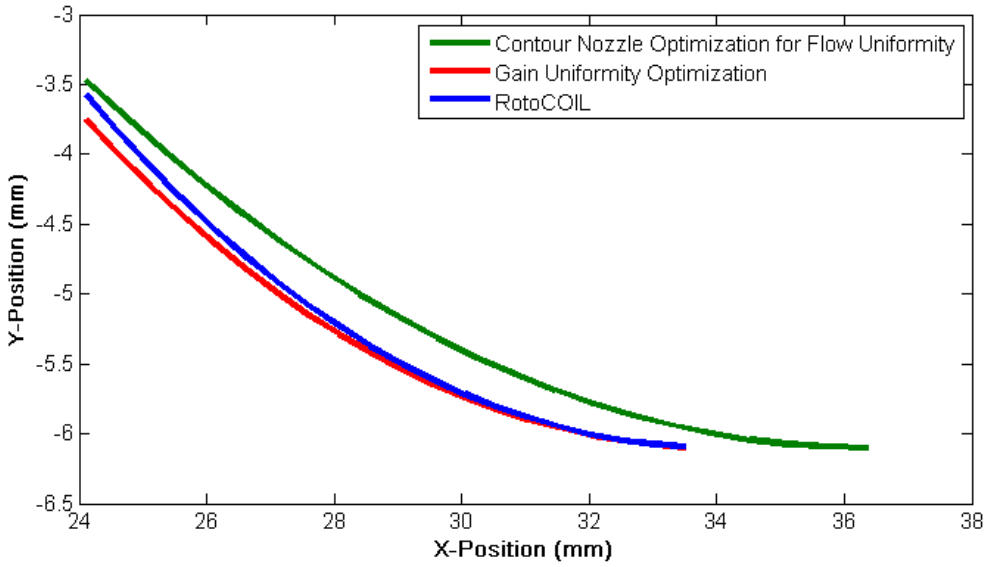

Figure 4.4: Comparison of the baseline contour (RotoCOIL) with the gain uniformity and flow uniformity optimized contours.

To further show the improved flow uniformity, Figure 4.5 shows the y component velocity profiles of several nozzles that were modeled over the course of these projects. Remembering the start of the mixing nozzle simulations, the RotoCOIL was the baseline and has the worst flow uniformity. The optimization of gain uniformity did improve the flow uniformity, but was limited since the distance from the throat to the nozzle exit was fixed. With the contour optimization of the contour with the extended length, there is a nearly perfect flow uniformity (i.e. y velocities go towards zero) outside of the boundary layers.

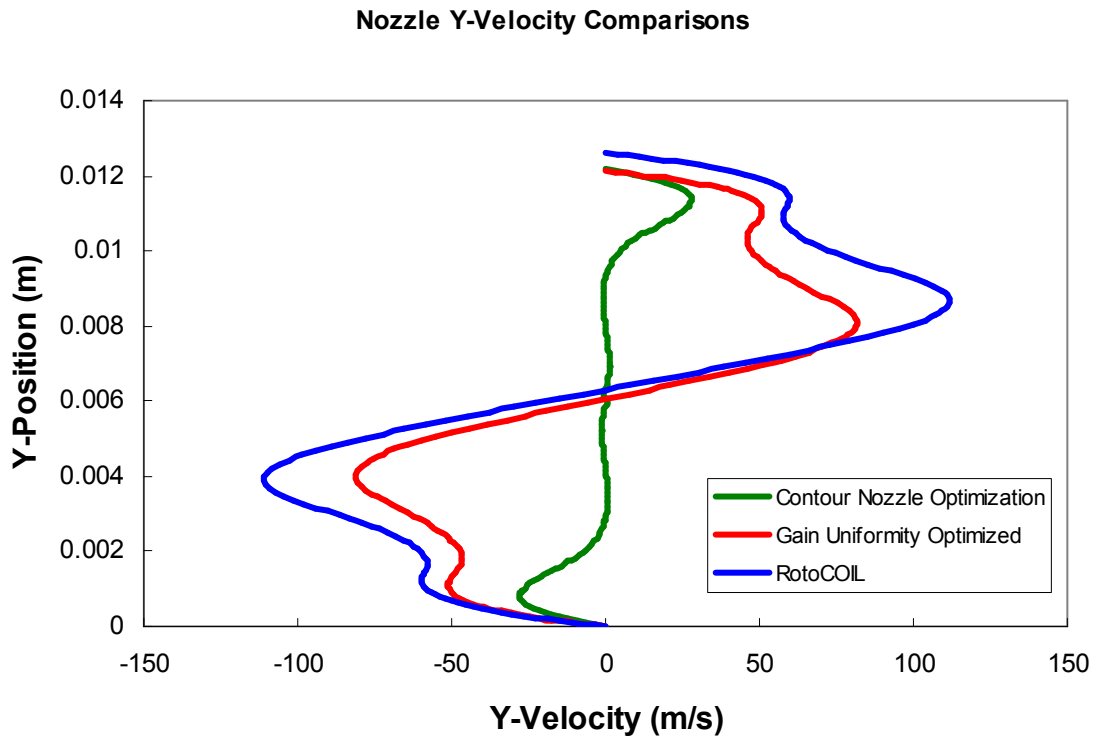

Figure 4.5: Y component velocity profiles showing the improvement of the Optimized Contour nozzle.

Furthermore, it was of interest to explore changing the nozzle outlet location, Xe, to see if extending the length from the throat to the exit would greatly improve results. A parametric study was carried out for this analysis to get an overall picture of the design space. The same conditions were carried out as in Table 4.1 with the exception of ranging Xe from 34 to 40 mm. Each variable was incremented by one unit within the range.

Now that there are three variables it is difficult to present all the data on one plot. Therefore, the Xe variable will be constant in the different plots and the two angles with the objective function will be the three dimensions.

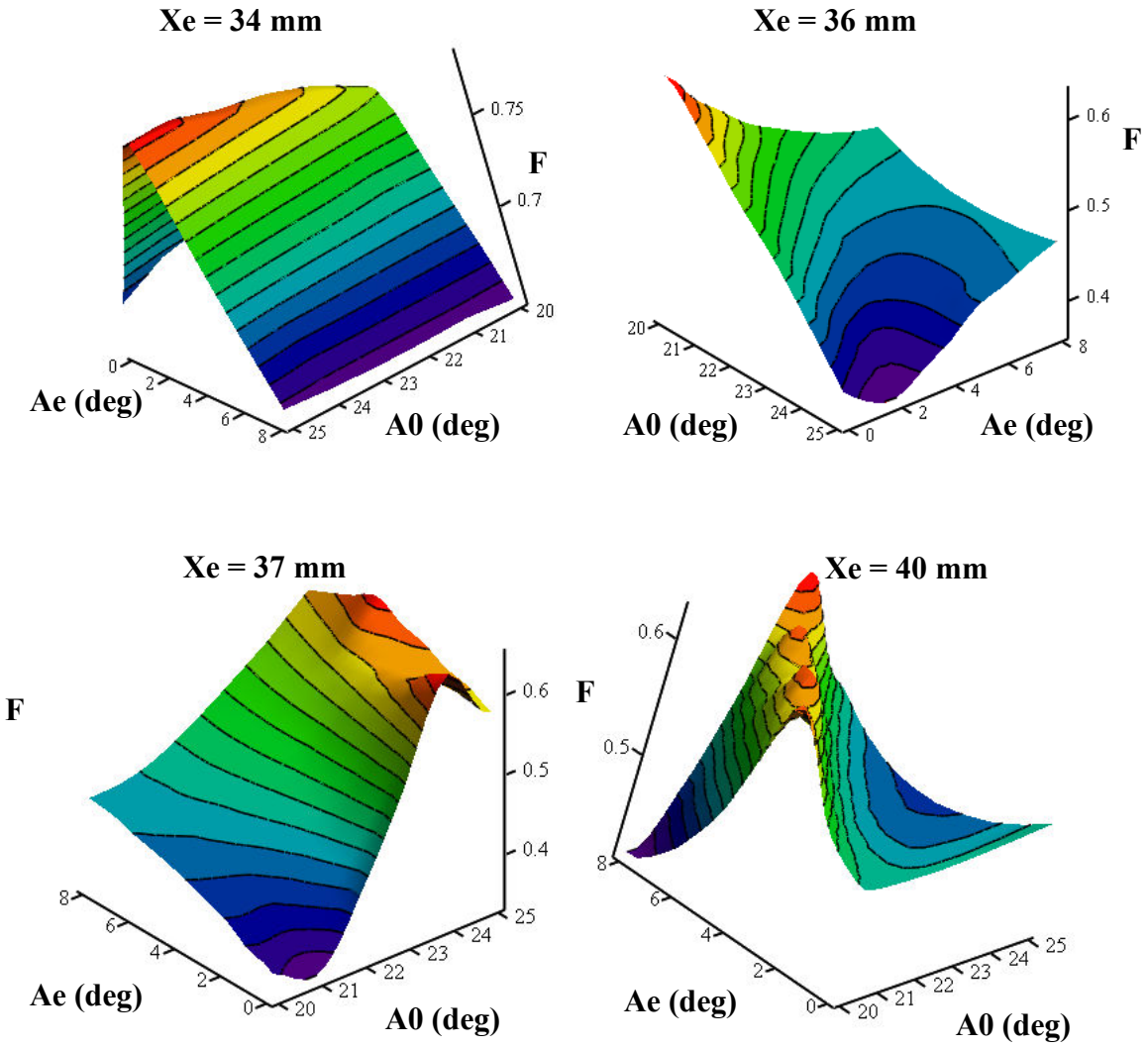

Figure 4.6: Results from the parametric study showing the performance at different nozzle lengths.

Figure 4.6 may be hard to decipher but upon a closer look the information becomes clear. For the exit location of Xe equal to 34 degrees, the objective function results are very high (F > 0.65) meaning that the flow uniformity is poor. The Xe value is basically the RotoCOIL design and similarly in Figure 4.5 does not perform well. When Xe is equal to 36 and 37 mm, there are much improved results (min F = ~0.35). Above 37 mm the performance worsened. However for the best performing Xe values, there is a shift in the

A0 value from 25 to 20 degrees for 36 and 37 mm, respectively. Presumably this shows that there is an optimum A0 between 36 and 37 mm. For 36.36mm it was found the A0 optimum to be 23.46 degrees. However, upon plotting the optimized contour at 36.36 mm with the best results from Xe values of 36 and 37 mm (see Figure 4.7), it can quickly be seen that the contours are virtually the same. The changing angle values are accommodating the same contour shape. Therefore, it appears that there is a threshold for the minimum nozzle length and once the nozzle is beyond that threshold the flow uniformity does not get any better. This threshold for this case appears to be 36 mm (34 and 35 mm had a poor performance) or ~12 mm from the starting tangent point to the nozzle exit.

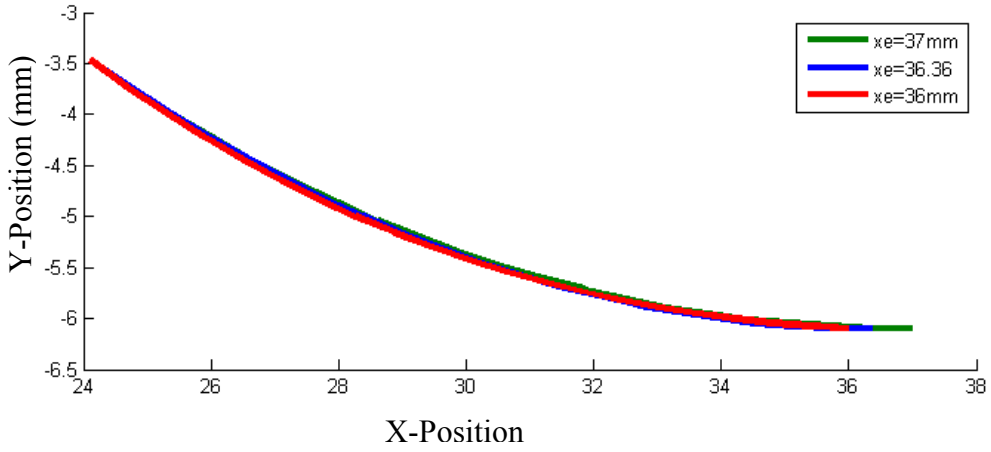

Figure 4.7: Comparison of the optimized nozzle at Xe = 36.36mm with the min F results from Xe = 36 and 37mm.

Conclusions

The Chapter Three optimization improved upon the gain uniformity, but the contour was improved in Chapter Four to give a better flow uniformity. As seen in Figure 4.5, the flow uniformity of the optimized contour is significantly better that the hot flow optimization. Additionally, it was discovered that the length expansion curvature has to reach a minimum before the flow uniformity plateaus.

For completeness, the optimized contour nozzle was simulated in 3D under hot flow conditions and the gain uniformity was compared to the baseline and hot flow optimized nozzle. Figure 4.8 shows that the contour optimization nozzle still has a good gain uniformity profile.

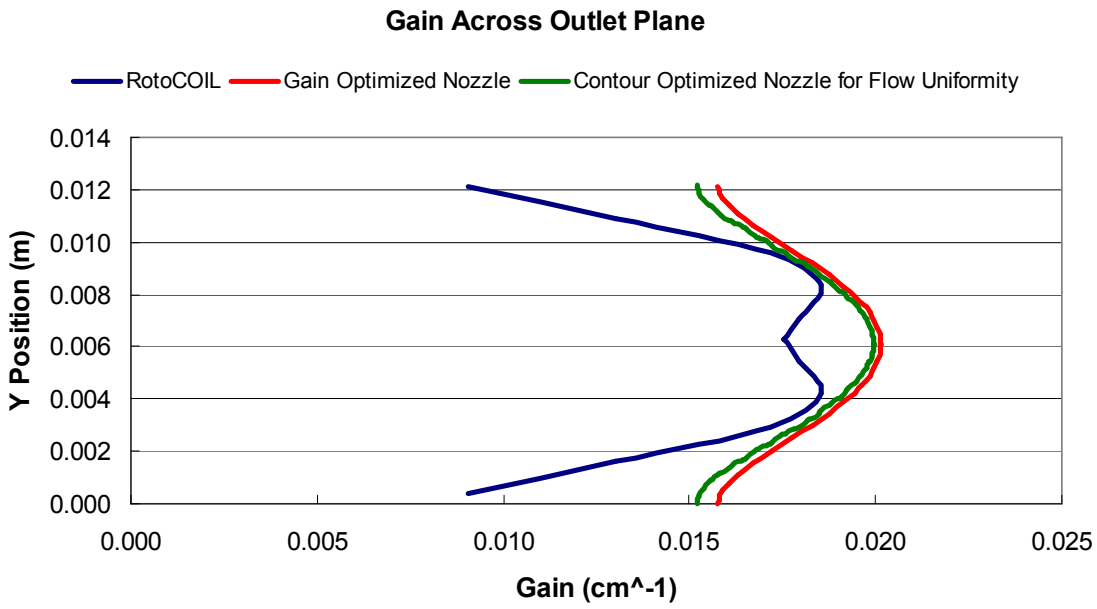

Figure 4.8: Gain profiles at the across the outlet plane.

CHAPTER 5

SUPERSONIC EJECTOR: PROFILING

The low cavity operating pressure (10 torr) of the COIL requires a pumping system to exhaust the gases to the local exit pressure. In the ABL, several steam ejectors are used to recover the lasing cavity pressure to atmospheric conditions and exhaust the gases at the operational altitude of 40,000 ft. The ejector is powered by high temperature, high pressure steam which entrains the gases and raises the overall pressure to the desired level at the exit of the diffuser. To achieve functional performance, the ABL carries approximately 17 tons of this motive fluid. A typical ejector cross section is shown in Figure 5.2. Following convention, the ejector properties are denoted as the primary flow and the laser gases are the secondary flow. There are several main elements to an ejector; the supersonic motive nozzle, suction chamber, mixing channel, and diffuser.

Recent research has shown that significant enhancements in ejector performance can be achieved by optimizing each of these elements. Guillaume [52] has proposed the use of elliptical nozzles to enhance entrainment and Eames [33] has shown that profiling the discharge section can result in significantly improved pressure recovery.

Improvement in efficiencies for the ABL can be made by profiling the mixing channel and diffuser of the ejector. In a traditional constant pressure ejector (see Figure 5.2), a converging section maintains a constant pressure as the primary flow entrains the secondary. Once the flow enters the mixing channel, there is a section of constant pressure mixing before the mixed fluids undergo a shock. Finally, the flow enters the diffuser which increases the static pressure at the expense of reducing the momentum.

With the presence of shocks in the mixing channel, losses to the total pressure results in a reduction on the pressure recovery ratio.

In order to evaluate the performance of a profiled ejector, a traditional constant pressure ejector will also be calculated. Using the same boundary conditions, 1D models will generate geometries for both a profiled [33] and constant pressure ejector [20]. The generated geometries will be evaluated in 2D axi-symmetric simulation to determine the performance and validation of the 1D modeling. Additionally, the 2D simulations will be compared to published experimental data to ensure the accuracy of the numerical method.

To quantify improvement of an ejector, several constraints must be fixed. For the application of the ABL, the flow rate of the laser gas media is fixed, which translates to the secondary flow for the ejector. Rather than redesigning the motive nozzle's throat dimension (changing the flow rate through the nozzle since it is choked), the motive flow rate will also be fixed and therefore, the entrainment ratio will remain constant throughout the analysis. The pressure recovery will be the quantified performance. The entrainment ratio directly translates to pressure recovery and is reported in literature for refrigeration applications [24, 26, 27, 31, 32, 36, 53]. A typical ejector performance plot and operation is shown in Figure 5.1.

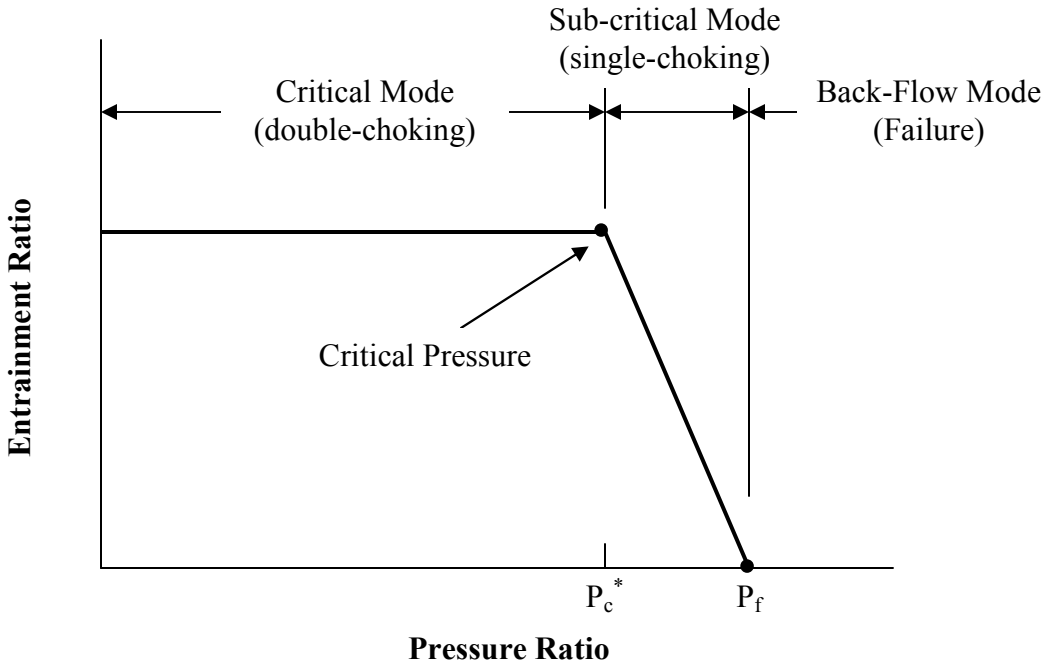

Figure 5.1: Typical operational modes of an ejector.

Constant Pressure Method

In a classic constant pressure ejector, Figure 5.2, there is a converging section as the driver fluid mixes with the secondary flow, a straight section (throat) and finally a diverging section which slows the flow down and increases the static pressure. The first objective is to develop a 1D calculations which will provide baseline geometry of a conventional ejector. From previous researchers it is known that a constant pressure ejector performs better than a constant velocity ejector [20]. For this reason it was chosen to develop a 1D model analyzing the constant pressure ejector. Huang et al. [20] developed a constant pressure model building off the original model by Keenan et al. [21]. The Huang et al. model includes choking of the entrained flow at critical mode operation. The assumptions made in the 1D constant pressure model are as follows [20]:

1. The working fluid is assumed to be ideal with constant C_p and γ.
2. Flow is 1D and at steady state.
3. The kinetic energy at the inlets and exit are negligible.
4. Isentropic relations are used as an approximation. To account for frictional and mixing losses in a non-ideal process, coefficients are introduced into the equations. The values are determined experimentally.
5. Mixing occurs within the constant area section.
6. Mixing occurs at a uniform pressure.
7. The entrained flow is choked at a hypothetical throat.
8. The wall of the ejector is adiabatic.

For this analysis, the primary fluid stagnation pressure and temperature are needed for the primary nozzle (see Figure 5.2). Given that the flow is choked at the throat of the primary nozzle, the mass flow can be calculated as:

$$\dot{m}_p = \frac{P_g A_t}{\sqrt{T_g}} * \sqrt{\frac{\gamma}{R}\left(\frac{2}{\gamma+1}\right)^{(\gamma+1)/(\gamma-1)}} \sqrt{\eta_p} \tag{21}$$

where η_p is the isentropic efficiency of the compressible flow nozzle. Knowing the exit area of the primary nozzle and using isentropic relationships the exit Mach and pressure can be calculated. Similarly assuming constant pressure from the secondary flow to the point of entrainment, the Mach and primary flow area of the constant area mixing channel can be calculated. The application of assumption 6 from above and the realization that the Mach at the choke point equals unity, the pressure at the sonic condition and mass flow rate can be determined. Adding the areas from the primary and secondary flows, the mixing channel area, A_3, can be found. Lastly, using energy and

momentum balances, the remaining velocities, pressures, and temperatures at the exit can be calculated. A more detailed description with a flow chart is presented in Appendix A. This 1D model was carried out in Matlab.

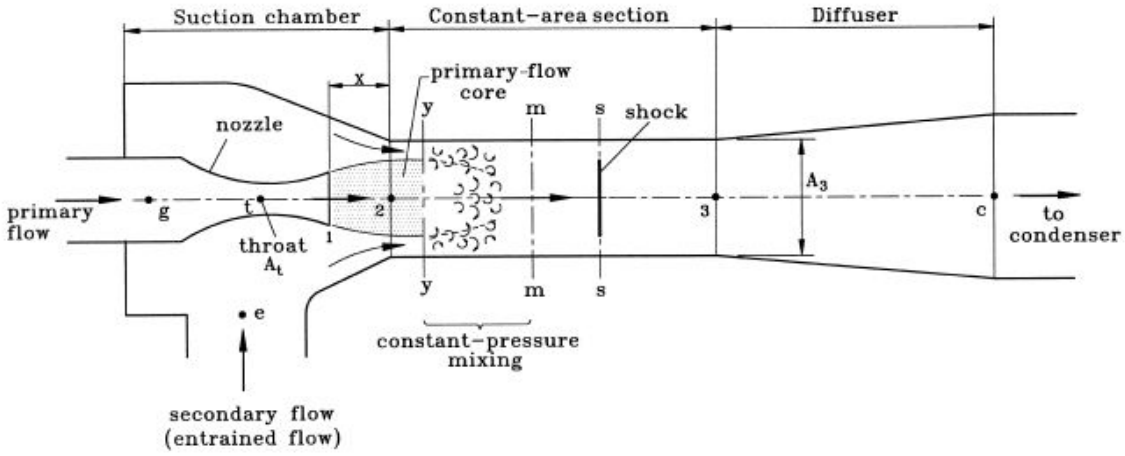

Figure 5.2: A conventional constant pressure ejector [20].

Constant Rate of Momentum Change Method

Alternatively, Eames proposed a methodology to design the ejector by profiling the mixing channel and diffuser such that the momentum of the flow changes at a constant rate. The Constant Rate of Momentum Change (CRMC) method calculates the ejector geometry based on a set of input pressures and velocities [33]. It assumes a constant momentum rate of the flow, which allows the static pressure to gradually rise from the entrance to the exit of the ejector. This avoids the total pressure loss due to the shock process. Theoretical predictions for a profile generated using such a technique have improved the pressure recovery by values up to 50% compared to conventional ejectors [33]. Figure 5.3 shows a schematic diagram of a CRMC ejector.

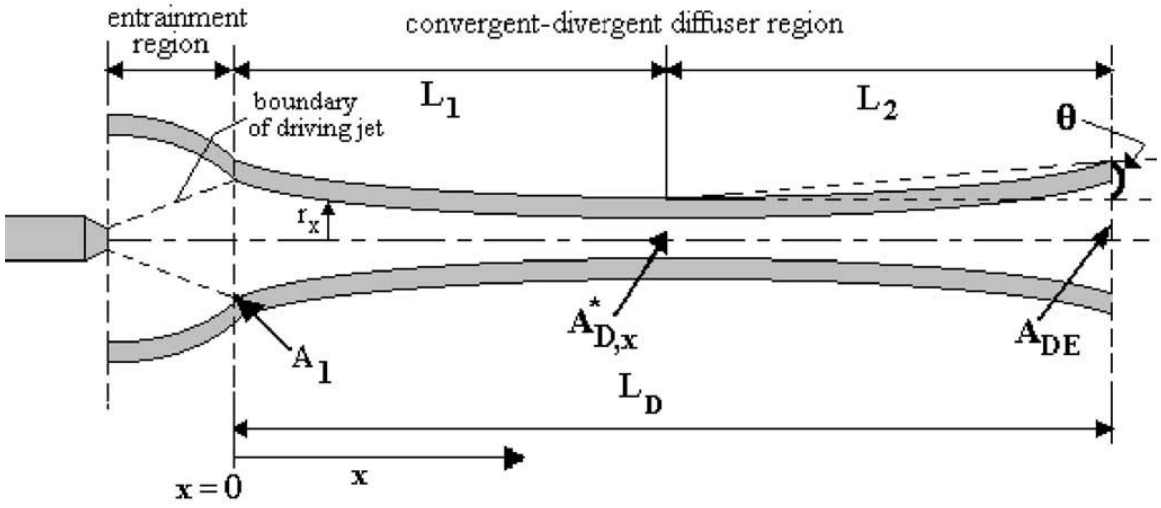

Figure 5.3: Geometry of a CRMC ejector [33].

The CRMC model contains the following assumptions in order to simplify the geometry and flow passage:

1. The same gas is assumed for both primary and secondary flows.
2. The process is assumed to be ideal.
3. The primary mass flow and entrainment ratio are specified.
4. The total pressure and temperatures of the primary and secondary flows are known.
5. The flow is assumed adiabatic.
6. The velocity of the secondary flow is specified.

The entrainment process is carried out at constant static pressure. Under the ideal design conditions the combined primary and secondary flow is compressed in the diffuser section so that at its throat the local Mach number equals unity. The main CRMC assumption can also be states as:

$$\frac{d\dot{M}_o}{dx} = \dot{m}_g(1+R_m)\frac{du}{dx} = \beta \tag{22}$$

where β is a constant. Using these conditions and taking the boundary conditions:

$$u(x) = u_{primary} \quad \text{at} \quad x = 0 \qquad \text{and} \qquad u(x) = u_{out} \quad \text{at} \quad x = L_E$$

Equation 22 reduces to:

$$u(x) = u_{primary} - \frac{(u_{primary} - u_{out})x}{L_E} \qquad \text{for} \quad 0 \le x \le L_E \tag{23}$$

Numerical Methods

To compare the performance of the ejector geometries, 2-D axisymetric CFD simulations were completed for identical conditions. Eames provided results for his geometry therefore, the corresponding conditions were used for the comparison [33]. The operating conditions are given in Table 5.1 while a comparison of the resulting geometries is shown in Figure 5.4.

Table 5.1: Constraints for the analysis of the ejector.

Known Conditions	
Primary Pressure	0.1985 MPa
Primary Temperature	393.15 K
Primary Flow Rate	1 gm/s
Secondary Pressure	872 Pa
Secondary Temperature	278 K
Secondary Flow Rate	0.42 gm/s
Entrainment Ratio	0.42
Specific Heat Ratio	1.3
Primary and Secondary Fluid	steam

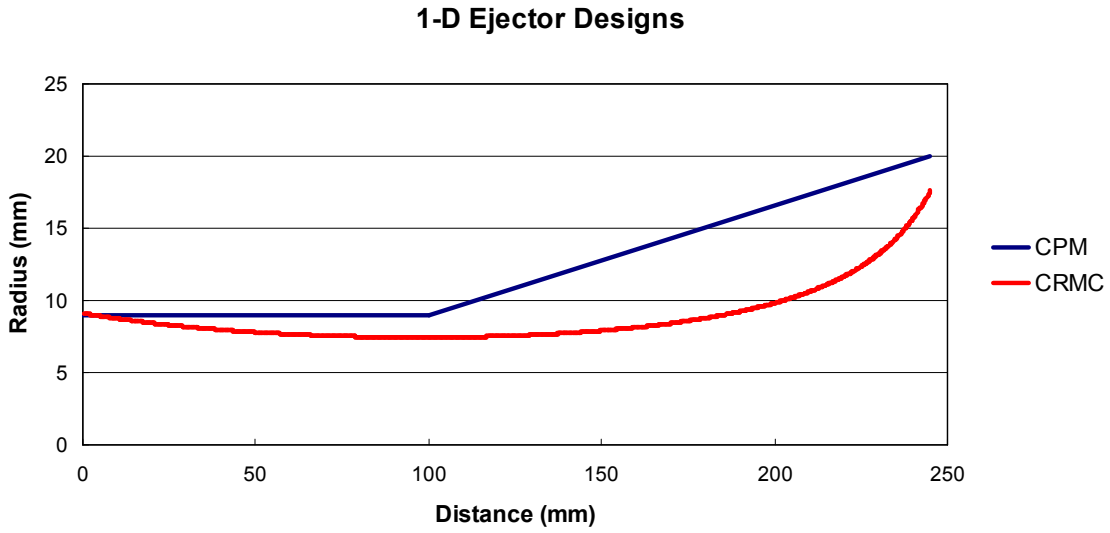

Figure 5.4: CRMC calculated ejector geometry compared to CPM geometry for the same conditions.

The ejectors modeled were axi-symmetric with a *k-ε* turbulence model. A pressure-velocity coupled solver was used to calculate the flow field along with a 2nd order discretization. A pressure boundary condition was used for both the primary inlet and the outlet, whereas, a mass flow inlet was used for the secondary (suction) inlet The wall boundaries were modeled with no slip conditions. Furthermore, an adaptive meshing technique was used based on the gradient of the Mach number. This allowed for refinement along the stratification of flows.

Table 5.2: Dimensions of the CPM ejector [33].

Entrainment Region	140mm	Outlet Diameter	40mm
Throat	40mm	Throat Diameter	18mm
Subsonic Diffuser	210mm	Mixing Chamber Inlet Diameter	24mm

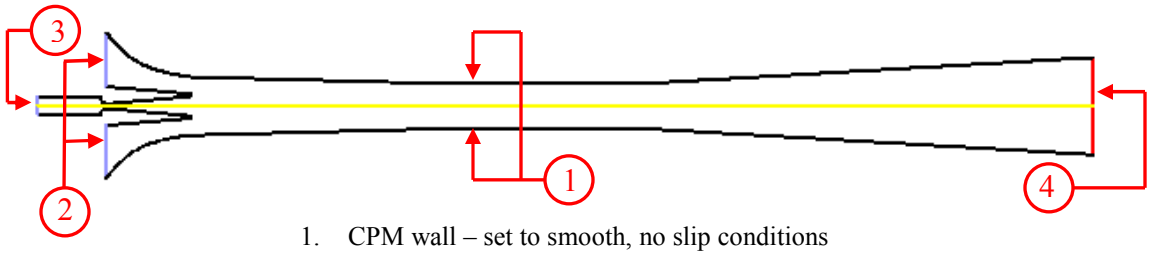

1. CPM wall – set to smooth, no slip conditions
2. Suction Inlet – set to pressure inlet
3. Motive Inlet – set to pressure inlet
4. Outlet – set to pressure outlet

Figure 5.5: CFD model of the constant pressure channel calculated from the CPM [20] model.

The profiled geometry replaced the constant area throat for the center injection ejector. Table 5.3 and Table 5.1 provide the CRMC dimensions and the boundary conditions, respectively.

Table 5.3: CRMC Ejector dimensions.

Entrainment Region	140 mm	Outlet Diameter	32 mm
		Throat Diameter	14 mm
Subsonic Diffuser	250 mm	Mixing Chamber Inlet Diameter	24 mm

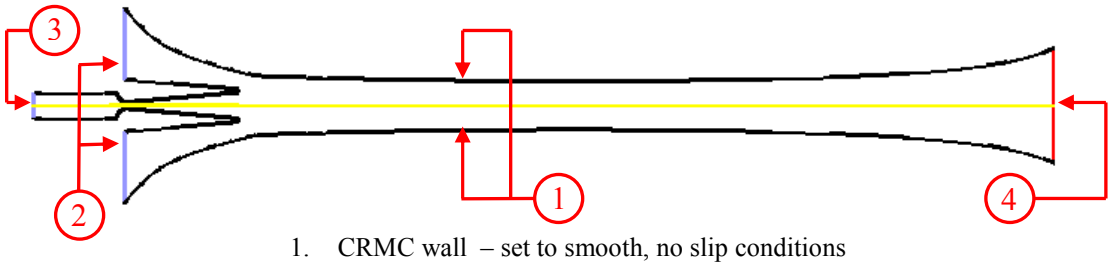

1. CRMC wall – set to smooth, no slip conditions
2. Suction Inlet – set to pressure inlet
3. Motive Inlet – set to pressure inlet
4. Outlet – set to pressure outlet

Figure 5.6: CFD model of the profiled geometry calculated from the Eames [33] CRMC model.

Results

The first step was to validate the algorithms and boundary conditions utilized. Sriveerakul et al. [30] published experimental data of a supersonic ejector with similar dimensions and conditions. The pressure recovery results of the CFD calculation for the constant pressure ejector are shown in Figure 5.7, with the published results from Sriveerakul et al. [30]. The CFD calculation matched published data well.

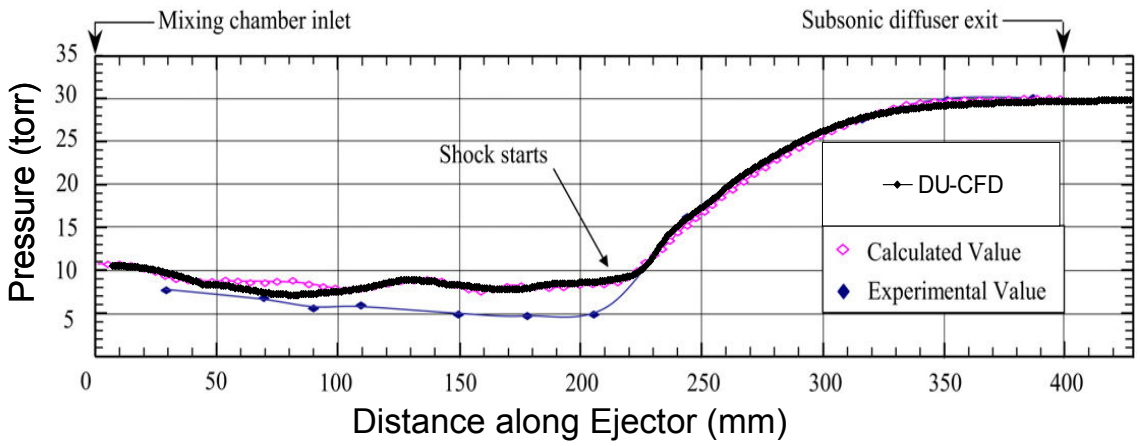

Figure 5.7: Constant pressure ejector pressure profile: Calculated and measured from Sriveerakul et al. [30] compared to the presented work.

Confident that the CFD calculations are producing realistic results, a comparison of performance from the CPM and CRMC profiles could be completed. Figure 5.8 shows the entrainment ratio compared to the pressure recovery. The initial assumption of a 0.42 entrainment ratio from the CRMC [33] is an overestimate for the conditions and the calculated value is approximately 0.20. The CPM [20] model more accurately calculates the entrainment. Adjusting the coefficients for greater losses, the model converges on the CFD values. The other noticeable difference is that the CRMC geometry has an increased pressure recovery compared to the CPM ejector for a given entrainment ratio. The critical pressure recovery for the CPM and the CRMC ejector occur at 3.7 and 5.8, respectively. However, when the pressure ratio for the CRMC is held to be equal to the CPM pressure ratio, then the entrainment ratio for the CRMC is increased by 48% compared to the CPM.

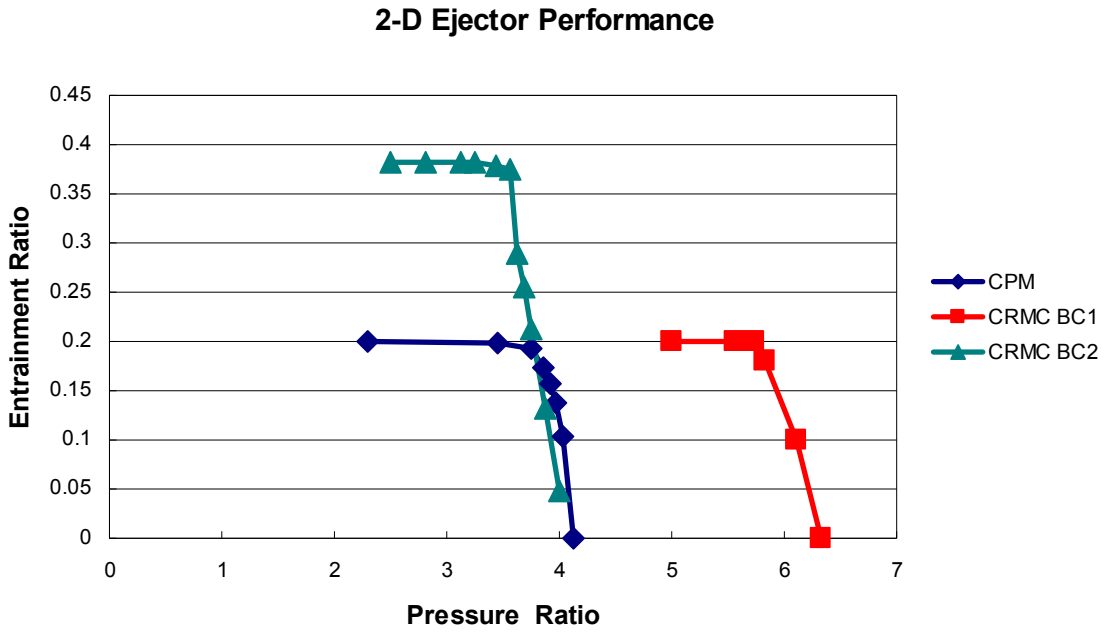

Figure 5.8: Comparison of the CPM ejector performance to the CRMC ejector for 2 different boundary conditions: 1) equal entrainment ratios and 2) equal pressure ratios.

Conclusions

The significant findings from this supersonic ejector comparison study of nozzle performance using 2-D axisymetric simulations is the CRMC profiled geometry, developed by Eames [33], improved the critical pressure ratio from 3.8 for the CPM to 5.8. However, the CRMC 1D calculation does not calculate the entrainment ratio; rather it is an initial input and greatly affects the results. The CPM calculation, therefore, can be used to calculate the entrainment ratio for the design point and its results can be used for a more accurate solution of the CRMC model.

The pressure recovery and entrainment ratio are direct trade offs. For the case of the ABL, the pressure recovery needed is based on the atmospheric conditions and the goal is to reduce the primary flow rates. If the CRMC channel was implemented, the primary nozzle could be redesigned to reduce the flow rate (smaller throat), while maintaining the same Mach speeds for momentum transfer and entrainment. Therefore, the CRMC channel should be able to achieve the required pressure recovery, while requiring less primary flow compared to conventional ejector channel design. Theoretically, the 17 tones of primary fluid used for the ABL could be reduced by 48%.

CHAPTER 6

SUPERSONIC EJECTOR: LOBED MOTIVE NOZZLE

As stated in Chapter Five, the ABL carries 17 tons of fluid to generate the steam needed by the supersonic ejectors to recover enough pressure to exhaust to local atmospheric conditions at 40,000 feet (150 torr). Furthermore, profiling the ejector through the CRMC method improves the pressure recovery over the CPM ejector.

Other researchers [36, 52, 54] have proposed different nozzle geometries to promote flow instabilities to enhance the entrainment of the secondary flow. Previous work from Chapter Two on the I_2 mixing nozzle demonstrated the benefit of using elliptical nozzles to increase mixing. Furthermore, Hui et al. reports that lobed nozzles have great differences in turbulent structures and vortex scales compared to circular nozzles, which enhance mixing [55]. These elliptical or lobed structures emanating from a central point create the shedding of vortices from the nozzle tip due to Kelvin-Helmholtz instabilities. However, as one increases the surface area of interaction the internal frictional losses in the nozzle prior to injection will hinder performance (i.e. average mach numbers will drop as a result of frictional loses). If one can imagine a circular exit to a nozzle and adding lobes to create vortices for mixing, then continue to add more and more; eventually, the exit returns to a circular shape (see Figure 6.4). Therefore, the hypothesis is that there has to be an optimum number of lobes, or perimeter of shear layer, resulting in the maximum amount of mixing of the entrained flow. Thus the objective of this effort is to explore the effects of the number of lobes, perimeter of the shear layer, and exit area of the nozzle on the pressure recovery. The resulting work will show the improvement of pressure recovery compared to a conventional circular nozzle. Additionally, validation of the 3D simulations will be presented.

Experimental Methods

In order to validate the ejector model, an industrial collaborator assisted in developing a small scale test stand for a center injection ejector. Nitrogen was used for both the motive and suction gases. The motive gas was pressurized to approximately 30 psi, while the suction inlet flow rate was limited to 60 SLM and the pressure was measured. The outlet was pulled by vacuum. A conceptual drawing is shown in Figure 6.1. The test unit is made sectional so that several designs can be tested. Stereo lithography rapid prototyping was used to fabricate the ejector components, to allow quick turn around of the different parts.

There were two different nozzles and two different mixing channels fabricated. A typical round nozzle was compared to the lobed nozzle created in the 3D CFD models. For the mixing channels, a CPM channel with a diameter of 19 mm was compared to the CRMC profiled mixing channel [33].

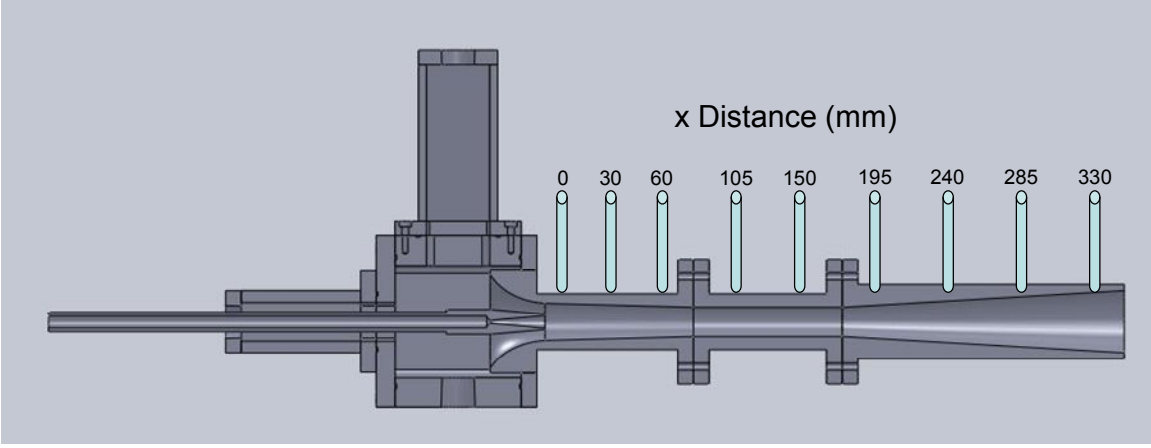

Figure 6.1: Small scale ejector test set up.

Numerical Methods

The lobed nozzle was modeled for both mixing channels (see Figure 6.2). The same conditions and methods were used as presented in Chapter Four. Several different lobed geometries were designed and are discussed below.

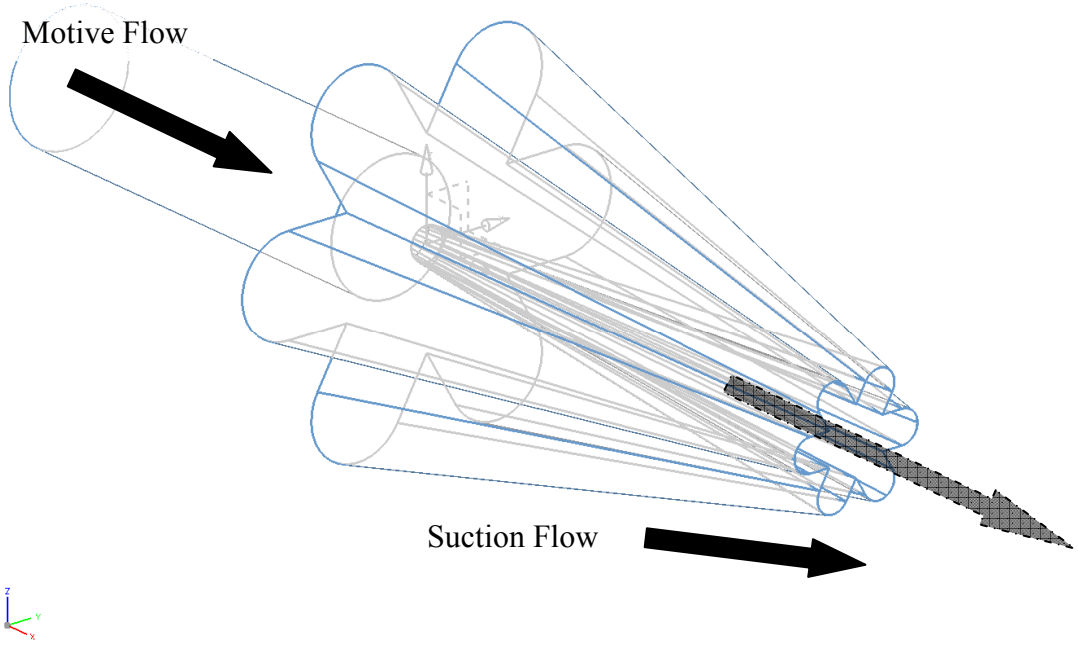

Figure 6.2: Design concept for motive gas lobed nozzle in order to promote mixing.

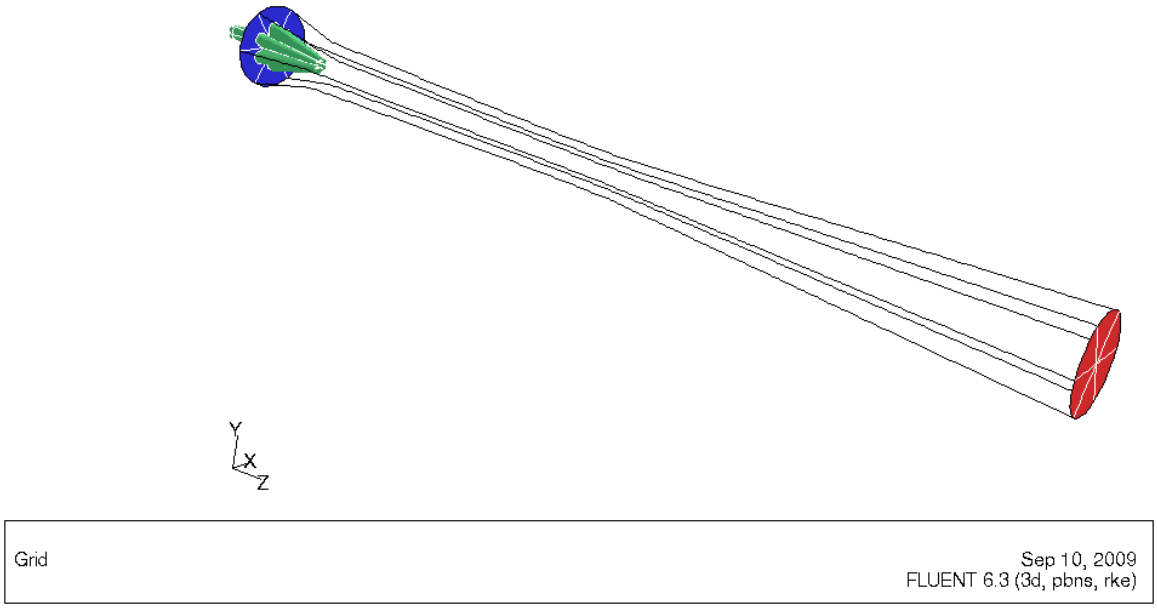

Figure 6.3: Schematic of lobed nozzle design modeled for CFD.

Constant Expansion Angle

A series of lobed nozzles were designed to replicate the major diameter of the round nozzle at 8 mm. This provided the same expansion angle from the throat to the tip. Obviously, the exit areas differed from each nozzle and therefore the exit Mach numbers also differed. Figure 6.4 shows the exit of the nozzles superimposed.

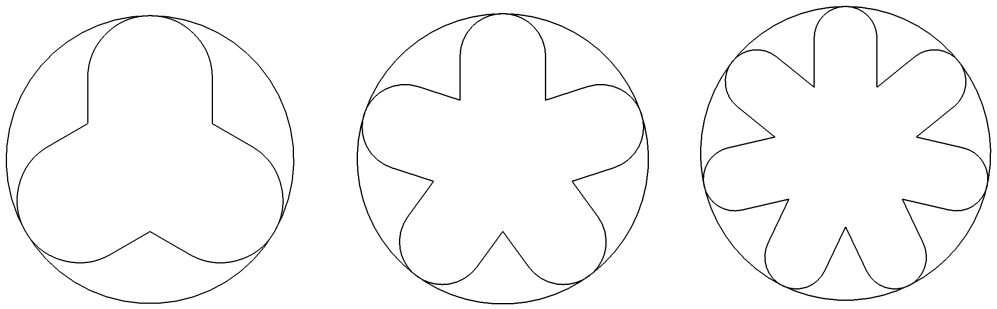

Figure 6.4: Schematic showing the different nozzle exit areas for a circular and 3, 5, and 7 lobed designs.

Constant Exit Area

Another series of lobed nozzles were designed such that the exit nozzle area remained equal to the round nozzle, resulting in similar Mach numbers at the exit of nozzle. Figure 6.5 shows the nozzle designs.

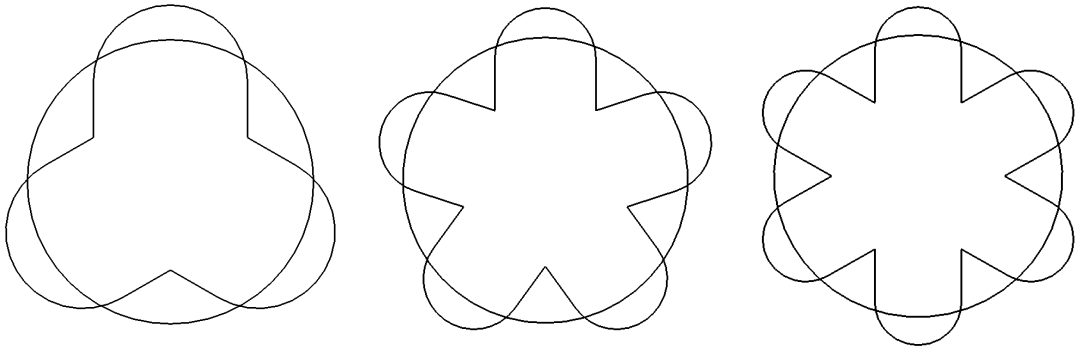

Figure 6.5: Schematic showing the nozzle exit areas being equal for a circular and 3, 5, and 6 lobed designs.

Results

Experimental

The experimental and CFD results for the round nozzle with constant area throat are presented in Figure 6.6. The results from CFD calculations and experimental measurements are consistent. Important values to be pointed out are the entrainment ratio and the total flow rate, 0.26 and 1.96E-03 kg/s for the non-heated case (293K) respectively and 0.34 and 1.99E-03 kg/s for the heated case (310K) respectively.

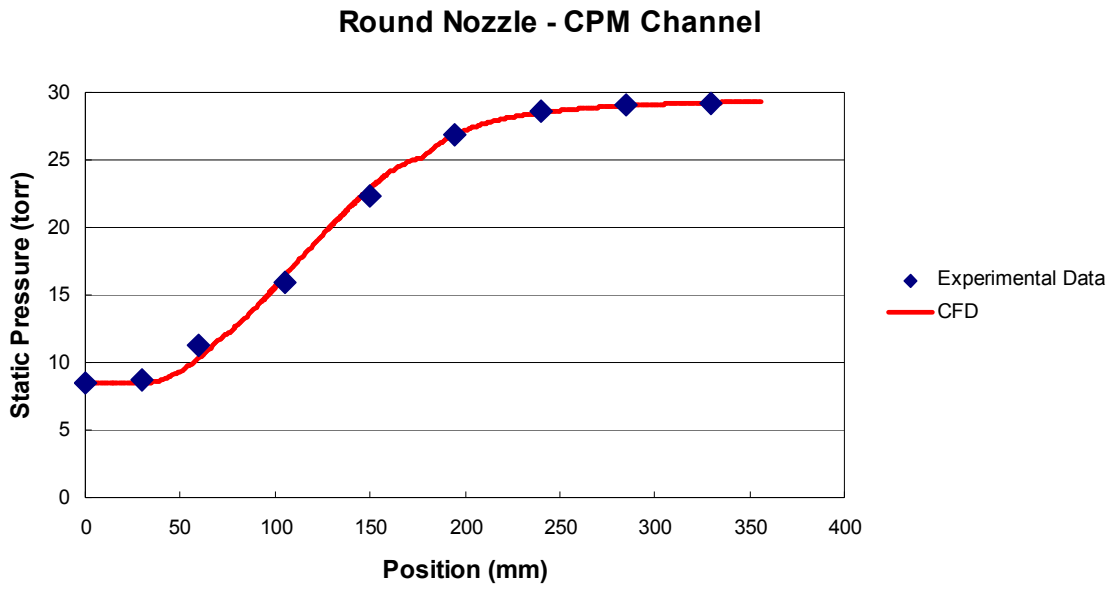

Figure 6.6: Ejector experimental results compared to the CFD calculations for the round nozzle and constant area throat.

The results for a 6 lobed nozzle with constant area throat are presented in Figure 6.7. The CFD calculation matches the experimental results very well. Important values to be pointed out are the entrainment ratio and the total flow rate, 0.10 and 1.37E-03 kg/s for

the non-heated case (293K) respectively and 0.18 and 1.33E-03 kg/s for the heated case (310K) respectively.

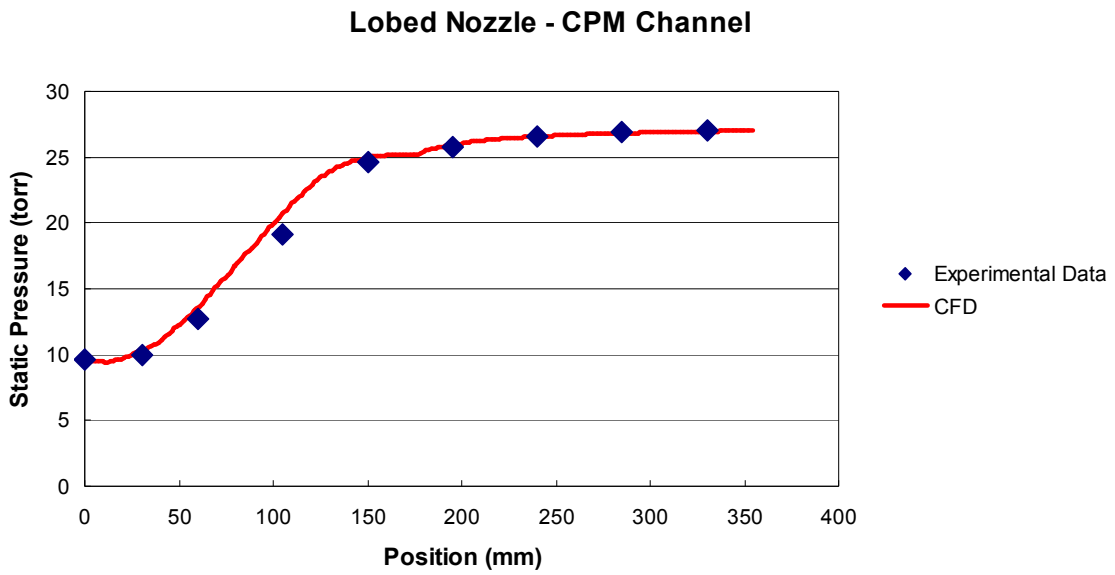

Figure 6.7: Ejector experimental results compared to the CFD calculations for a 6 lobed nozzle and constant area throat.

Constant Expansion Angle

The first set of results compared the round motive nozzle to different lobed nozzles. The lobed nozzles all have the same diverging angle as the round nozzle leading to the same major diameter of 8 mm. Figure 6.8 shows all of the lobed nozzles enhance the mixing and result in an increased pressure recovery. The addition of more lobes initially keeps increasing the pressure recovery, but at four lobes the trend reverses (see Figure 6.9). This alludes to the hypothesis of there being an optimum may be correct. However, the comparison is flawed since more than one variable is changing. All of the nozzles have a different exit area due to the major diameters being held constant. Therefore, the exit Mach numbers are also changing. Additionally, the perimeter values are changing as a

result of increasing the number of lobes. Figure 6.9 shows that as both the perimeter and areas increase towards four lobes, the pressure recovery increases. Thus it is unclear if the enhanced performance is from the perimeter or increased Mach number due to the increase in exit areas.

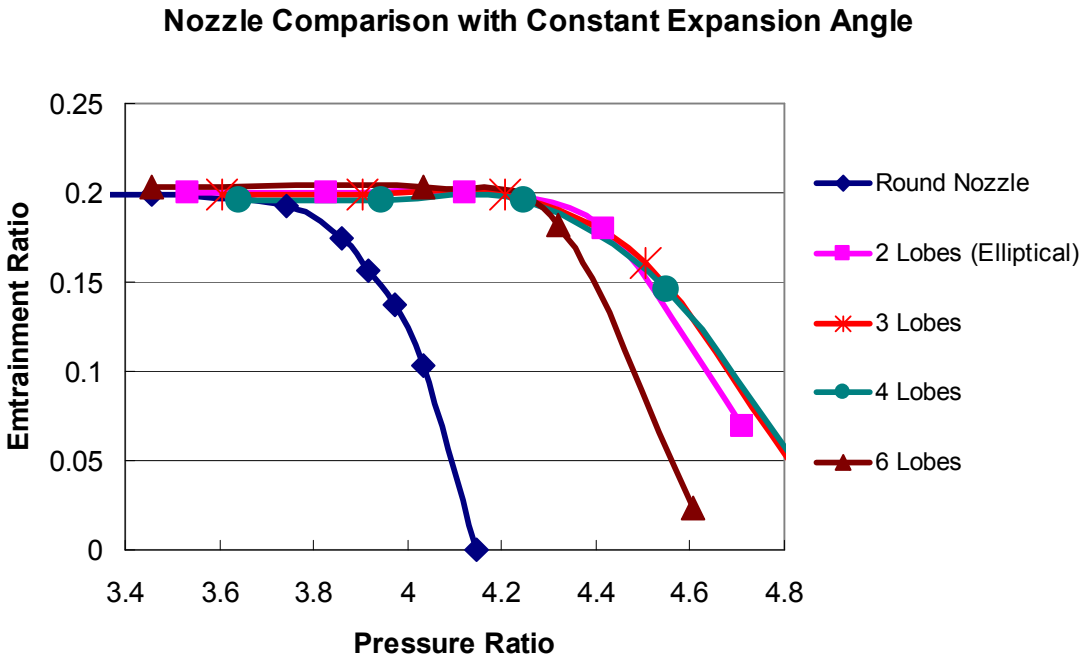

Figure 6.8: Plot of the performance of the different nozzles investigated. The identified data points are the critical pressure recovery value for each nozzle.

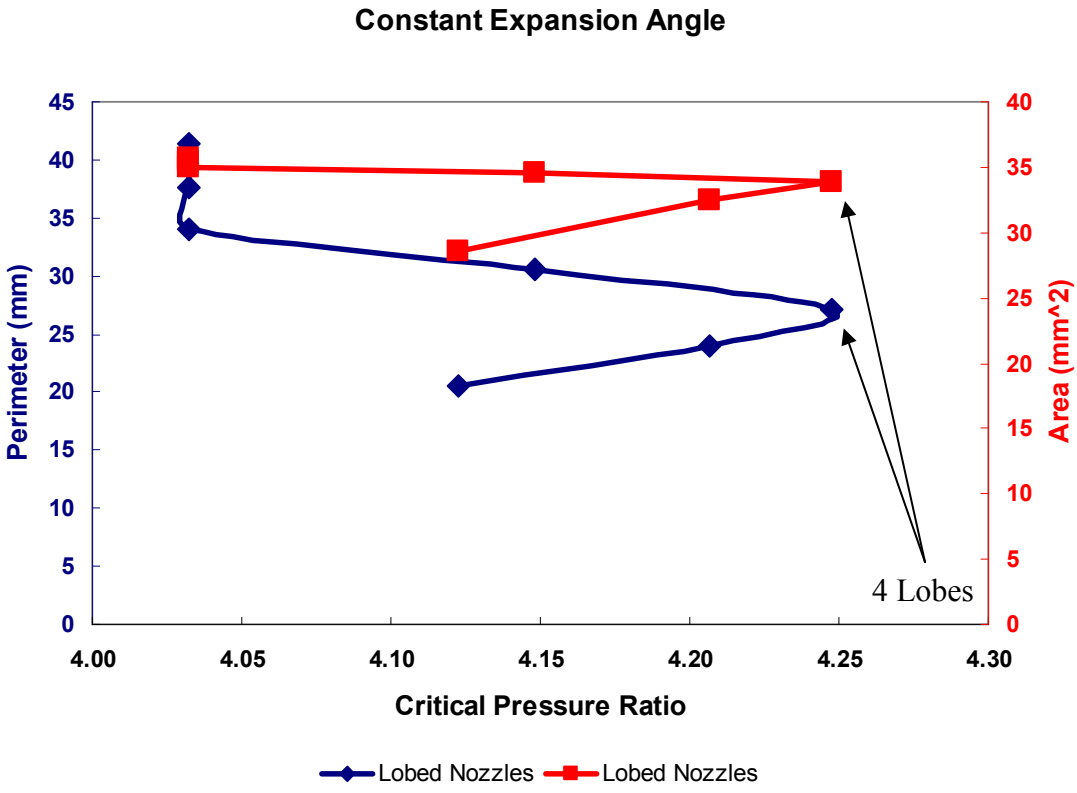

Figure 6.9: Plot showing that the increase in perimeter and area to the 4 lobed design increases the critical pressure ratio.

Constant Nozzle Exit Area

When holding the nozzle exit areas constant, the pressure recovery ratio shows similar results to the previous lobed nozzles. Figure 6.10 clearly shows there is an optimum perimeter value that would result in a maximum pressure recovery. Since the Mach number remained constant, Figure 6.10 confirms that the pressure recovery is a function of the perimeter for the lobed nozzles. Figure 6.11 shows the pressure recovery performance of the lobed nozzles compared to the round nozzle. The maximum recovery

occurs at three lobes instead of four as was found for the constant expansion angle nozzle designs.

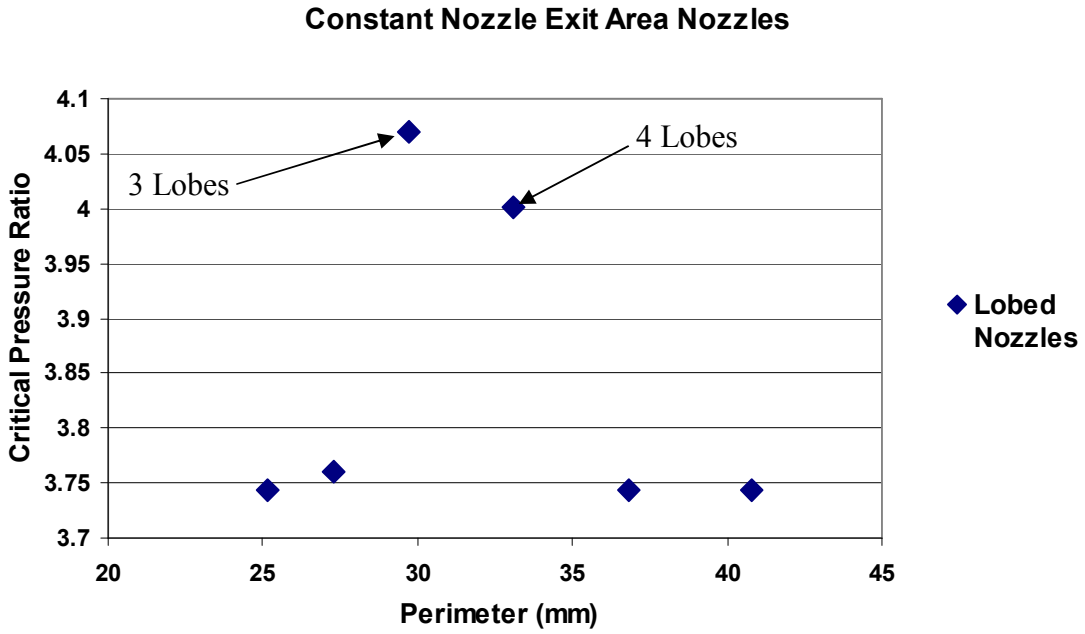

Figure 6.10: Plot showing the when the nozzle exit area is held constant there is an optimum perimeter value for a maximum pressure recovery.

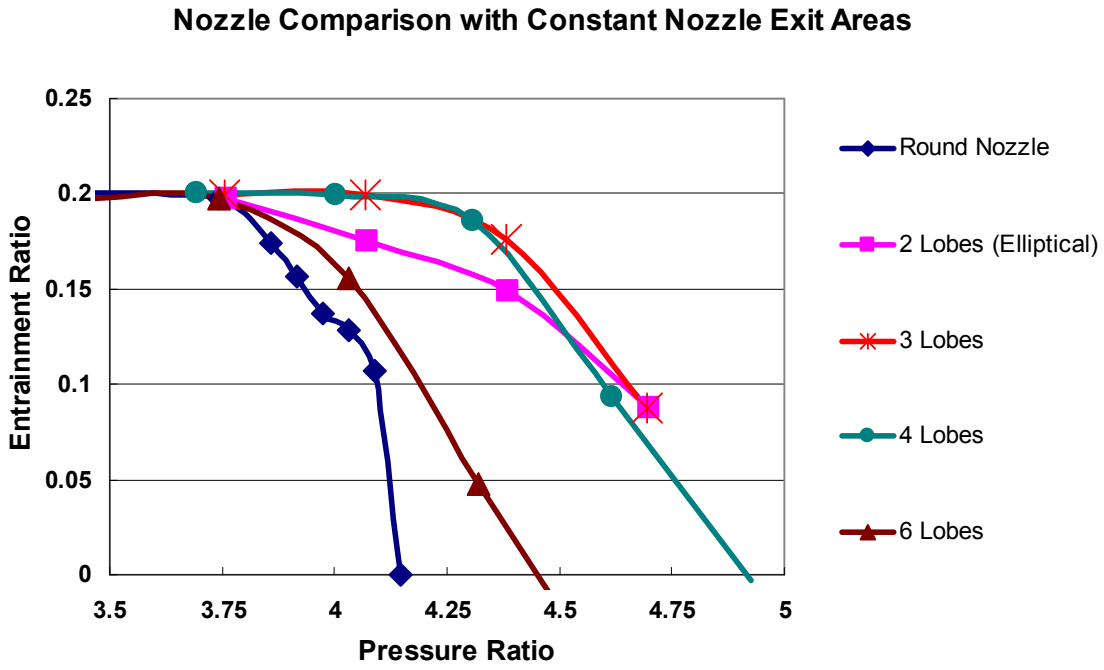

Figure 6.11: Plot of the performance of the different nozzles with the nozzle exit areas constant.

The results clearly show that the lobed nozzle aids in pressure recovery for a given entrainment ratio. It was also found that the perimeter was the driving force. There are an infinite number of geometries to reach this perimeter value. The results for the above conditions suggest the optimum value is near 30 mm.

The final step is to take the knowledge gained from Chapters Four and Five and combine the geometries to investigate the upper limit to the pressure recovery. Figure 6.12 shows the results for the lobed geometries compared to the round nozzle for both the CPM and CRMC ejector profile. The lobed nozzle produced an increase in pressure recovery for both CPM and CRMC profiles over the round nozzle; 15.1% and 6.4% respectively. However, comparing the current technology (round nozzle with the CPM profile) with the best performing ejector (3 lobes with the CRMC profile) there was a 43.5% increase in pressure recovery.

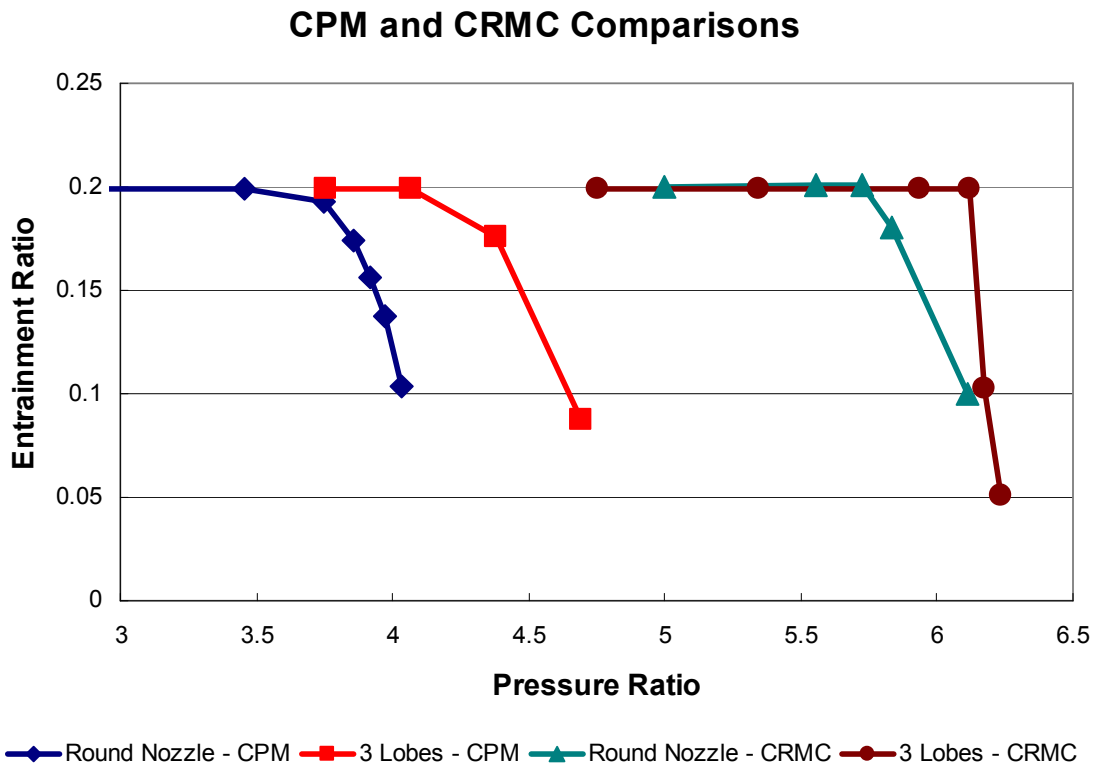

Figure 6.12: Comparisons of CPM and CRMC geometries with different nozzle configurations.

Conclusion

This work investigates enhanced mixing due to flow instability by adding lobes to the circular nozzle design. Pressure recovery was found to improve for constant nozzle exit area designs up to an optimum perimeter value; which for the presented conditions was approximately 30 mm. Increasing the perimeter beyond the optimum, the frictional losses due to mixing adversely affects the pressure recovery and the recovered pressure reduces to that of the round nozzle. Ultimately, when the design combines the optimal number of lobes with that of the profiled mixing channel, a maximum pressure recovery can be achieved. For the conditions explored in this paper, the pressure recovery ratio for the best case was 6.25 compared to 4 for the baseline geometry. It should be noted that in the

ABL system, the primary ejector steam is at much higher temperatures (~1000 K) than simulated for this analysis. However, the increase in temperature adds thermodynamic energy to the system that will aid in further pressure recovery. This is the reason that the ABL can recover up to 150 torr at an altitude of 40,000 feet. Therefore, the results presented are still valid for the ABL. The increase in fluid temperature may change the design, but the improvements seen with the addition of a profile with a lobed nozzle will carry through.

These results are significant to the progress of the ABL in that the potential with these new designs could lead to one of two possible improvements. First, if the same entrainment ratio was held with the current ABL design, the pressure recovery would be greater and the plane could be flown at a lower altitudes. Second, if the pressure recovery is sufficient, the new ejector design could dramatically reduce the amount of primary fluid needed to achieve the desirable pressure recovery. For the above conditions, the primary flow rates could be reduced by 48%.

CHAPTER 7

CONCLUSIONS AND FUTURE WORK

Iodine Mixing Nozzle Bank

This research has demonstrated that the supersonic mixing nozzle can be improved upon and that an optimized design based on mixing efficiency, gain uniformity, and flow uniformity was achieved. Several key changes to the baseline mixing nozzle improved the performance. A single iodine injection orifice allowed for greater penetration into the primary flow, while increasing the length from the orifice to the throat allowed for more I_2 dissociation resulting in an increase in gain uniformity. Using a 3^{rd} order polynomial and limiting the length of the expansion curvature improved flow uniformity. At the time of publication, the optimized nozzle from this research being fabricated and implemented into a $1/40^{th}$ scale COIL.

The optimized design will lead to more power extraction and better beam quality, which has the possibility of reducing the number of COIL modules currently used in the ABL. Second, it may be possible to closely couple the nozzle bank with the gain region, due to the uniform profile, further reducing the size and weight.

Supersonic Ejector

Utilizing a new lobed nozzle design to improve mixing and a contoured diffuser reducing the losses in the flow, both the pressure recovery and entrainment ratio was increased.

This would aid the ABL by being able to fly at a lower altitude with an increased pressure recovery or reducing the amount of overall fluid needed to operate at the current altitude through an increased entrainment ratio. The latter could significantly reduce the weight of the system.

Future Work

Future work for the mixing nozzle needs to be carried out on the experimental verification of the gain uniformity. Close collaboration between the computational and experimental analysis could lead to even further improvements. Additionally, the global optimization routines could be integrated into the design tools; however, this will require an expansion in computational power.

The supersonic ejector needs to have further experimental verification of the new designs and test the limits. Computationally, the CFD models need to be updated to satisfy the actual ABL requirements (if available) for a design that could be implemented into the physical system.

CHAPTER 8

REFERENCES

1. Brown, G., M. Carlyle, D. Diehl, J. Kline, and K. Wood, *A Two-Sided Optimization for Theater Ballistic Missile Defense.* Operations Research, 2005. **53**(5): p. 745-763.
2. Ellis, M.W. and J. Record, *Theater Ballistic Missile Defense and US Contingency Operations.* Parameters 22, 1992: p. 11-26.
3. Wirsig, G.W., *The Airborne Laser and the Future of the Theater Missile Defense.* Air Command and Staff College, Maxwell AFB, AL, 1997(ADA397885).
4. U.S. Department of Defense, M.D.A. [cited 2009 January, 12]; Available from: www.mda.mil.
5. *A Brief History of the Airborne Laser*. 1993, United States Air Force: Kirtland AFB, NM.
6. McDermott, W.E., N.R. Pchelkin, D.J. Benard, and R.R. Bousek, *An electronic transition chemical laser.* Applied Physics Letters, 1978. **32**(8): p. 469-470.
7. Perram, G.P., *Chemical Lasers*, Air Force Institute of Technology.
8. Boeing. *Technical Characteristics -- Boeing 747-400 Freighter*. 2009 [cited; Available from: http://www.boeing.com/commercial/747family/pf/pf_400f_prod.html.
9. Madden, T.J. *Detailed Mixing in COIL Devices*. in *AIAA Plasmadynamics and Lasers Conference*. 1994. Colorado Springs, CO.
10. Madden, T.J. *Chemical Oxygen-Iodine Laser Technology Development using 3-D Navier-Stokes Simulation*. in *HPCMP Users Group Conference*. 2006. Denver, CO.
11. Madden, T.J. *Chemical Oxygen-Iodine Laser Device Simulation Using the 3D, Unsteady Navier-Stokes Equations*. in *IEEE Computer Society Users Group Conference*. 2007.
12. Madden, T.J., J.H. Miller, A.I. Lampson, and D.N. Plummer. *3-D Navier-Stokes Simulation of Chemical Laser Devices*. in *IEEE Computer Society Users Group Conference*. 2005.
13. Madden, T.J., C.A. Noren, L. Emmert, and M.C. Heaven. *A method for comparison of computational fluid dynamic simulation and planar laser induced fluorescence images for a supersonic flowfield*. in *High Energy/Average Power Lasers and Intense Beam Applications II*. 2008. San Jose, CA, USA: SPIE.

14. Madden, T.J. *Application of 3-D, Unsteady Navier-Stokes Simulation to Chemical Oxygen-Iodine Laser Technology Development*. in *HPCMP Users Group Conference*. 2008. Seattle, WA.
15. Miller, J.H., J.S. Shang, and R.F. Tomaro, *Computation of Compressible Flows Through a Chemical Laser Device with Crossflow Injection.* Journal of Propulsion and Power, 2001. **17**(4).
16. Endo, M., T. Masuda, and T. Uchiyama, *Supersonic chemical oxygen-iodine laser with X-shaped streamwise vortex Generator.* Quantum Electronics, IEEE Journal of, 2006. **42**(1): p. 71-77.
17. Opgenorth, M.J., W.E. McDermott, P. Laz, and C.S. Lengsfeld, *The Development of Automated Probabilistic and Optimization Design Tools for Chemical Laser Systems*, in *Mechanical and Materials Engineering*. 2008, University of Denver: Denver, CO.
18. Lohn, P.D., TRW Space and Electronics Group, Redondo Beach, CA; Chan, W. R., TRW Space and Electronics Group, Redondo Beach, CA; Haflinger, D. E., TRW Space and Electronics Group, Redondo Beach, CA; Fink, S. F., TRW Space and Electronics Group, Redondo Beach, CA; Behrens, H. W., TRW Space and Electronics Group, Redondo Beach, CA; Plummer, D. N., RDA Associates, Albuquerque, NM; Buonadonna, V. R., Boeing Space and Communications, Seattle, WA; Walter, R. F., Schafer Corp., Albuquerque, NM in *AIAA Plasmadynamics and Lasers Conference, 32nd*. 2001 Anaheim, CA.
19. Ionin, A.A., I.V. Kochetov, A.P. Napartovich, and N.N. Yuryshev, *Physics and engineering of singlet delta oxygen production in low-temperature plasma.* Journal of Physics D-Applied Physics, 2007. **40**(2): p. R25-R61.
20. Huang, B.J., J.M. Chang, C.P. Wang, and V.A. Petrenko, *A 1-D analysis of ejector performanceAnalyse unidimensionnelle de la performance d'un éjecteur.* International Journal of Refrigeration, 1999. **22**(5): p. 354-364.
21. Keenan, J.H., E.P. Neumann, and F. Lustwerk, *An investigation of ejector design by analysis and experiment.* ASME Journal of Applied Mechanics, 1950(72): p. 299-309.
22. Munday, J.T. and D.F. Bagster, *A New Ejector Theory Applied to Steam Jet Refrigeration.* Industrial & Engineering Chemistry Process Design and Development, 1977. **16**(4): p. 442-449.
23. Aly, N.H., A. Karameldin, and M.M. Shamloul, *Modelling and simulation of steam jet ejectors.* Desalination, 1999. **123**(1): p. 1-8.
24. Eames, I.W., S. Aphornratana, and H. Haider, *A theoretical and experimental study of a small-scale steam jet refrigerator.* International Journal of Refrigeration, 1995. **18**(6): p. 378-386.
25. Huang, B.J. and J.M. Chang, *Empirical correlation for ejector designCorrélation empirique pour la conception des éjecteurs.* International Journal of Refrigeration, 1999. **22**(5): p. 379-388.
26. Aphornratana, S. and I.W. Eames, *A small capacity steam-ejector refrigerator: experimental investigation of a system using ejector with movable primary nozzle.* International Journal of Refrigeration, 1997. **20**: p. 352-358.

27. Chen, Y.-M. and C.-Y. Sun, *Experimental study of the performance characteristics of a steam-ejector refrigeration system.* Experimental Thermal and Fluid Science, 1997. **15**(4): p. 384-394.
28. Sun, D.-W., *Variable geometry ejectors and their applications in ejector refrigeration systems.* Energy, 1996. **21**(10): p. 919-929.
29. Singhal, G., A.L. Dawar, and P.M.V. Subbarao, *Application of profiled ejector in chemical lasers.* Applied Thermal Engineering, 2008. **28**(11-12): p. 1333-1341.
30. Sriveerakul, T., S. Aphornratana, and K. Chunnanond, *Performance prediction of steam ejector using computational fluid dynamics: Part 1. Validation of the CFD results.* International Journal of Thermal Sciences, 2007. **46**(8): p. 812-822.
31. Varga, S., A.C. Oliveira, and B. Diaconu, *Numerical assessment of steam ejector efficiencies using CFD.* International Journal of Refrigeration, 2009. **32**(6): p. 1203-1211.
32. Bartosiewicz, Y., Z. Aidoun, and Y. Mercadier, *Numerical assessment of ejector operation for refrigeration applications based on CFD.* Applied Thermal Engineering, 2006. **26**(5-6): p. 604-612.
33. Eames, I.W., *A new prescription for the design of supersonic jet-pumps: the constant rate of momentum change method.* Applied Thermal Engineering, 2002. **22**(2): p. 121-131.
34. Varga, S., A.C. Oliveira, and B. Diaconu, *Influence of geometrical factors on steam ejector performance - A numerical assessment.* International Journal of Refrigeration, 2009. **32**(7): p. 1694-1701.
35. Srikrishnan, A.R., J. Kurian, and V. Sriramulu, *An experimental investigation of thermal mixing and combustion in supersonic flows.* Combustion and Flame, 1996. **107**(4): p. 464-474.
36. Chang, Y.-J. and Y.-M. Chen, *Enhancement of a steam-jet refrigerator using a novel application of the petal nozzle.* Experimental Thermal and Fluid Science, 2000. **22**(3-4): p. 203-211.
37. Haven, B.A. and M. Kurosaka, *Kidney and anti-kidney vortices in crossflow jets.* Journal of Fluid Mechanics, 1997. **352**: p. 27-64.
38. FLUENT_Inc., *FLUENT Documentation*. 2006.
39. Nocedal, J. and S.J. Wright, *Numerical Optimization*. Springer Series in Operations Research, ed. P. Glynn and S.M. Robinson. 1999, New York: Springer-Verlag.
40. Vanderplaats, G.N., *Numerical Optimization Techniques for Engineers*. Third Edition ed. 2001, Colorado Springs, CO: Vanderplaats Research and Development, Inc.
41. Byrd, R.H. and R.A. Waltz, *An Active-Set Algorith for Nonlinear Programming Using Parametric Linear Programming*. 2007, University of Southern California, Department of Industrial and Systems Engineering.
42. MATLAB. 1994-2008, The MathWorks Inc.
43. J. Han, D.N.P., P.G. Crowell, J. Erkkila, G.D. Hager, C. Helms, and K. Truesdell, *Heuristic method for evaluating coil performance.* AIAA Journal, 1996. **34**: p. 1595-1603.

44. Opgenorth, M.J., W.E. McDermott, P. Laz, and C.S. Lengsfeld, *A Combined Probabilistic and Optimization Approach for Improved Chemical Mixing Systems Design.* International Journal for Numerical Methods in Fluids, 2009. **Submitted November 11, 2009**
45. Capelle, G.A. and H.P. Broida, *Lifetimes and quenching cross sections of I[sub 2](B [sup 3] Pi[sub Ou][sup +]).* The Journal of Chemical Physics, 1973. **58**(10): p. 4212-4222.
46. McDermott, W.E., *Reduced Kinetics Model for a Chemical Oxygen Iodine Laser*, M.J. Opgenorth and C.S. Lengsfeld. 2007, Unpublished: Denver.
47. Azyazov, V.N. and M.C. Haeven, *Role of O2(b) and I2 (A',A) in Chemical Oxygen?Iodine Laser Dissociation Process.* AIAA Journal, 2006. **44**: p. 1593-1600.
48. Perram, G.P., *Approximate analytic solution for the dissociation of molecular iodine in the presence of singlet oxygen.* International Journal of Chemical Kinetics, 1995. **27**(8): p. 817-828.
49. R.F. Heider III, C.E.G., G.I. Segal, T.M. El-Sayed, *Chain-reaction mechanism for molecular iodine dissociation in the O2(a)-iodine atom laser.* Journal of Physical Chemistry, 1983. **87**: p. 2348-60.
50. Azyazov, V.N., S.Y. Pichugin, and M.C. Heaven, *On the dissociation of I-2 by O-2(a (1)Delta): Pathways involving the excited species I-2(A(') (3)Pi(2u),A (3)Pi(1u)), I-2(X (1)Sigma,upsilon), and O-2(a (1)Delta,upsilon).* Journal of Chemical Physics, 2009. **130**(10).
51. Furman, D., E. Bruins, B.D. Barmashenko, and S. Rosenwaks, *Small-signal gain and iodine dissociation in a supersonic chemical oxygen-iodine laser with transonic injection of iodine.* Applied Physics Letters, 1999. **74**(21): p. 3093-3095.
52. Guillaume, D.W. and T.A. Judge, *Improving the efficiency of a jet pump using an elliptical nozzle.* Review of Scientific Instruments, 1999. **70**(12): p. 4727-4729.
53. El-Dessouky, H., H. Ettouney, I. Alatiqi, and G. Al-Nuwaibit, *Evaluation of steam jet ejectors.* Chemical Engineering and Processing, 2002. **41**(6): p. 551-561.
54. Srikrishnan, A.R., J. Kurian, and V. Sriramulu, *Experimental Study on Mixing Enhancement by Petal Nozzle in Supersonic Flow.* Journal of Propulsion and Power, 1996. **12**(1): p. 165-169.
55. Hu Hui, T.K., Tatsuo Saga, Nobuyuki Taniguchi, Sigeki Segawa, Akira Ono. *Research on the Mixing Enhancement Performance of Lobed Nozzles by using PIV and LIV*. in *1998 ASME Fluids Engineering Division Summer Meeting*. 1998. Washington D.C.: ASME.

CHAPTER 9

APPENDICIES

Appendix A

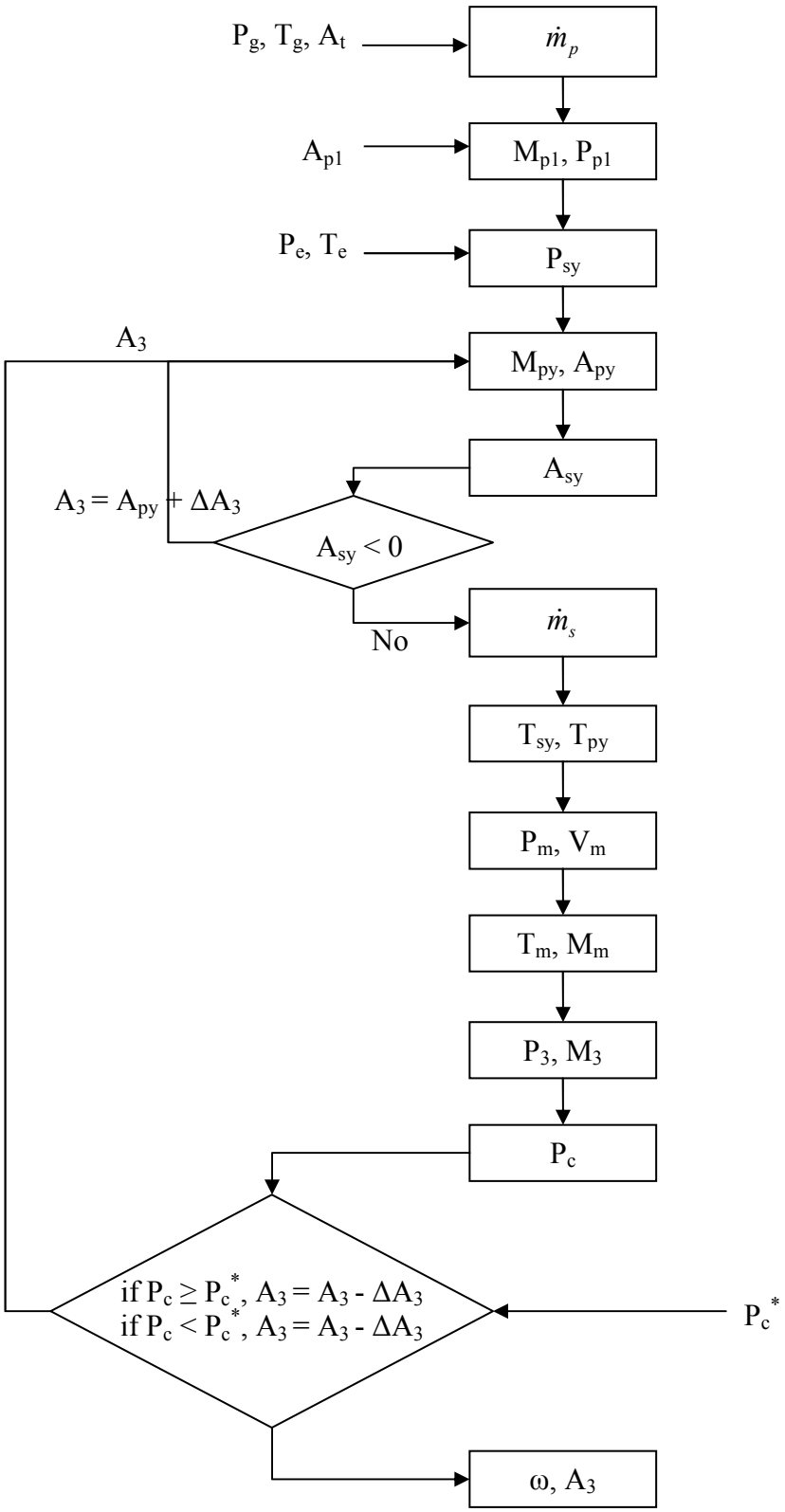
P_g, T_g, A_t
$\dot{m}_p$
A_{p1}
M_{p1}, P_{p1}
P_e, T_e
P_{sy}
A_3
M_{py}, A_{py}
A_{sy}
$A_3 = A_{py} + \Delta A_3$
$A_{sy} < 0$
No
$\dot{m}_s$
T_{sy}, T_{py}
P_m, V_m
T_m, M_m
P_3, M_3
P_c
if $P_c \geq P_c^*$, $A_3 = A_3 - \Delta A_3$
if $P_c < P_c^*$, $A_3 = A_3 - \Delta A_3$
P_c^*
ω, A_3

Appendix B

CRMC Method for Calculating a Profiled Ejector Channel

$P_{og} := 1.98 \cdot 10^5 Pa$ $T_{og} := 393K$ $m_{dot} := .001 \frac{kg}{s}$ $U_{NE} := 980 \frac{m}{s}$

$P_{os} := 872Pa$ $T_{os} := 278K$ $R_m := 0.42$ $U_s := 50 \frac{m}{s}$

$\gamma := 1.3$ $R := 462 \frac{J}{kg \cdot K}$ $Cp := 2100 \frac{J}{kg \cdot K}$

$\theta := 8deg$ $L_D := 245mm$ $U_{DE} := 50 \frac{m}{s}$

Working Fluid - water/steam

$$U_1 := \frac{U_{NE} + R_m \cdot U_s}{1 + R_m} \qquad U_D(x) := U_1 - \frac{(U_1 - U_{DE}) \cdot x}{L_D}$$

$$T_{o1} := \frac{T_{og} + R_m \cdot T_{os}}{1 + R_m} \qquad T_1 := T_{o1} - \frac{U_1^2}{2 \cdot Cp}$$

$$P_{NE} := P_{os} - \frac{\rho_s \cdot U_s^2}{2} \qquad P_{o1} := P_{NE} \cdot \left(\frac{T_{o1}}{T_1} \right)^{\frac{\gamma}{\gamma - 1}}$$

$$T(x) := T_{o1} - \frac{U_D(x)^2}{2 \cdot Cp} \qquad P(x) := P_{o1} \cdot \left(\frac{T(x)}{T_{o1}} \right)^{\frac{\gamma}{\gamma - 1}}$$

$$\rho(x) := \frac{P(x)}{R \cdot T(x)} \qquad D_D(x) := 1 \sqrt{\frac{m_{dot} \cdot (1 + R_m) \cdot R \cdot T(x)}{\pi \cdot P(x) \cdot U_D(x)}}$$

$D_D(0mm) = 9.108mm$ $D_D(100mm) = 7.444mm$ $D_D(245mm) = 17.61mm$

$P(0mm) = 859.5Pa$ $P(100mm) = 2698.462Pa$ $P(245mm) = 4826.448Pa$